
1

2 μ/π separation using

3 Convolutional Neural Networks

4 for the MicroBooNE

5 Charged Current Inclusive Cross Section

6 Measurement

8 Jessica Nicole Esquivel

9 Bachelor of Science in Electrical Engineering and Applied Physics

10 St. Mary's University

11 San Antonio, TX, USA 2011

12 DISSERTATION

13 Submitted in partial fulfillment
14 of the requirements for the degree

15 *Doctor of Philosophy in Physics*

16 - * - DRAFT January 29, 2018 - * -

17 December, 2017
18 Syracuse University
19 Syracuse, New York

20
21
22
23

Copyright 2017
Jessica Nicole Esquivel
All Rights Reserved
Syracuse University

24



μ BooNE



26

Abstract

27

The purpose of this thesis was to use Convolutional Neural Networks
28 (CNN) to separate μ' s and π' s for use in increasing the acceptance rate
29 of μ' 's below the implemented 75cm track length cut in the Charged
30 Current Inclusive (CC-Inclusive) event selection for the CC-Inclusive
31 Cross-Section Measurement. In doing this, we increase acceptance
32 rate for CC-Inclusive events below a specific momentum range.

33

Dedication

34

I dedicate this dissertation to the two important women in my life; My
35 wife and my mom. Both have been there cheering me on giving me strength
36 and love as I worked towards the hardest accomplishment I've ever done.

37

Jessica Nicole Esquivel

38

Acknowledgements

39 Of the many people who deserve thanks, some are particularly prominent, such as
40 my supervisor...

Contents

42	List of figures	xv
43	List of tables	xxv
44	1 Introduction	1
45	2 Neutrinos	3
46	2.1 What are Neutrinos	3
47	2.2 History of Neutrinos	4
48	2.3 Neutrino Oscillations	4
49	2.3.1 Solar Oscillations and the Solar Neutrino Problem	5
50	2.3.2 Atmospheric Oscillations and the Atmospheric Neutrino Anomaly	7
51	2.3.3 Two Flavor Neutrino Oscillation Formulation	9
52	2.3.4 Three Flavor Neutrino Oscillation Formulation	12
53	2.3.5 Reactor Oscillation	13
54	3 The MicroBooNE Experiment	15
55	3.1 Liquid argon time projection chambers	15
56	3.2 The MicroBooNE Time Projection Chamber	16
57	3.3 MicroBooNE's Physics Goals	18
58	3.3.1 The low-energy excess	18
59	3.3.2 Cross sections	19
60	3.3.3 Liquid argon detector development	20
61	3.4 The Booster Neutrino Beam	20
62	3.4.1 Creating the Booster Neutrino Beam	21
63	3.5 Event Reconstruction	22

64	4 Neutrino Identification: Finding MicroBooNE's first Neutrinos	25
65	4.1 Flash Finding	25
66	4.1.1 Flash Reconstruction	26
67	4.1.2 Beam Timing	27
68	4.1.3 Event Rates	28
69	4.2 TPC Topology Selection	28
70	4.2.1 Cosmic Tagging	29
71	4.2.2 2D Cluster Selection	29
72	4.2.3 3D Tracks and vertices Selection	31
73	4.2.4 TPC Updates	33
74	4.3 Conclusion	34
75	5 CC-Inclusive Cross Section Selection Filter	37
76	5.1 Data and MC Processing Chain	38
77	5.2 Normalization of data and MC	39
78	5.3 Optical Software Trigger and Reconstruction	40
79	5.3.1 Software Trigger	40
80	5.3.2 Flash Reconstruction	41
81	5.3.3 Beam Window	42
82	5.4 TPC Reconstruction	44
83	5.4.1 Hit Reconstruction	45
84	5.4.2 Clustering	45
85	5.4.3 Pandora	46
86	5.4.4 Trackkalmanhit	46
87	5.4.5 Cosmic Hit Removal	46
88	5.4.6 Projection Matching Algorithm	47
89	5.5 Event Selection	47
90	5.5.1 Expected Bakgrounds	48
91	5.5.2 Truth Distributions	51
92	6 Background on Convolutional Neural Networks	59
93	6.1 Image Classification	59
94	6.2 CNN Structure	60
95	6.2.1 Backpropagation	63
96	6.3 Choosing Hyperparameters	64

97	7 Training process of Convolutional Neural Networks	67
98	7.1 Hardware Configurations for Convolutional Neural Network Training	67
99	7.2 Creating images using LArTPC data for training/validation of CNNS	68
100	7.3 Convolutional Neural Network Training	70
101	7.3.1 Training CNN1075	70
102	7.3.2 Training CNN10000	73
103	7.3.3 Training CNN100000	76
104	8 Using Convolutional Neural Networks for ν_μ CC event classification	87
105	8.1 Classification using CNN10000	87
106	8.1.1 Classification of MC data using Selection I CC-Inclusive Filter .	87
107	8.1.2 Conclusions of CNN10000 classification of MC data	95
108	8.2 Classification using CNN100000	96
109	8.2.1 Classification of MC data using Selection I CC-Inclusive Filter .	96
110	8.2.2 Classification of MicroBooNE data using Selection I CC-Inclusive	
111	Filter	106
112	8.2.3 Comparing two CC-Inclusive Cross Section Selection Filters . .	106
113	9 Conclusion	107
114	Bibliography	109

¹¹⁵ List of figures

¹¹⁶	2.1	The Standard Solar Model	5
¹¹⁷	2.2	Solar Neutrino Experiments	7
¹¹⁸	2.2a	Ray Davis's Homestake Experiment	7
¹¹⁹	2.2b	Kamiokande Experiment	7
¹²⁰	2.2c	SNO Experiment	7
¹²¹	2.3	Cosmic Ray Shower	8
¹²²	2.4	Measurements of the double ratio for various atmospheric neutrino experiments	9
¹²⁴	2.5	The flavor eigenstates are rotated by an angle θ with respect to the mass eigenstates	10
¹²⁶	3.1	Low Energy excess seen in MiniBooNE	19
¹²⁷	3.2	Arial view of the Main Injector and the Booster Neutrino Beam at Fermilab	21
¹²⁸	3.3	Arial view of the Main Injector and the Booster Neutrino Beam at Fermilab	23
¹²⁹	3.4	Energy spectrum of the Booster Neutrino Beam at Fermi National Laboratories	24
¹³¹	4.1	Efficiency for selecting beam events as a function of minimum total PE cut for all PE cuts as well as zoomed into interesting region.	26
¹³³	4.2a	Predicted distribution of flash times with respect to trigger time for 1 day of data taking at nominal rate and intensity	31

135	4.2b Measured distribution of flash times with a 50 PE threshold cut, with respect to trigger time. Shown as a ratio to the expected cosmic rate from off-beam data. A clear excess from neutrinos is visible between 3- 5 μ s after the trigger time.	31
139	4.3 Percent of good clusters remaining for neutrinos and cosmics after the primary cuts were applied. This is relative to total number of initial clusters.	32
142	4.4 Percent matched cluster pairs remaining for neutrinos and cosmics after secondary cuts applied. This is relative to the number of events that contain clusters which pass the primary cuts.	32
145	4.5 First Neutrino Interaction Candidate Events from MicroBooNE	35
146	4.6 First Neutrino Interaction Candidate Events from MicroBooNE	36
147	5.1 5.1a Track range distribution for selection I. The track range is defined as the 3D distance between the start and end of the muon candidate track. No data is shown below 75 cm due to the track length cut described previously. 5.1b Efficiency of the selected events by process quasi-elastic (QE), resonant (RES), and deep-inelastic (DIS). Statistical uncertainty is shown in the bands and the distributions are a function of true muon momentum. The rise of the efficiency between 0 GeV and 0.5 GeV is due to the minimum track length cut and the decreasing efficiency for higher momentum tracks is caused by the containment requirement.	40
156	5.1a Track range distribution of selection I	40
157	5.1b Selection efficiency as a function of the true muon momentum	40
158	5.2 Time distribution of reconstructed optical flashes with a PE value of 50 or more for a sample of BNB unbiased triggered events.	42
160	5.3 Flash time distribution for all flashes (left plot) and flashes > 20PE (right plot). The different curves are as follows: on-beam data (black), off-beam data (red), CORSIKA inTime MC (light blue), BNB only MC (green), and BNB+Cosmic MC (purple). The dashed vertical lines mark the time window that was chosen for each sample	43

165	5.4 Reconstruction chain run on both data and MC. The red stars mean that the algorithm returns reconstructed 3D vertices.	44
167	5.5 Event selection diagram for selection I and selection II. This analysis focused on optimizing selection I. Boxes with the same color across the two selections symbolize similar cuts.	49
170	5.6 MC momentum distributions of the muon originating from a ν_μ CC interaction. Upper left is the momentum distributions of events with a vertex within the FV (green) and the events with a fully contained track (blue) before the selection. The upper right side is the momentum distribution after the selection (red). The lower plot is the selection efficiencies.	52
176	5.7 MC $\cos(\theta)$ distributions of the muon originating from a ν_μ CC interac- tion. Upper left is the $\cos(\theta)$ distributions of events with a vertex within the FV (green) and the events with a fully contained track (blue) before the selection. The upper right side is the $\cos(\theta)$ distribution after the selection (red). The lower plot is the selection efficiencies.	53
181	5.8 MC ϕ distributions of the muon originating from a ν_μ CC interaction. Upper left is the ϕ distributions of events with a vertex within the FV (green) and the events with a fully contained track (blue) before the selection. The upper right side is the ϕ distribution after the selection (red). The lower plot is the selection efficiencies.	54
186	5.9 MC momentum distributions of the muon originating from a ν_μ CC interaction. Upper left is the momentum distributions of events with a vertex within the FV split up into CCQE (red), CCRES (yellow), and CCDIS (green) before selection. The upper right side is the momentum distribution after the selection with the same color schemes. The lower plot is the selection efficiencies for all three interaction types. The definition of QE, RES, and DIS is based on GENIE.	55

193	5.10 MC $\cos(\theta)$ distributions of the muon originating from a ν_μ CC interaction. Upper left is the $\cos(\theta)$ distributions of events with a vertex within the FV split up into CCQE (red), CCRES (yellow), and CCDIS (green) before selection. The upper right side is the $\cos(\theta)$ distribution after the selection with the same color schemes. The lower plot is the selection efficiencies for all three interaction types. The definition of QE, RES, and DIS is based on GENIE.	56
200	5.11 MC ϕ distributions of the muon originating from a ν_μ CC interaction. Upper left is the ϕ distributions of events with a vertex within the FV split up into CCQE (red), CCRES (yellow), and CCDIS (green) before selection. The upper right side is the ϕ distribution after the selection with the same color schemes. The lower plot is the selection efficiencies for all three interaction types. The definition of QE, RES, and DIS is based on GENIE.	57
207	6.1 Pixel representation and visualization of a curve detector filter. As you can see, in the pixel representation, the weights of this filter are greater along a curve we are trying to find in the input image	61
210	6.2 Visualization of filters found in first layer of a CNN.	61
211	6.3 Applying a feature mask over a set of fashion items to extract necessary information for auto-encoding. Unnecessary information for example color or brand emblems are not saved. This feature map is an edge detection mask that leaves only shape information which helps to distinguish between different types of clothes.	62
216	6.4 Pictorial Representation of Convolutional Neural Networks as well as a visual representation on CNN's complexity of layer feature extraction	62
218	6.5 Pictorial representation of the AlexNet model. The AlexNet model consists of 5 convolution layers and 3 fully connected layers.	65

220	6.6	Pictoral representation of the GoogleNet model. The GoogleNet model 221 consists of 22 layers. The model implements 9 Inception modules which 222 performs covolution and pooling in parallel and strays away from 223 the basis that CNN layers need to be stacked up sequentially. The 224 GoogleNet model also doesn't use fully connected layers, instead it 225 uses average pooling which greatly reduces the amount of parameters. 226 GoogleNet has 12x fewer parameters than AlexNet.	65
227	7.1	Accuracy vs. Loss of AlexNet 2-output μ/π sample consisting of 2,150 228 images each.	71
229	7.2	Description of confusion matrix variables: False pion rate = $false\pi/total\pi$ 230 True pion rate = $true\pi/total\pi$ Accuracy = $(true\pi rate + true\mu rate)/2$ 231 Pion prediction value = $true\pi/(true\pi + false\pi)$ Muon prediction value 232 = $true\mu/(true\mu + false\mu)$	72
233	7.2a	Confusion Matrix showing Accuracy of CNN1075 using training 234 MC data	72
235	7.2b	Confusion Matrix showing Accuracy of CNN1075 using testing 236 MC data	72
237	7.3	Accuracy vs. Loss of AlexNet 2-output μ/π sample consisting of 10,000 238 images each.	74
239	7.4	Description of confusion matrix variables: False pion rate = $false\pi/total\pi$; 240 True pion rate = $true\pi/total\pi$; Accuracy = $(true\pi rate + true\mu rate)/2$; 241 Pion prediction value = $true\pi/(true\pi + false\pi)$; Muon prediction value 242 = $true\mu/(true\mu + false\mu)$	75
243	7.4a	Confusion Matrix showing Accuracy of CNN10000 using training 244 MC data	75
245	7.4b	Confusion Matrix showing Accuracy of CNN10000 using testing 246 MC data	75
247	7.5	Probability plot of muons and pions from testing set. Images surrounding 248 histogram are a random event from lowest bin and highest bin for 249 each particle.	76

250	7.6 Training and testing accuracy of CNN trained on 100,000 images of $\mu/\pi/p/\gamma/e$ with 20,000 images of each particle. Each image was a size of 576x576 and the images per particle were split 90% use for training and 10% used for testing the network	77
254	7.7 Training and testing loss of CNN trained on 100,000 images of $\mu/\pi/p/\gamma/e$	77
255	7.8 Confusion Matrix of all five particles	78
256	7.9 t-SNE of CNN	79
257	7.10 Probabilities of different particle classes as well as their contamination from other classes	80
259	7.10a Muon Prob	80
260	7.10b Pion Prob	80
261	7.10c Proton Prob	80
262	7.10d Electron Prob	80
263	7.10e Gamma Prob	80
264	7.11 Muon probability of true muons (blue) versus pions (red), protons (cyan), gammas (green) and electrons (magenta).	81
266	7.12 Kinematic distributions versus muon probability for true muons and true pions.	82
268	7.12a Track range versus muon probability for true muons (blue) and true pions (red).	82
270	7.12b Track range $\leq 75\text{cm}$ versus muon probability for true muons (blue) and true pions (red).	82
272	7.12c Momentum versus muon probability for true muons (blue) and true pions (red).	82
274	7.13 Kinematic distributions versus muon probability for true muons and true protons.	83
276	7.13a Track range versus muon probability for true muons (blue) and true protons (cyan).	83

278	7.13b Track range $\leq 75cm$ versus muon probability for true muons (blue) and true protons (cyan).	83
280	7.13c Momentum versus muon probability for true muons (blue) and true protons (cyan).	83
282	7.14 Kinematic distributions versus muon probability for true muons and true electrons.	84
284	7.14a Track range versus muon probability for true muons (blue) and true electrons (magenta).	84
286	7.14b Track range $\leq 75cm$ versus muon probability for true muons (blue) and true electrons (magenta).	84
288	7.14c Momentum versus muon probability for true muons (blue) and true electrons (magenta).	84
290	7.15 Kinematic distributions versus muon probability for true muons and true gammas.	85
292	7.15a Track range versus muon probability for true muons (blue) and true gammas (green).	85
294	7.15b Track range $\leq 75cm$ versus muon probability for true muons (blue) and true gammas (green).	85
296	7.15c Momentum versus muon probability for true muons (blue) and true gammas (green).	85
298	8.1 Confusion matrix and probability plot of events passing selection I cc-inclusive cuts right before 75cm track length cut	88
300	8.1a Confusion Matrix for CNN10000 classified events from selection I	88
301	8.1b Probability plot for CNN10000 classified events from selection I	88
302	8.2 CNN10000 distributions of track candidate images output from Selection I Modified cc-inclusive filter	89
304	8.2a Track range distribution of events from Selection I Modified passing CNN with 70% accuracy	89

306	8.2b	Stacked signal and background track range distributions from Selection I Modified passing CNN with 70% accuracy	89
307			
308	8.2c	Stacked signal and background track range distributions from Selection I Modified passing 75 cm track length cut	89
309			
310	8.2d	Stacked signal muons and background muons/pions of track range distributions from Selection I Modified passing CNN with 70% accuracy	89
311			
312			
313	8.2e	Stacked signal muons and background muons/pions of track range distributions from Selection I Modified passing 75 cm track length cut	89
314			
315			
316	8.3	CNN10000 stacked signal/background track range distributions of track candidate images output from Selection I Modified cc-inclusive filter	90
317			
318	8.3a	Stacked signal muons and background muons/pions of track range distributions from Selection I Modified passing CNN with 75% accuracy	90
319			
320			
321	8.3b	Stacked signal muons and background muons/pions of track range distributions from Selection I Modified passing CNN with 80% accuracy	90
322			
323			
324	8.3c	Stacked signal muons and background muons/pions of track range distributions from Selection I Modified passing CNN with 85% accuracy	90
325			
326			
327	8.3d	Stacked signal muons and background muons/pions of track range distributions from Selection I Modified passing CNN with 90% accuracy	90
328			
329			
330	8.4	CNN10000 momentum distributions of track candidate images output from Selection I Modified cc-inclusive filter	91
331			
332	8.4a	Momentum distribution of events from Selection I Modified passing CNN with 70% accuracy	91
333			
334	8.4b	Stacked signal and background momentum distributions from Selection I Modified passing CNN with 70% accuracy	91
335			

336	8.4c	Stacked signal and background momentum distributions from Selection I Modified passing 75 cm track length cut	91
337			
338	8.5	Track distribution comparisons of true CC muons plotted vs true CC muons and pions plotted	92
339			
340	8.5a	Stacked signal μ /background μ and π track range distribution of CNN @ 70%	92
341			
342	8.5b	Stacked signal $\mu\&\pi$ /background $\mu\&\pi$ track range distribution of CNN @ 70%	92
343			
344	8.6	Images of true CC events where the pion was the tagged track candidate	93
345	8.6a	Pion reconstructed track range is less than 75 cm and longer than muon track due to dead wires	93
346			
347	8.6b	Pion reconstructed track range is less than 75 cm and larger than muon reconstructed track	93
348			
349	8.6c	Pion reconstructed track range is greater than 75 cm and larger than muon reconstructed track	93
350			
351	8.7	CNN performance of classified muons and pions compared to the already implemented 75 cm track length cut	95
352			
353	8.8	$\text{Cos}(\theta)$ distribution at $\text{CNN10000} \geq 85\%$	96
354			
355	8.9	$\text{Cos}(\theta)$ distribution at $\text{CNN10000} \geq 85\%$	97
356			
357	8.10	$\text{Cos}(\theta)$ distribution at $\text{CNN10000} \geq 85\%$	98
358			
359	8.11	$\text{Cos}(\theta)$ distribution at $\text{CNN10000} \geq 85\%$	99
360			
361	8.12	$\text{Cos}(\theta)$ distribution at $\text{CNN10000} \geq 85\%$	100
362			
363	8.13	$\text{Cos}(\theta)$ distribution at $\text{CNN10000} \geq 85\%$	101
364			
365	8.14	$\text{Cos}(\theta)$ distribution at $\text{CNN10000} \geq 85\%$	102
366			
367	8.15	$\text{Cos}(\theta)$ distribution at $\text{CNN10000} \geq 85\%$	103
368			
369	8.16	$\text{Cos}(\theta)$ distribution at $\text{CNN10000} \geq 85\%$	104
370			
371	8.17	$\text{Cos}(\theta)$ distribution at $\text{CNN10000} \geq 85\%$	105
372			

³⁶³ List of tables

³⁶⁴ 4.1	Passing rates for 2D cluster cuts for neutrino on MC set and a cosmic only MC set. First column shows event rates with no cuts applied to both sets. Columns two and three show event rates after primary and secondary cuts are applied. Line three shows the second line scaled with the flash finding factor of 0.008. All events are normalized to per day assuming we are running at 5 Hz.	31
³⁷⁰ 5.1	Passing rates of Selection I. Numbers are absolute event counts and cosmic background is not scaled. The BNB+Cosmic sample contains all events, not just ν_μ CC inclusive. The numbers in brackets give the passing rate wrt the step before (first percentage) and wrt total generated events (second percentage). The BNB+Cosmic MC-Truth column shows how many true ν_μ CC inclusive events are left in the sample. This number includes mis-identifications where a cosmic track is picked by the selection instead of the neutrino interaction in the same event. The cosmic only sample is used just to illustrate the cut efficiency. The last column Signal:Cosmic only gives an estimate of the ν_μ CC events wrt the cosmic only background at each step. For this number, the cosmic background has been scaled as described in section 5.2.	50
³⁸² 5.2	Passing rates for Selection I selection applied to on-beam and off-beam data. The numbers in brackets give the passing rate wrt the step before (first percentage) and wrt the generated events (second percentage). Off-beam data has been scaled with a factor 1.23 to normalize to the on-beam data stream.	50

387	8.1 Comparing passing rates of CNN at different probabilities versus 75 cm track length cut: Numbers are absolute event counts and Cosmic background is not scaled appropriately. The BNB+Cosmic sample contains all events. The numbers in brackets give the passing rate wrt the step before (first percentage) and wrt the generated events (second percentage). In the BNB+Cosmic MC Truth column shows how many true ν_μ CC-inclusive events (in FV) are left in the sample. This number includes possible mis-identifications where a cosmic track is picked by the selection instead of the neutrino interaction in the same event. The CNN MC True generated events were scaled wrt the MC True generated events for the 75 cm cut passing rates due to only running over 188,880 generated events versus the 191362 generated events. The last column Signal:Cosmic only gives an estimate of the ν_μ CC events wrt the cosmic only background at each step. For this number, the cosmic background has been scaled as described in [?]. Note that these numbers are not a purity, since other backgrounds can't be determined at this step. . .	93
403	8.2 Signal and background event numbers of selection I and selection I with CNN cut estimated from a BNB+Cosmic sample and Cosmic only sample normalized to $5 * 10^{19}$ PoT. The last column gives the fraction of this signal or background type to the total selected events per CNN probability.	94

*"If they don't give you a seat at the table,
bring a folding chair."*

— Shirley Chisholm

⁴¹⁰ **Chapter 1**

⁴¹¹ **Introduction**

⁴¹² This thesis will be a description of work done to further increase efficiency and purity
⁴¹³ of the charged current inclusive cross section measurement using the MicroBooNE
⁴¹⁴ detector. It will also describe the MicroBooNE detector, what neutrinos are, the
⁴¹⁵ charged current inclusive cross section measurement and its importance as well as
⁴¹⁶ convolutional neural networks and how they can be used in μ/π separation. Chapter
⁴¹⁷ **2** will talk about the background of neutrinos and the people and detectors that
⁴¹⁸ discovered neutrinos as well as an in depth history of neutrino oscillation and the
⁴¹⁹ discovery that neutrinos have mass.

⁴²⁰ Chapter **3** will discuss the MicroBooNE experiment, specifically, how Liquid
⁴²¹ Argon Time Projection Chambers work, the Light Collection System and the Electronic
⁴²² and Readout Trigger systems. This chapter will also describe the Booster Neutrino
⁴²³ Beam sationed at Fermilab.

⁴²⁴ Chapter **4** will discuss the work that was done to detect the first neutrinos seen in
⁴²⁵ the MicroBooNE detector and the software reconstruction efforts required to create an
⁴²⁶ automated neutrino ID filter that was used to find the first neutrinos and then was
⁴²⁷ later expanded on to create the charged current inclusive filter that will be discussed
⁴²⁸ in chapter **5**

⁴²⁹ Chapter **6** will give a brief description of what Convolutional Neural Networks are
⁴³⁰ and how it will be used for μ/π separation in this selection. Chapter **7** will discuss
⁴³¹ the hardware frameworks and training methods used to train multiple Convolutional
⁴³² Neural Networks for use in the charged current inclusive cross section measurement.
⁴³³ Chapters **8** and **??** will discuss the results of using Convolutional Neural Networks on
⁴³⁴ monte-carlo and data to sift out charged current inclusive neutrino events.

⁴³⁵ **Chapter 2**

⁴³⁶ **Neutrinos**

⁴³⁷ **2.1 What are Neutrinos**

⁴³⁸ Neutrinos are fundamental particles which help make up the universe. They are also
⁴³⁹ one of the least understood. Neutrinos are not affected by the electromagnetic force
⁴⁴⁰ because they do not have electric charge. Neutrinos are affected by a weak sub-atomic
⁴⁴¹ force of much shorter range than electromagnetism, and are therefore able to pass
⁴⁴² through great distances in matter without much possibility of being affected by it.
⁴⁴³ Until the late 1990's, neutrinos were thought to have no mass. Neutrinos are created
⁴⁴⁴ by radioactive decay such as the ones that happen in the sun, in nuclear reactors or
⁴⁴⁵ when cosmic rays hit atoms. There are three types of neutrinos, ν_e , ν_μ and ν_τ which
⁴⁴⁶ correspond to their charged lepton pairs.

⁴⁴⁷ As previously stated, neutrinos are very weakly interacting; in fact, neutrinos can
⁴⁴⁸ pass unscathed through a wall of lead several hundred light-years thick. Because
⁴⁴⁹ neutrinos interact so rarely, studying neutrinos requires a massive detector and a
⁴⁵⁰ powerful neutrino source. With that being said, we can only "see" a neutrino when
⁴⁵¹ they interact in a detector. In a collision, distinct charged particles are produced with
⁴⁵² each type of neutrino because of the weak force. An electron neutrino will create an
⁴⁵³ electron, a muon neutrino will create a muon, and a tau neutrino will create a tau. The
⁴⁵⁴ charged lepton track the particle leaves in the detector is how one figures out what
⁴⁵⁵ type of neutrino interaction was "seen". Liquid Argon Time Projection Chambers are
⁴⁵⁶ being used to study neutrinos due to their excellent imaging and particle identification
⁴⁵⁷ capabilities.

⁴⁵⁸ 2.2 History of Neutrinos

⁴⁵⁹ The neutrino was first postulated by Wolfgang Pauli in 1931 to explain how beta
⁴⁶⁰ decay could resolve the conservation of energy, momentum and angular momentum
⁴⁶¹ problem. Pauli suggested that this missing energy might be carried off, unseen, by a
⁴⁶² neutral particle (he called neutron) which was escaping detection. James Chadwick
⁴⁶³ discovered a much heavier nuclear particle in 1932 that he also named neutron, leaving
⁴⁶⁴ two particles with the same name. Enrico Fermi was the first person to coin the
⁴⁶⁵ term neutrino (which means little neutral one in latin) in 1933 to fix this confusion.
⁴⁶⁶ Fermi's paper, which was published in 1934, unified Pauli's neutrino with Paul Dirac's
⁴⁶⁷ positron and Werner Heisenberg's neutron-proton model and his theory accurately
⁴⁶⁸ explained many experimentally observed results. Wang Ganchang first proposed the
⁴⁶⁹ use of beta capture to experimentally detect neutrinos and in 1959 Clyde Cowan and
⁴⁷⁰ Frederick Reines published their work stating that they had detected the neutrino.
⁴⁷¹ The experiment called for antineutrinos created in a nuclear reactor by beta decay that
⁴⁷² reacted with protons producing neutrons and positrons: $\nu_e + p^+ \rightarrow n^0 + e^+$. Once
⁴⁷³ this happens, the positron finds an electron and they annihilate each other and the
⁴⁷⁴ resulting gamma rays are detectable. The neutron is detected by neutron capture and
⁴⁷⁵ the releasing of another gamma ray. In 1962 Leon M. Lenderman, Melvin Schwartz
⁴⁷⁶ and Jack Steinberger were the first to detect interactions of the muon neutrino. The
⁴⁷⁷ first detection of the tau neutrino was announced in the summer of 2000 by the
⁴⁷⁸ DONUT collaboration at Fermilab. In the late 1960s, many experiments found that the
⁴⁷⁹ number of electron neutrinos arriving from the sun was around 1/3 to 1/2 the number
⁴⁸⁰ predicted by the Standard Solar Model. This became known as the solar neutrino
⁴⁸¹ problem and remained unresolved for around thirty years. This problem was resolved
⁴⁸² by the discovery of neutrino oscillation and mass. [1]

⁴⁸³ 2.3 Neutrino Oscillations

⁴⁸⁴ Neutrino oscillation was first predicted by Bruno Pontecorvo. It describes the phe-
⁴⁸⁵ nomenon of a neutrino created with a specific lepton flavor (electron, muon or tau)
⁴⁸⁶ that is later measured to have a different flavor. Neutrino oscillation is important
⁴⁸⁷ theoretically and experimentally due to the fact that this observation implies that the
⁴⁸⁸ neutrino has a non-zero mass, which is not part of the original Standard Model of
⁴⁸⁹ particle physics. [2]

490 2.3.1 Solar Oscillations and the Solar Neutrino Problem

491 The solar neutrino flux derived from Bahcall's Standard Solar Model is shown in figure
 492 2.1. Nuclear fusion and decay processes produce an abundant amount of neutrinos.
 493 The standard solar model predicts that these reactions produce several groups of
 494 neutrinos, each with differing fluxes and energy spectra. The figure also shows the
 495 ranges of detection of existing solar neutrino experiments in different shades of blue
 496 to illustrate that they sample different portions of the solar neutrino energy spectrum.
 497 Three of these experiments, plus a new one, are discussed below.

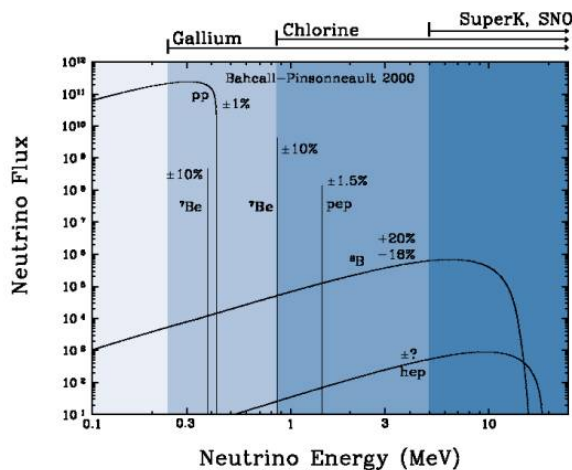


Figure 2.1: The Standard Solar Model

498 Since neutrinos rarely interact with matter, they pass through the sun and the earth
 499 undetected. About 65-billion neutrinos from the sun stream through every square
 500 centimeter on the Earth every second, yet we are oblivious to their passage in our
 501 every-day lives. [3]

502 The first experiment to detect the effects of neutrino oscillation was the Ray Davis's
 503 Homestake Experiment. The detector was stationed in the Homestake Gold Mine in
 504 Lead, South Dakota. It was 1,478 meters underground and was $380\ m^3$. The detector
 505 was filled with perchloroethylene. Perchloroethylene was chosen because of its high
 506 concentrations of chlorine. When an ν_e interacted with chlorine-37 atom, the atom
 507 would transform to argon-37 which was then extracted and counted. The neutrino
 508 capture reaction is shown in equation 2.1. Davis observed a deficit of about 1/3
 509 the flux of solar neutrinos that was predicted by Bahcall's Standard Solar Model.

- 510 The unexplained difference between the measured solar neutrino flux and model
511 predictions lead to the Solar Neutrino Problem. [4]



512 While it is now known that the Homestake Experiment detected neutrinos, some
513 physicist were weary of the results. Conclusive evidence of the Solar Neutrino Problem
514 was provided by the Kamiokande-II experiment, a water Cherenkov detector with
515 a low enough energy threshold to detect neutrinos through neutrino-electron elastic
516 scattering. In the elastic scattering interaction the electrons coming out of the point of
517 reaction strongly point in the direction that the neutrino was traveling, away from the
518 sun. While the neutrinos observed in Kamiokande-II were clearly from the sun, there
519 was still a discrepancy between Kamiokande-II and Homestake; The Kamiokande-
520 II experiment measured about 1/2 the predicted flux, rather than the 1/3 that the
521 Homestake Experiment saw.

522 The solution to the solar neutrino problem was finally experimentally determined
523 by the Sudbury Neutrino Observatory(SNO). The Ray Davis's Homestake Experiment
524 was only sensitive to electron neutrinos, and the Kamiokande-II Experiment was
525 dominated by the electron neutrino signal. The SNO experiment had the capability to
526 see all three neutrino flavors. Because of this, it was possible to measure the electron
527 neutrinos and total neutrino flux. The experiment demonstrated that the deficit was
528 due to the MSW effect, the conversion of electron neutrinos from their pure flavor
529 state into the second neutrino mass eigenstate as they passed through a resonance
530 due to the changing density of the sun. The resonance is energy dependent, and is
531 visible near 2 MeV. The water cherenkov detectors only detect neutrinos above about 5
532 MeV, while the radiochemical experiments were sensitive to lower energy (0.8 MeV for
533 chlorine, 0.2 MeV for gallium), and this turned out to be the source of the difference
534 in the observed neutrino rates at the two types of experiments. Figure 2.2 shows
535 Homestake, Kamiokande-II and SNO experiments.

536 MSW Effect

537 The Mikheyev-Smirnov-Wolfenstein effect is a process which acts to modify neu-
538 trino oscillations in matter. The presence of electrons in matter changes the energy

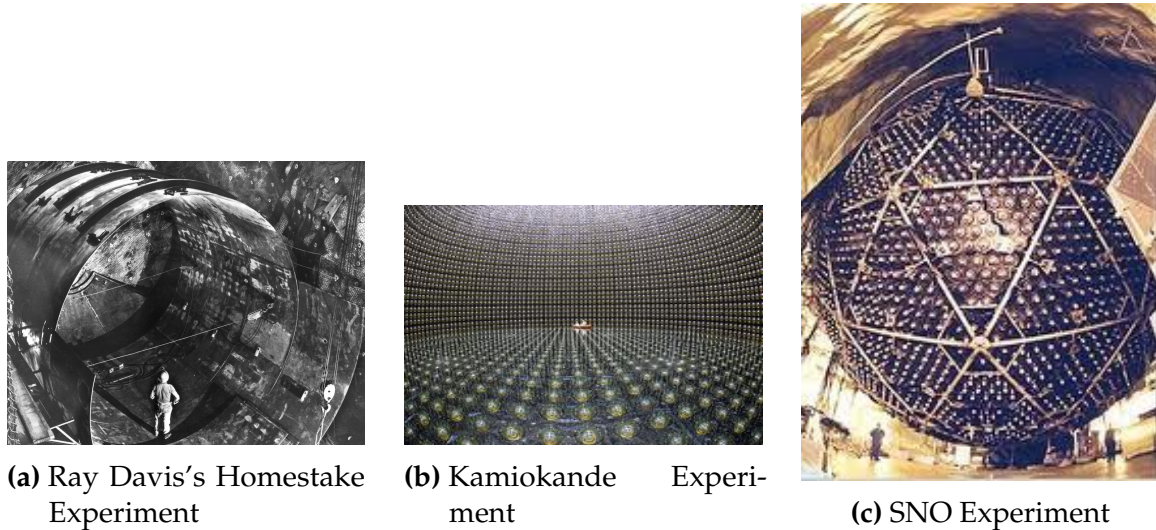


Figure 2.2: Solar Neutrino Experiments

539 levels of the mass eigenstates of neutrinos due to charged current coherent forward
 540 scattering of the electron neutrinos. This coherent forward scattering is similar to
 541 the electromagnetic process with respect to the refractive index of light in a medium.
 542 Because of this MSW Effect, neutrinos in vacuum have a different effective mass than
 543 neutrinos in matter and because neutrino oscillations depend on the squared mass
 544 difference of the neutrinos, the neutrino oscillations are different in matter than in
 545 vacuum. This effect is important at the sun where electron neutrinos are produced.
 546 The neutrinos of high energy leaving the sun are in a vacuum propagation eigenstate
 547 ν_2 that has a very small overlap with the electron neutrino $\nu_e = \nu_1 \cos(\theta) + \nu_2 \sin(\theta)$
 548 seen by the charged current reactions in Kamiokande-II and SNO. The discrepancy of
 549 the deficit between SNO, Kamiokande-II and Homestake is due to the energy of the
 550 solar neutrinos. The MSW effect "turns on" at about 2 MeV and at lower energies, this
 551 MSW effect is negligible. [5]

552 **2.3.2 Atmospheric Oscillations and the Atmospheric Neutrino 553 Anomaly**

554 Atmospheric neutrinos are neutrinos that stem from the decay hadrons coming from
 555 primary cosmic rays. The dominant part of the decay chain is shown in equations 2.2
 556 and 2.3

$$\pi^+ \rightarrow \mu^+ \nu_\mu \mu^+ \rightarrow e^+ \nu_e \bar{\nu}_\mu \quad (2.2)$$

557

$$\pi^- \rightarrow \mu^- \bar{\nu}_\mu \mu^- \rightarrow e^- \bar{\nu}_e \nu_\mu \quad (2.3)$$

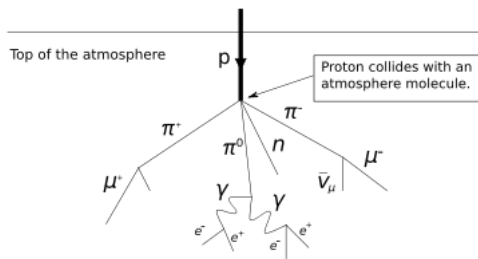


Figure 2.3: Cosmic Ray Shower

558 Figure 2.3 shows the cosmic ray shower. In general, these neutrinos have energies
 559 from 1 GeV to 100s of GeV and the ratio of ν_μ s to ν_e s equals to 2 (see equation 2.4)

$$R = \frac{(\nu_\mu + \bar{\nu}_\mu)}{(\nu_e + \bar{\nu}_e)} \quad (2.4)$$

560 There have been two types of detectors used to study atmospheric neutrinos: Water
 561 Cherenkov detectors and tracking calorimeters. Super-Kamiokande is the detector we
 562 will focus on. These atmospheric detector experiments measure the ratio of ν_μ to ν_e .
 563 They also measure the zenith angle distribution of the neutrinos. These experiments
 564 report a double ratio (shown in equation 2.5). This double ratio is the ratio measured
 565 in the detector to the ratio that's expected which is 2. If the double ratio equals to 1, the
 566 data agrees with the prediction. Various measurements from multiple experiments
 567 are shown in figure 2.4. Except for Frejus, all R measurements are less than 1. This
 568 discrepancy between the predicted R and the measured R became known as the
 569 Atmospheric Neutrino Anomaly.

$$R = \frac{(N_\mu / N_e)_{DATA}}{(N_\mu / N_e)_{SIM}} \quad (2.5)$$

570 Kamiokande-II has the capability of measuring the direction of the incoming
 571 neutrinos. The expectation of atmospheric neutrino detection is that the flux be

Experiment	Type of experiment	R
Super-Kamiokande	Water Cerenkov	0.675 ± 0.085
Soudan2	Iron Tracking Calorimeter	0.69 ± 0.13
IMB	Water Cerenkov	0.54 ± 0.12
Kamiokande	Water Cerenkov	0.60 ± 0.07
Frejus	Iron Tracking Calorimeter	1.0 ± 0.15

Figure 2.4: Measurements of the double ratio for various atmospheric neutrino experiments

isotropic due to the fact that atmospheric neutrinos can reach the detector from all directions. Kamiokande-II noticed that muon-like data did not agree well with this expectation. At low energies approximately half of the ν_μ are missing over the full range of zenith angles. At high energies the number of ν_μ coming down from above the detector seems to agree with expectation, but half of the same ν_μ coming up from below the detector are missing. This anomaly can be easily explained by neutrino flavor oscillations. Due to the fact that the neutrino travels less distance coming straight down into the detector (about 15km) than coming up from the bottom of the detector(13000km) changes the probability of oscillation. The probability of oscillation for the muon neutrinos coming down into the detector is roughly zero, whereas for neutrinos coming up, the oscillation probability is $\sin^2(2\theta)$. Both the solar and atmospheric neutrino problems can be explained by neutrino oscillation so its fitting to derive this phenomenon mathematically. In the next two sections, two flavor and three flavor neutrino oscillation derivations will be explained.

2.3.3 Two Flavor Neutrino Oscillation Formulation

The flavor eigenstates can oscillate between each other because they are composed of an add-mixture of mass eigenstates(ν_1, ν_2). Figure 2.5 shows the mass and flavor eigenstates rotated by an angle θ which is the mixing angle.

In matrix form the wavefunctions are:

$$\begin{pmatrix} \nu_\mu \\ \nu_e \end{pmatrix} = \begin{pmatrix} \cos\theta & \sin\theta \\ -\sin\theta & \cos\theta \end{pmatrix} * \begin{pmatrix} \nu_1 \\ \nu_2 \end{pmatrix} \quad (2.6)$$

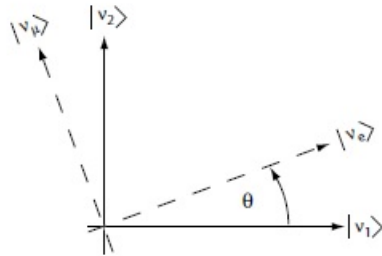


Figure 2.5: The flavor eigenstates are rotated by an angle θ with respect to the mass eigenstates

591 Applying the time evolution operator to ν_μ :

$$|\nu_\mu(t)\rangle = -\sin\theta|\nu_1\rangle e^{-i\frac{E_1 t}{\hbar}} + \cos\theta|\nu_2\rangle e^{-i\frac{E_2 t}{\hbar}} \quad (2.7)$$

592 where $E_1 = \sqrt{p^2 c^2 + m_1^2 c^4}$ and $E_2 = \sqrt{p^2 c^2 + m_2^2 c^4}$ and $p_1 = p_2$. For the time
 593 being, let us assume $\hbar = c = 1$. With this assumption: $E_1 = \sqrt{p^2 + m_1^2}$ and $E_2 =$
 594 $\sqrt{p^2 + m_2^2}$. The next modifications is to assume neutrinos are relativistic:

$$\gamma = \frac{E}{m_o c^2} = \frac{\sqrt{p^2 c^2 + m_o^2 c^4}}{m_o c^2} \gg 1 \quad (2.8)$$

595 because of this,

$$p \gg m_o \quad (2.9)$$

596

$$E = \sqrt{p^2 + m_o^2} = p\sqrt{1 + m_o^2/p^2} \simeq p + \frac{1}{2}\frac{m_o^2}{p} \quad (2.10)$$

597 where the binomial expansion is used. Now E_1 and E_2 can be written as:

$$E_1 \simeq p + \frac{1}{2}\frac{m_1^2}{p} \text{ and } E_2 \simeq p + \frac{1}{2}\frac{m_2^2}{p} \quad (2.11)$$

598 Now applying all these assumptions back into equation 2.7 gives us:

$$|\nu_\mu(t)\rangle = -\sin\theta|\nu_1\rangle e^{-i\left(p + \frac{1}{2}\frac{m_1^2}{p}\right)t} + \cos\theta|\nu_2\rangle e^{-i\left(p + \frac{1}{2}\frac{m_2^2}{p}\right)t} \quad (2.12)$$

$$|\nu_\mu(t)\rangle = e^{-i\left(p+\frac{1}{2}\frac{m_1^2-m_2^2}{p}\right)t} (-\sin\theta|\nu_1\rangle + \cos\theta|\nu_2\rangle) \quad (2.13)$$

599 Substituting $\Delta m^2 = m_1^2 - m_2^2$ and $t = \frac{x}{c} = x$ and $e^{-iz} = e^{-i\left(p+\frac{1}{2}\frac{m_1^2}{p}\right)t}$ gives us:

$$|\nu_\mu(t)\rangle = e^{-iz} \left(-\sin\theta|\nu_1\rangle + \cos\theta|\nu_2\rangle e^{+ix\left(\frac{1}{2}\frac{\Delta m^2}{p}\right)} \right) \quad (2.14)$$

600 Finding the Probability for a $\nu_\mu \rightarrow \nu_e$:

$$P(\nu_\mu \rightarrow \nu_e) = |\langle \nu_e | \nu_\mu(t) \rangle|^2 \quad (2.15)$$

601 Remembering that $\langle \nu_i | \nu_j \rangle = \delta_{ij}$

$$\langle \nu_e | \nu_\mu(t) \rangle = e^{-iz} \left(-\sin\theta\cos\theta + \sin\theta\cos\theta e^{\frac{i\Delta m^2 x}{p}} \right) \quad (2.16)$$

602 Taking the absolute value squared gives us:

$$P(\nu_\mu \rightarrow \nu_e) = |\langle \nu_e | \nu_\mu(t) \rangle|^2 = e^{+iz} e^{-iz} \sin^2\theta \cos^2\theta \left(-1 + e^{\frac{i\Delta m^2 x}{p}} \right) \left(-1 + e^{\frac{-i\Delta m^2 x}{p}} \right) \quad (2.17)$$

603 Since the neutrino is relativistic we can set $p = E_\nu$ and change $x = L$. Also 604 recognizing the trigonometric relation $(1 - \cos 2\theta)/2 = \sin^2\theta$ the above equation 605 becomes:

$$P(\nu_\mu \rightarrow \nu_e) = \sin^2 2\theta \sin^2 \left(\frac{\Delta m^2 L}{4E_\nu} \right) \quad (2.18)$$

606 All that's left to do now is re-introduce \hbar and c doing this we get:

$$P_{\nu_\mu \rightarrow \nu_e}(L, E) = \sin^2 2\theta \sin^2 \left(1.27 \Delta m^2 \frac{L}{E_\nu} \right) \quad (2.19)$$

607 This equations has three important variables.

- The angle θ : This angle, as mentioned before, is called the mixing angle. It defines the difference between the flavor and the mass eigenstates. When $\theta = 0$ the mass and flavor eigenstates are identical and now oscillations occur.
- The mass squared difference, Δm^2 : Again $\Delta m^2 = m_1^2 - m_2^2$. The reason this is an important variable is because it implies that for neutrinos to oscillate, neutrinos must have mass. Furthermore, the mass squared difference also tells us that the neutrino mass eigenstates must be different.
- L/E: This is the variable that is of most interest to experimental physicists due to the fact that it is the variable that we set. L is the distance between the source and detector and E is the energy of the neutrino. For a given Δm^2 , the probability of oscillation changes with respect to L/E.

2.3.4 Three Flavor Neutrino Oscillation Formulation

Seeing the quantum mechanics involved in deriving the probability of a two flavor neutrino oscillation, it is now possible to formulate the three flavor neutrino oscillation. The three flavor neutrino oscillation formulation begins similarly to the two flavor, but there is the Pontecorvo-Maki-Nakagawa-Sakata matrix (PMNS) instead of the 2X2 matrix in the previous section. The PMNS matrix is show below:

$$\begin{pmatrix} c_{12}c_{13} & s_{12}c_{13} & s_{13}e^{-i\delta} \\ -s_{12}c_{23} - c_{12}s_{23}s_{13}e^{i\delta} & c_{12}c_{23} - s_{12}s_{23}s_{13}e^{i\delta} & s_{23}c_{13} \\ s_{12}s_{23} - c_{12}c_{23}s_{13}e^{i\delta} & -c_{12}s_{23} - s_{12}c_{23}s_{13}e^{i\delta} & c_{23}c_{13} \end{pmatrix} * \begin{pmatrix} e^{i\alpha_1/2} & 0 & 0 \\ 0 & e^{i\alpha_2/2} & 0 \\ 0 & 0 & 1 \end{pmatrix} \quad (2.20)$$

where $c_{ij} = \cos\theta_{ij}$ and $s_{ij} = \sin\theta_{ij}$

Following the same steps as before we get:

$$P_{\alpha \rightarrow \beta} = \delta_{\alpha\beta} - 4\sum Re(U_{\alpha i}^* U_{\beta i} U_{\alpha j} U_{\beta j}^*) \sin^2\left(\frac{\Delta m_{ij}^2 L}{4E}\right) 2\sum Im(U_{\alpha i}^* U_{\beta i} U_{\alpha j} U_{\beta j}^*) \sin\left(\frac{\Delta m_{ij}^2 L}{2E}\right) \quad (2.21)$$

The main things to notice here are δ_{ij} which is the CP violating term and has not been measured yet, and θ_{13} which has just been measured. CP violation is a violation

⁶²⁹ of the postulated CP-symmetry. CP-symmetry states that the laws of physics should
⁶³⁰ be the same if a particle were to be exchanged with its antiparticle and then if the left
⁶³¹ hand side of a decay were switched with the right hand side.

⁶³² **2.3.5 Reactor Oscillation**

⁶³³ Many experiments have searched for oscillation of electron anti-neutrinos produced at
⁶³⁴ nuclear reactors. Such oscillations give the value of the parameter θ_{13} . The KamLAND
⁶³⁵ experiment, started in 2002, has made a high precision observation of reactor neutrino
⁶³⁶ oscillation. Neutrinos produced in nuclear reactors have energies similar to solar
⁶³⁷ neutrinos, a few MeV. The baselines of these experiments have ranged from tens
⁶³⁸ of meters to over 100 km. On 8 March 2012, the Daya Bay team announced a 5.2σ
⁶³⁹ discovery that $\theta_{13} \neq 0$.

640 Chapter 3

641 The MicroBooNE Experiment

642 The purpose of this chapter is to discuss and understand the details of the MicroBooNE
643 detector. A thorough understanding of MicroBooNE and the technology behind liquid
644 argon time projection chambers is important for understanding results as well as
645 understanding how images were made for use in deep learning efforts that will be
646 outlined in later chapters.

647 3.1 Liquid argon time projection chambers

648 Liquid Argon Time Projection Chambers (LArTPCs) are an exciting detector technol-
649 ogy that provide excellent imaging and particle identification, and are now being
650 used to study neutrinos. The Time Projection Chamber (TPC) was first invented by
651 Nygren in 1974 [?] and the proposal for a LArTPC for neutrino physics was made
652 by Rubbia [?] in 1977 with the ICARUS collaboration implementing this concept [?].
653 A LArTPC is a three-dimensional imaging detector that uses planes of wires at the
654 edge of an active volume to read out an interaction. When a neutrino interacts with an
655 argon atom, the charged particles that are produced ionize the LAr as they travel away
656 from the interaction. By placing a uniform electric field throughout the LAr volume,
657 the ionization is made to drift towards a set of anode planes, which consist of wires
658 spaced very closely together collecting the ionized charge, which is subsequently read
659 out by electronics connected to the anode wires. The collected ionization creates a
660 spatial image of what happened in the detector on each anode plane. The position
661 resolution of the interaction along the beam direction (perpendicular to drift direction)
662 relies on the wire pitch, while the resolution in drift direction is dependent on the

663 timing resolution of the electronics used and the longitudinal diffusion in the volume.
664 The drift time of the ionization relative to the time of the original signal allows the
665 signal to be projected back along the drift coordinate, hence the name LArTPC. Having
666 very small distances between each wire within an anode plane allows for very fine
667 granularity and detail to be captured, and having multiple wire planes at different
668 angles provides independent two-dimensional views that can be combined into a
669 three dimensional picture of the interaction. Once the charge signal is created on the
670 anode planes, software analysis packages identify particles in the detector by using
671 deposited energy on the wires along their track length. The 30 year development of the
672 ICARUS detector has led to LArTPCs being used as cosmic ray [?], solar neutrino [?]
673 and accelerator neutrino [?] detectors. The ArgoNeuT experiment at Fermilab was
674 the first United States based liquid argon neutrino program that has since produced
675 short-baseline $\nu - Ar$ cross-section measurements in the NUMI beamline [?]. The
676 MicroBooNE experiment is the second experiment in the US based LArTPC neutrino
677 program and will be discussed thoroughly in the next sections. The next phases of
678 the liquid argon neutrino program are under way and are the Fermilab Short Base-
679 line Neutrino (SBN) program [?] and the Deep Underground Neutrino Experiment
680 (DUNE) [6]. The SBN program will include three LArTPC detectors, including the
681 MicroBooNE detector, on the Booster Neutrino Beam (BNB) to do multiple-baseline
682 oscillation measurements. The detector closest to the beam will be the 40 ton Short
683 Baseline Neutrino Detector (SBND) [?] at 150 m and the detector furthest is the 600 ton
684 ICARUS T600 [?] detector positioned at 600 m. The DUNE collaboration will deliver
685 a 30 GeV neutrino beam 1300 km from Fermilab to a 34 kiloton LArTPC detector
686 at Homestake, SD. DUNE will study the leptonic CP phase, δ_{cp} , as well as measure
687 neutrino and antineutrino oscillations.

688 3.2 The MicroBooNE Time Projection Chamber

689 MicroBooNE (Micro Booster Neutrino Experiment) is a 89 ton active volume (180 ton
690 total mass) LArTPC which is then inserted into a cylindrical cryostat on axis of the
691 Booster Neutrino Beam (BNB) stationed at Fermilab in Batavia, Illinois. Understanding
692 LArTPC technology and detector physics is necessary to build a LArTPC the size of
693 DUNE, and MicroBooNE has made many advances in developing this technology [7]
694 [8].

MicroBooNE's Time Projection Chamber (TPC) is 10.3 m long (beamline direction), 2.3 m high and 2.5 m wide (which corresponds to the drift distance). The TPC is shown in figure ?? . MicroBooNE is the largest LArTPC currently running in the world [9]. This LArTPC has 3 wire planes: 1 plane that collects the ionization in the wires and is 0° to the vertical with 3456 wires spaced 3 mm apart, and 2 planes where the ionization drifts passed and induces a signal at $\pm 60^\circ$ to the vertical each with 2400 wires also spaced 3 mm apart. Each plane has a spacing also of 3 mm from eachother. The first two planes are the induction planes and the last is the collection. The 270 V/cm electric field of the TPC is created using 64 stainless steel tubes shaped into rectangles around the TPC and held in place by G10 to form a field cage. The cathode is charged at a high voltage of -70 kV and this voltage is stepped down across the field cage tubes using a voltage divider chain with an equivalent resistance of $240\text{ M}\Omega$ between the tubes. The field cage tubes are separated by 4 cm from center to center. The electron drift distance is 2.5 m in the x direction with a drift time of 2.3 ms. Maintaining high charge yield is done by continuously recirculating and purifying the argon. The purity is monitored using MicroBooNE's light collection system. Another use of the light collection system is initial timing and drift coordinate of the interaction.

MicroBooNE's light collection system is a crucial part for 3D reconstruction of all particle interactions in the LArTPC. The initial interaction time, t_0 , and initial drift coordinate, x_0 , are not known from the TPC alone. For beam events, the accelerator clock is used to determine t_0 of the interaction and the x_0 can be inferred using drift time. Non-beam events, however, do not have this capability, which is why scintillation light from an interaction is used. The $\nu - Ar$ interaction produces scintillation light which is collected by photomultiplier tubes (PMTs) which allows the exact time, t_0 of the neutrino interaction to be determined. The scintillation light created propagates within nanoseconds to the light collection system compared to the milliseconds it takes the ionized electrons from the interaction to reach the anode wire planes. Therefore we can precisely know where along the drift direction the particle interaction first took place. The scintillation light is also localized, so combining the PMT information with the wire plane information allows for cosmic background rejection happening outside the beam timing window.

The light collection system is made up of 32 Hamamatsu R5912-02mod cryogenic PMTs with a diameter of 8-inches. The PMTs are located behind the 3 wire anode planes and provides 0.85% photocathode coverage. Each PMT has an acrylic plate mounted in front of it that is coated with a wave-length shifting material called TPB.

730 The acrylic plates take in the scintillation light, at 128 nm, and re-emits it visible
731 wavelengths visible to the PMTs, with a peak at 425 nm.

732 Both the light collection system and the TPC create analog signal that is read out and
733 digitized by the electronics system. The process requires amplification and shaping of
734 the signal which then goes to the data acquisition (DAQ) software for writing of the
735 digitized data to disk. The anode plane wires are connected to detector specific circuit
736 boards (ASICS) that are submerged and operate inside the liquid argon volume. These
737 ASICS send amplified signal to 11 feed-throughs where further amplification of the
738 signal happens outside the cryostat. The signal is received by custom LArTPC readout
739 modules distributed over nine readout crates which do the digitization. The TPC wires
740 are digitized at 16 MHz then downsampled to 2 MHz. The TPC system reads out 4
741 frames of wire signal data per event, 1 frame before a trigger and 2 frames after the
742 triggered frame. The four frames allows for identification of a neutrino interaction as
743 well as cosmic background rejection. The process of digitization is similar for the light
744 collection system. Each PMT signal undergoes a shaping with a 60 ns peaking time
745 for digitization of multiple samples. The digitization occurs at 64 MHz but are not
746 read out continuously during the TPC readout time. Only shaped PMT signal samples
747 above a small threshold are read out and saved. Both the TPC and PMT readouts are
748 initiated via triggers on a separate trigger board located in a warm electronics crate.
749 The timing trigger is created by a timing signal from the BNB accelerator which is
750 shaped and sent to the trigger board. The PMT trigger is generated when the PMT
751 signal multiplicity is greater than 1 and the summed PMT pulse-height is more than 2
752 photo-electrons summed up over all PMT channels. When the trigger board gets both
753 a timing trigger and a PMT trigger in coincidence, at BNB trigger is then generated by
754 the board. This signal is then passed to all readout crates initiating the readout of data.
755 The data is then sent to the DAQ software which then saves the data to disk into one
756 event memory.

757 3.3 MicroBooNE's Physics Goals

758 3.3.1 The low-energy excess

759 The primary goal of the MicroBooNE experiment is to study and investigate the low-
760 energy excess seen in MiniBooNE 3.1. MicroBooNE has the capability of confirming or

761 denying this excess as electrons or photons due to the detector being in the same beam,
 762 having a similar baseline, and lastly the detector being able to clearly distinguish
 763 between electrons and photons. LArTPCs use the topology of events as well as energy
 764 loss near the vertex to differentiate between single e^- tracks and photon-induced
 765 induced pair production $\gamma \rightarrow e^+ e^-$, which wasn't possible in MiniBooNE, a Cherenkov
 766 detector. This technique has been shown in the ArogoNeuT detector [?] and a side by
 767 side comparison of both event types in a LArTPC can be seen in figure ???. An excess
 768 in electrons would point towards new oscillation physics beyond the standard model,
 769 while photons would be within the standard model. MicroBooNE will observe a $4-5\sigma$
 770 signal.

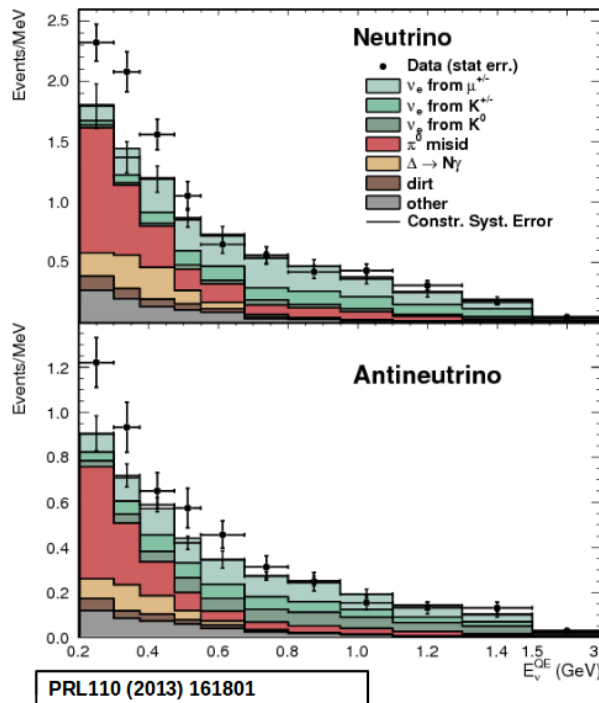


Figure 3.1: Low Energy excess seen in MiniBooNE

771 3.3.2 Cross sections

772 MicroBooNE's neutrino cross-section program will be the first $\nu - Ar$ cross-section in
 773 the 1 GeV energy range and one of only a few cross-section measurements of $\nu - Ar$
 774 in the world. MicroBooNE is also the first liquid argon detector to collect the highest
 775 statistics sample of neutrino interactions. Investigating final-state-interactions in the
 776 1GeV energy range provides information about short range nuclear correlations that
 777 affect the interpretations of neutrino oscillation experiment data.

778 One of the cross-section measurements MicroBooNE can make is an inclusive
 779 charged-current cross-section measurement (referred to as CC-inclusive). CC-inclusive
 780 events consist of a neutrino exchanging a W^\pm boson with an argon atom, producing a
 781 charged lepton and any number of other final state particles. In MicroBooNE's case, a
 782 CC-inclusive event will mostly have a defining muon track coming out of the vertex
 783 due to our neutrinos being predominately ν_μ s. A cross-section measurement is the
 784 energy dependent probability of $\nu - Ar$ interaction in the detector. Cross-sections
 785 however are independent of the intensity or focus of the particle beam so they can
 786 be compared among different experiments. A background for a CC-inclusive cross-
 787 section measurement are the neutral-current events that contain a pion. It is possible
 788 to have a neutral current interaction with a $\pi + p$ event signature that looks like a
 789 charged current $\mu + p$ event. Reconstruction tools implemented to date don't efficiently
 790 separate muons from pions. A common way to separate these two particles species is
 791 to implement a track length cut. On average, muons tend to have longer track lengths
 792 in LArTPCs so by requiring that the hypothesized lepton be above a threshold track
 793 length, it is possible to increase signal to background.

794 3.3.3 Liquid argon detector development

795 The last physics goal for the MicroBooNE collaboration is to provide important infor-
 796 mation regarding LArTPC technology. Being the first in large scare LArTPCs in the US,
 797 MicroBooNE will be albe to provide improvements to High Voltage (HV) distribution,
 798 Noise Characterization [?], and Michel Electron Reconstruction [8].

799 3.4 The Booster Neutrino Beam

800 The MicroBooNE detector is stationed at Fermi National Accelerator Laboratory
 801 (FNAL) where it receives neutrinos from both the Booster Neutrino Beam (BNB)
 802 and Neutrinos from the Main Injector (NuMI) beams. MicroBooNE is on-axis for the
 803 BNB and off-axis by 135 mrad for NuMI. For the purpose of this analysis, only data
 804 from the BNB was used. This section will discuss how neutrinos are created using the
 805 BNB. How these neutrinos are produced as well as their flux through the MicroBooNE
 806 detector is necessary for any analysis because of the systematic uncertainties the beam

807 introduces to a measurement. An aerial view of fermilab as well as the BNB is shown
 808 in figure 3.2

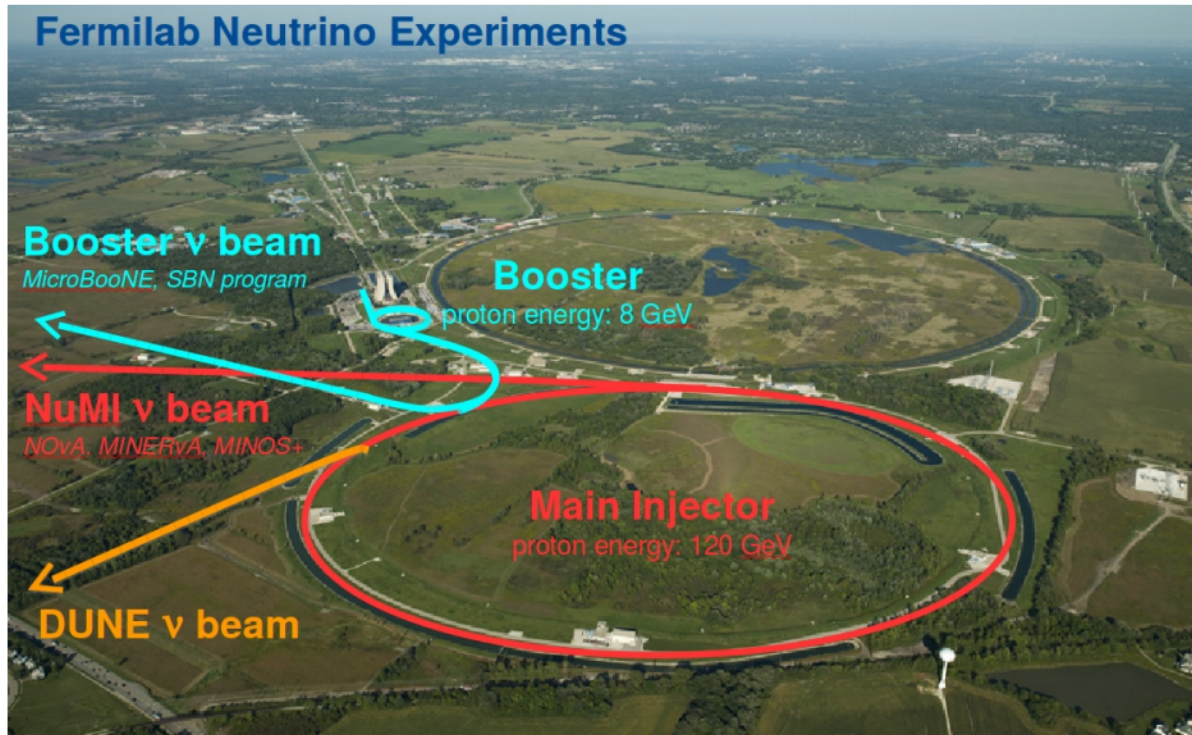


Figure 3.2: Arial view of the Main Injector and the Booster Neutrino Beam at Fermilab

809 3.4.1 Creating the Booster Neutrino Beam

810 The BNB is a very pure ν_μ beam, with only 0.6% contamination from ν_e s. The energy
 811 also peaks around 700 MeV which is desired based on the probability of oscillation
 812 equation which depends on the the value of L/E , where L is the distance of the
 813 detector from the neutrino beam and E is the energy of the neutrino beam. L/E was
 814 chosen to increase the probability of seeing neutrino oscillations in the MiniBooNE
 815 Low Energy Excess (LEE) range based on the probability of oscillation equation, which
 816 is $P_{\nu_\mu \rightarrow \nu_e}(L, E) = \sin^2 2\theta \sin^2 \left(1.27 \Delta m^2 \frac{L}{E} \right)$. The BNB collides 8.9 GeV/c momentum
 817 protons from the FNAL booster synchrotron into a beryllium target which produces a
 818 high flux of neutrinos. The protons originate from H^2 gas molecules that are turned
 819 into H^- ions by a Cockcroft-Walton generator shown in figure ???. The H^- initially are
 820 accelerated to 1MeV kinetic energy and are then passed to a linear accelerator using
 821 alternating electromagnetic fields to increase their energy to 400MeV. The ions are
 822 stripped of electrons by passing them through a carbon foil. The protons are bunched

823 into beam spills which contain $4 * 10^{12}$ protons in a $1.6 \mu\text{s}$ time window per spill. It's
824 at this point that the protons are directed towards the beryllium target. The amount
825 of protons directed towards the target (POT) is measured by two toroids upstream of
826 the target with an error of 2%. Beam intensity, timing, width, position, and direction
827 are monitored by beam position monitors, multi-wire chamber and resistive monitors.
828 The beryllium target is 71.1 cm long, 1.7 proton interaction lengths, and is 0.51 cm in
829 radius. The target is located inside a larger focusing electromagnet called the horn.
830 The horn is an aluminum alloy pulsed toroidal electromagnet. The pulsed current
831 peaks at 170 kA with a time-width of $143 \mu\text{s}$ which coincides with the protons arriving
832 on the target. The current flows from the inner conductor to the outer conductor
833 with a maximum magnetic field of 1.5 Tesla. The magnetic field focuses the charged
834 secondary particles produced by the p-Be interactions. The direction of current can be
835 switched to change the polarity of the secondary particles being focused creating a
836 beam of either primarily neutrinos, with positively charged secondary particles, or
837 antineutrinos.

838 Further down the beamline is a concrete collimator which absorbs particles not
839 necessary to the neutrino flux. The collimator is 214 cm long and 30 cm in radius.
840 After the collimator comes a 45 meter long, 1 meter radius, air-filled cylindrical decay
841 region which then ends in a beam-stop made of steel and concrete. The beam-stop
842 contains an array of gas proportional counters to detect muons. The BNB is shown in
843 figure 3.3.

844 **3.5 Event Reconstruction**

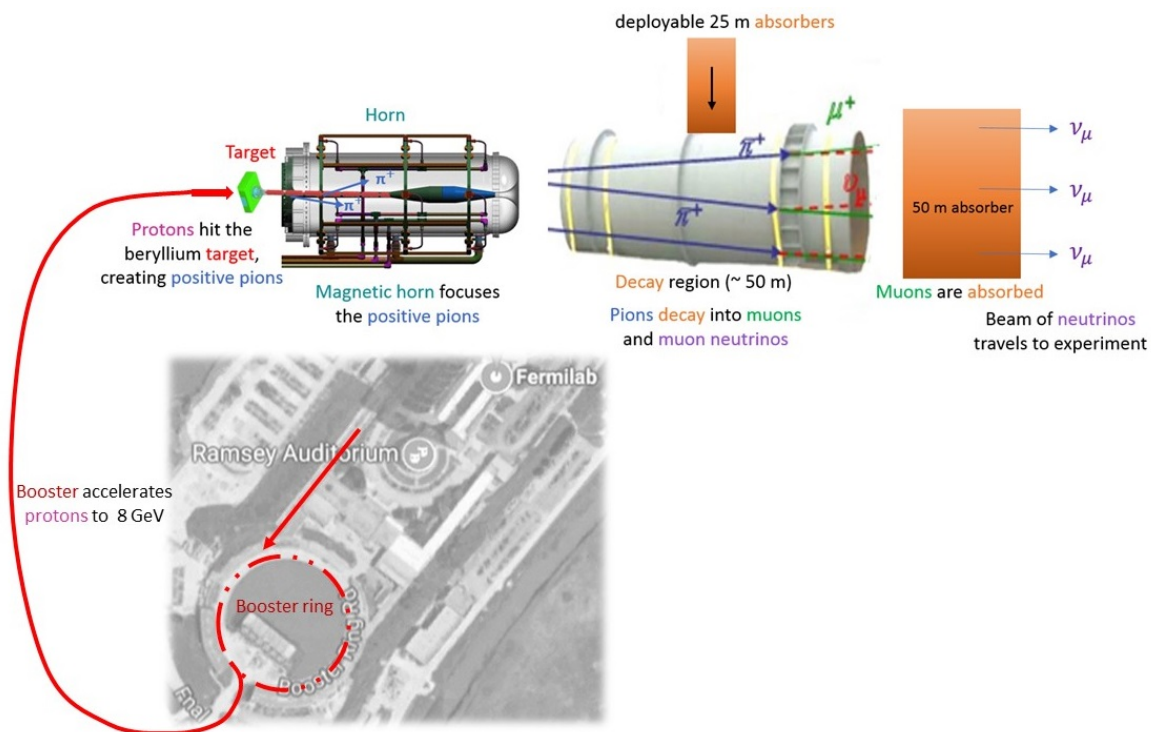


Figure 3.3: Aerial view of the Main Injector and the Booster Neutrino Beam at Fermilab

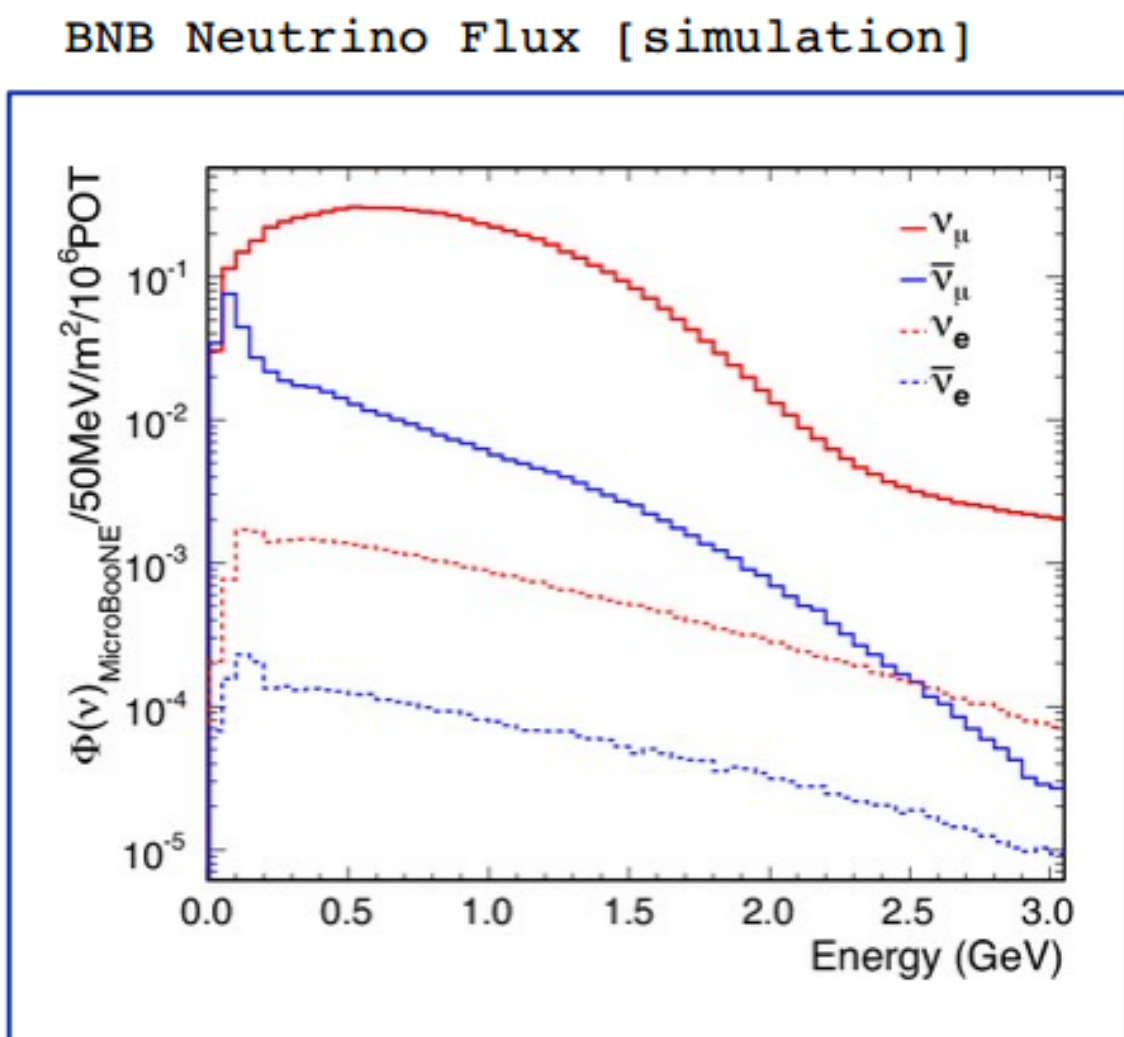


Figure 3.4: Energy spectrum of the Booster Neutrino Beam at Fermi National Laboratories

845 **Chapter 4**

846 **Neutrino Identification: Finding
847 MicroBooNE's first Neutrinos**

848 The goal of the Neutrino Identification analysis was to positively identify BNB neutrino
849 interactions in the MicroBooNE detector collected during the first days of running.
850 Neutrino event candidates were identified in part by using a cut on detected flash of
851 scintillation light during the $1.6 \mu\text{s}$ beam-spill length of the BNB as well as identifying
852 reconstructed object from the TPC that are neutrino like. After this selection, 2D
853 and 3D event displays were used for verification of the selection performance. This
854 selection was targeted to reduce the ratio of neutrino events to cosmic-only events from
855 the initial 1 neutrino to 675 cosmics to a ratio of 1 to 0.5 or better which is equivalent to
856 a background reduction by a factor of 1000 or more. These selected events were used
857 for MicroBooNE's public displays of neutrino interactions. A clearly visible neutrino
858 interaction with an identifiable vertex and at least 2 tracks originating from the vertex
859 was what the analysis focused on. This analysis wasn't optimized for high purity
860 or efficiency, but rather for very distinguishable neutrino interactions that could be
861 identified by the public.

862 **4.1 Flash Finding**

863 Flash finding is the first step used in finding neutrino interactions. This section will
864 detail how optical information is reconstructed as well as analysis scripts and event
865 filters were used.

866 **4.1.1 Flash Reconstruction**

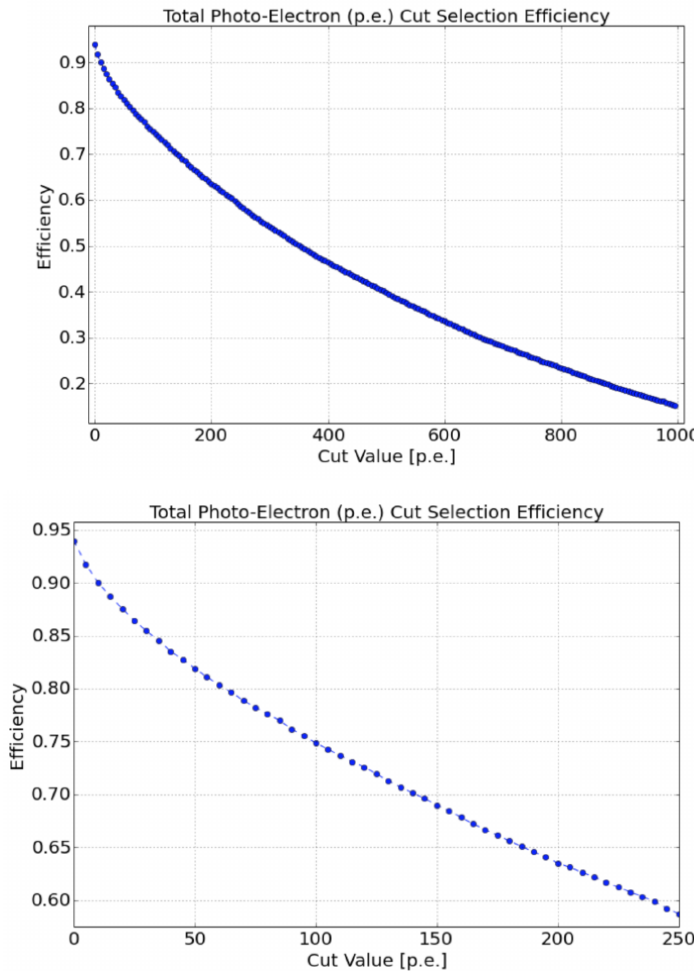
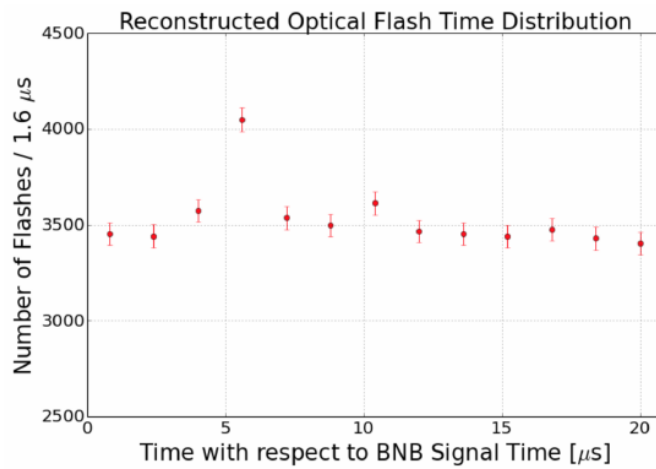


Figure 4.1: Efficiency for selecting beam events as a function of minimum total PE cut for all PE cuts as well as zoomed into interesting region.

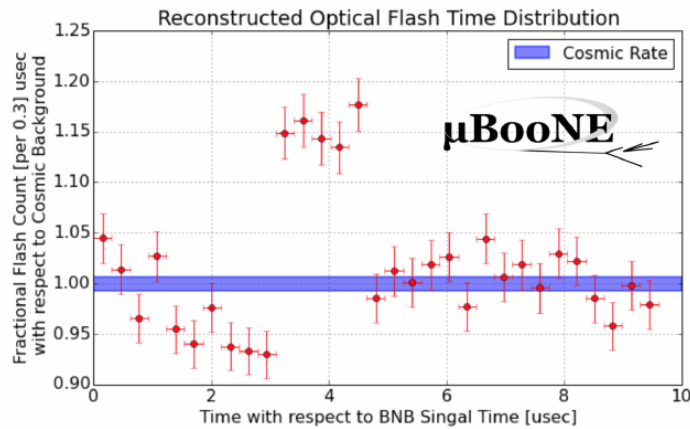
867 A flash is described as a collection of light seen at the same time within the detector.
868 They are then reconstructed by identifying signal from the PMTs above a specific
869 photoelectron (PE) threshold. These signals are called optical hits. Optical hits from
870 all the PMTs are then accumulated into $1\text{ }\mu\text{s}$ bins of time. If a specific bin is above a
871 set PE threshold, then the optical hits that overlap in time are the labeled as the hits
872 from the flash. All flash reconstructed properties like average time and x/y positions
873 are then found via the flash labeled optical hits. The total size of the flash is found by
874 summing up the total number of photoelectrons from all PMTs. Neutrino interactions
875 and cosmic muons will have a larger flash size compared to noise and other low-energy
876 backgrounds, therefore a total PE cut is used to reject these backgrounds. A total PE

⁸⁷⁷ cut of 50 PE was deemed sufficient for this analysis. Figure 4.1 show the total PE
⁸⁷⁸ versus the selection efficency of selecting neutrino beam events.

⁸⁷⁹ **4.1.2 Beam Timing**



(a) Predicted distribution of flash times with respect to trigger time for 1 day of data taking at nominal rate and intensity



(b) Measured distribution of flash times with a 50 PE threshold cut, with respect to trigger time. Shown as a ratio to the expected cosmic rate from off-beam data. A clear excess from neutrinos is visible between 3- 5 μ s after the trigger time.

⁸⁸⁰ It is necessary to get the specific time from flashes if one uses flashes to filter out
⁸⁸¹ neutrino interactions coincident with the neutrino beam spill period and background.
⁸⁸² Before a filter can be applied, an understanding of the timing of the trigger and PMT

readout with respect to the arrival of neutrinos from the BNB. To do this, a $1.6\ \mu s$ window near the expected beamtime was created and verified by finding that the number of flashes was significantly above the cosmic-ray background flashes. Beam data during the first week of running, October 16th 2016 through October 22nd 2016 and were used for a timing measurement. The total POT uses corresponds to roughly 24 hours of data taking at nominal intensity ($4 \times 10^{12} ppp$) and a 5 Hz repetition rate. Figure 4.2a shows size of the expected neutrino signal in time using Monte Carlo predictions and figure 4.2b shows the neutrino signal in data. The intensity in data is lower, however there can still be seen a significant excess above data.

4.1.3 Event Rates

Applying a 50 PE threshold cut inside a $1.6\ \mu s$ window reduces the cosmic-ray passing rate to 0.8%. With a 5 Hz beam rate, this corresponds to 135 cosmics passing per hour. The neutrino passing rate for this filter is about 22 events per hour. To further increase the neutrino to cosmic ratio, TPC topology cuts were implemented and will be discussed in the following section.

4.2 TPC Topology Selection

In order to further reduce the background of cosmic events, two independent selection streams using TPC wire data reconstruction was implemented. The first using 2D reconstructed clusters, and the second using 3D reconstructed tracks. Both streams look for neutrino interactions in the active TPC volume which are identifiable by two or more tracks originating from the same vertex.

Both 2D and 3D channels were optimized using monte carlo simulation which used a 128 kV cathode voltage. Passing rates were calculated using a 0.008 efficiency factor for cosmic events passing to simulate the flash finding described in section 4.1. This efficiency factor was an overestimation and was just used to get a general feel of what signal and background rates we would actually see in data.

909 4.2.1 Cosmic Tagging

910 The first step in TPC selection was based on the geometry of cosmic tracks in an event.
911 The cosmic ray muon geometry tagger runs on 3D tracks and assigns a score to each
912 reconstructed track on the likeliness of the track originating from a cosmic. The cosmic
913 scores are detailed below:

- 914 • 1: The track is tagged as entering or exiting the TPC
- 915 • 0.95: The track is a delta ray associated with a tagged track
- 916 • 0.5: The track is either entering or exiting, but not both
- 917 • 0.4: The track is entering or exiting through the Z boundary
- 918 • 0: The track isn't tagged

919 Clusters are assigned either a 0 or 1, 1 being a cosmic. In simulation, 90% of cosmics
920 are tagged as cosmics. These tracks are no longer considered when looking for a
921 neutrino topology. Requiring that the tracks be contained in turn affects the neutrino
922 efficiency by 20%. The algorithm checks that each track is contained within a boundary
923 region of 10 cm from all sides of the TPC. This boundary region was optimized via
924 handscanning of experimental data.

925 As can be expected, cosmic tagging is more efficient in the 3D channel (tracks) than
926 the 2D channel (clusters) because the reconstructed tracks can use the full 3D position
927 information of the entering and exiting points while the 2D channel mainly use the
928 reconstructed x position of the cluster which is associated to timing.

929 Cosmic tagging uses timing information to reject tracks and clusters that are outside
930 of drift window. The drift window for 128 kV is $1.6 \mu\text{s}$ while for 70 kV, the actual
931 voltage MicroBooNE is running at, is $2.3 \mu\text{s}$. Due to this variation between simulation
932 and data, we expect to see $2.3/1.6 = 1.44$ times more cosmic induced tracks or clusters
933 in the drift window.

934 4.2.2 2D Cluster Selection

935 This selection was spearheaded by myself and Katherine Woodruff. After looking at
936 experimental cosmics data, 2D clustering performs well, while 3D track reconstruction
937 is affected by more variations in simulation, for example noise filters. This was the

938 motivation for having a selection only on 2D clusters in the collection (Y) plane. As
 939 stated previously, the goal of this analysis was to find identifiable neutrino interactions
 940 for use in public event displays, in future analyses, the 3D track reconstruction has
 941 been modified to further increase the tracking efficiency and has more information
 942 that just the clusters. For this analysis, however, 2D cluster information was sufficient
 943 enough for neutrino selection.

944 **Primary Cuts**

945 The first cuts were used to select which clusters to consider. First the clusters must
 946 have at least ten hits on the collection plane and have a cosmic tagging score < 0.4.
 947 Only events that have at least two clusters that satisfy these primary cuts continue on.

948 After the initial cosmic tagging is applied, the following cuts are used to further
 949 separate identifiable neutrinos from background cosmics.

950 The next cut was to remove long, vertical clusters. This was applied after seeing
 951 that most cosmic induced clusters passing were long with high angles, while neutrino
 952 induced clusters were mainly forward going. We required a good cluster to either
 953 have a projected start angle less than 30 degrees from the z axis or be less than 200
 954 wires long. The length cut was added to make sure we don't cut any short high angle
 955 clusters that can correspond with a proton, or other highly ionizing particle associated
 956 with a long muon cluster. The 200 wire cut roughly equates to 0.6 m in the z direction,
 957 with a 3 mm wire pitch. Also, the projected angle is defined by $\tan \alpha = \Delta T / \Delta W$ where
 958 T is the time ticks and W is the wires.

959 The last cut requires the clusters to be either 30 time ticks or 30 wires. This cut was
 960 applied to reduce small delta rays associated with a cosmic without removing proton
 961 clusters associated with a long muon cluster, which saves ideal neutrino events that
 962 have both a long minimum ionizing muon like cluster and a short highly ionizing
 963 proton like cluster.

964 **Secondary Cuts**

965 The secondary cuts look to match long, low-angle clusters with short, high-charge
 966 clusters. Only clusters that have passed previous cuts are used. First clusters with
 967 length greater than 100 wires are chosen, which is approximately 0.3 m in the z

Cluster set	No Cuts	Primary Cuts	Secondary Cuts
Neutrinos only	570	303	32
Cosmics only (no flash)	308,016	291,879	602
Cosmics only (w/ flash)	2464	2335	5
Neutrinos/Cosmics	0.23	0.13	6.4

Table 4.1: Passing rates for 2D cluster cuts for neutrino on MC set and a cosmic only MC set. First column shows event rates with no cuts applied to both sets. Columns two and three show event rates after primary and secondary cuts are applied. Line three shows the second line scaled with the flash finding factor of 0.008. All events are normalized to per day assuming we are running at 5 Hz.

968 direction. Then we search for any cluster that is within approximately 3 cm (10 wires
 969 and 30 time ticks) away from the low-z end of the long cluster. This cluster must also
 970 be shorter than the first. In our reconstruction, the start and end point of a cluster can
 971 be swapped so both ends of the short cluster are compared to the long cluster.

972 Now that there is a vertex match, cuts based on charge and projected opening angle
 973 are implemented. We require the short cluster to have a higher start charge than the
 974 long cluster or the long cluster be longer than 500 wires. Start charge is defined as
 975 the charge on the first wire in ADC counts. The projected opening angle must also
 976 be between 11 and 90 degrees. This last cut is intended to remove clusters that are
 977 entirely overlapping or are part of the same long track. The resulting neutrino/cosmic
 978 event rate per day is shown in table 4.1. Figures 4.3 and 4.4 shows the percentages of
 979 clusters that pass each primary and secondary cuts.

980 4.2.3 3D Tracks and vertices Selection

981 The neutrino selection for the 3D channel was based on a reconstructed vertex and
 982 two tracks. All vertices and tracks were looped over that had a cosmic tag score < 0.4
 983 and the distances below were calculated:

- 984 • d : distance between the start points of the two tracks.
- 985 • d_1 : distance between vertex and start of track 1.
- 986 • d_2 : distance between vertex and start of track 2.

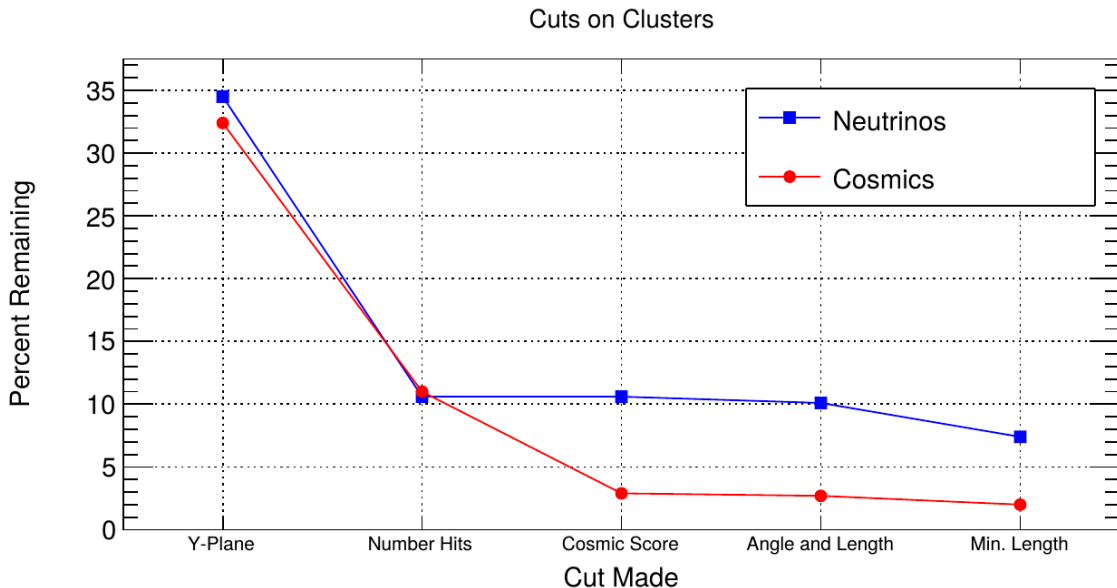


Figure 4.3: Percent of good clusters remaining for neutrinos and cosmics after the primary cuts were applied. This is relative to total number of initial clusters.

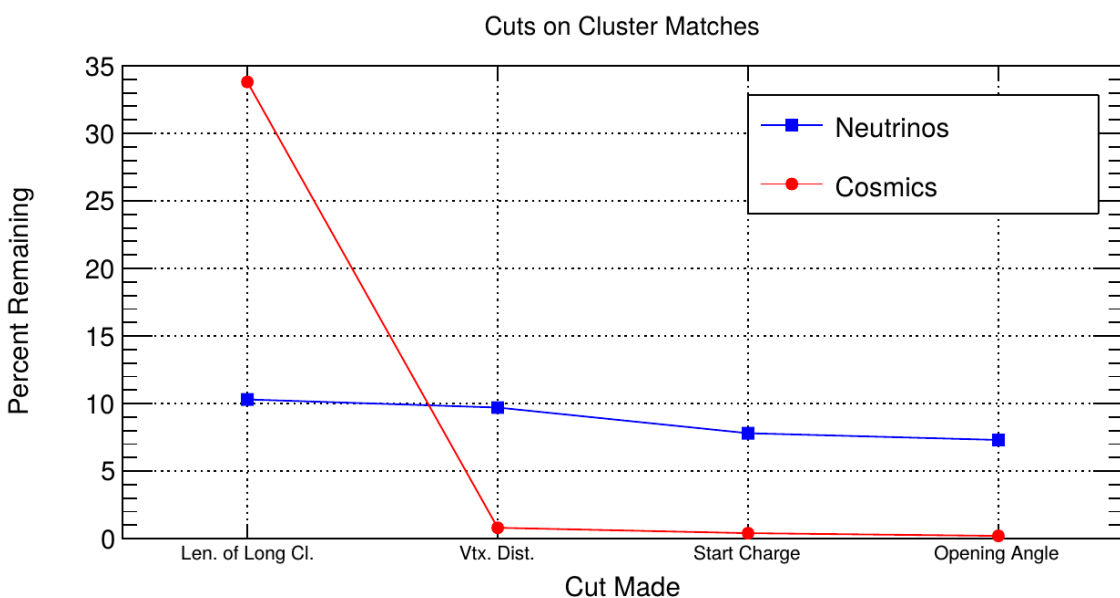


Figure 4.4: Percent matched cluster pairs remaining for neutrinos and cosmics after secondary cuts applied. This is relative to the number of events that contain clusters which pass the primary cuts.

987 The maximum distance of all three is then selected as the important characteristic per
988 trio. The best trio is the one that has the smallest maximum distance. The $\min(\max_d)$
989 for all trios in an event were plotted for BNB neutrino events and for cosmics to
990 find the best cut value for each tracking algorithm. The distribution of $\min(\max_{d,i})$
991 is smaller for neutrinos than for cosmics. The cut values for different tracking and
992 clustering algorithms are shown below. These cut values were chosen to minimize the
993 cosmic background to 20%.

- 994 • trackkalmanhit with cccluster $\min(\max_{d,i}) < 3$ cm.
- 995 • trackkalmanhit with pandoraNu $\min(\max_{d,i}) < 4.5$ cm.
- 996 • pandoraNu with cccluster $\min(\max_{d,i}) < 5$ cm.

997 4.2.4 TPC Updates

998 After doing a visual hand-scanning of the first beam data processed with the filters
999 detailed above, the events passing had a larger contamination of background than
1000 expected. This was mainly in part due to the reconstruction performing better on
1001 simulation than on data. Due to this, additional cuts on both streams needed to be
1002 implemented in order to increase signal/background ratio. These cuts were added on
1003 top of the filters described above and further reduce the event count.

1004 2D Filter Updates

1005 The main background observed in the 2D filter were Michel events, where the muon
1006 and electron formed two connected clusters. These events were rejected by comparing
1007 the start and end charge deposition of the long cluster (i.e muon particle). The start
1008 charge deposition must be less than the end charge deposition. This cut is implemented
1009 because muons have a higher ionizaiton loss at the end.

1010 3D Filter Updates

1011 It was seen that cosmic tracks can often originate or end at the same point, therefore
1012 faking a signal. Cosmic tracks, however, are mostly vertical. By requiring the angle
1013 of the longer track have a cosine greater than 0.85 with respect to the z-axis as well

₁₀₁₄ as requiring the longer track to have a length greater than 10 cm, we can reduce this
₁₀₁₅ background.

₁₀₁₆ **4.3 Conclusion**

₁₀₁₇ After proccesing these filters in parallel, it was shown that the 3D filter had a higher
₁₀₁₈ purity than the 2D filter because of the higher cosmic rejection being used due to 3D
₁₀₁₉ reconstruction. The 2D filter is blind to track entering/exiting from the top or bottom
₁₀₂₀ of the TPC. Although the 3D filter had a higher purity, the 2D filter was still able to
₁₀₂₁ find identifiable events in data that were used as public event displays. A sample of
₁₀₂₂ event displays are shown in figures 4.5 and 4.6.

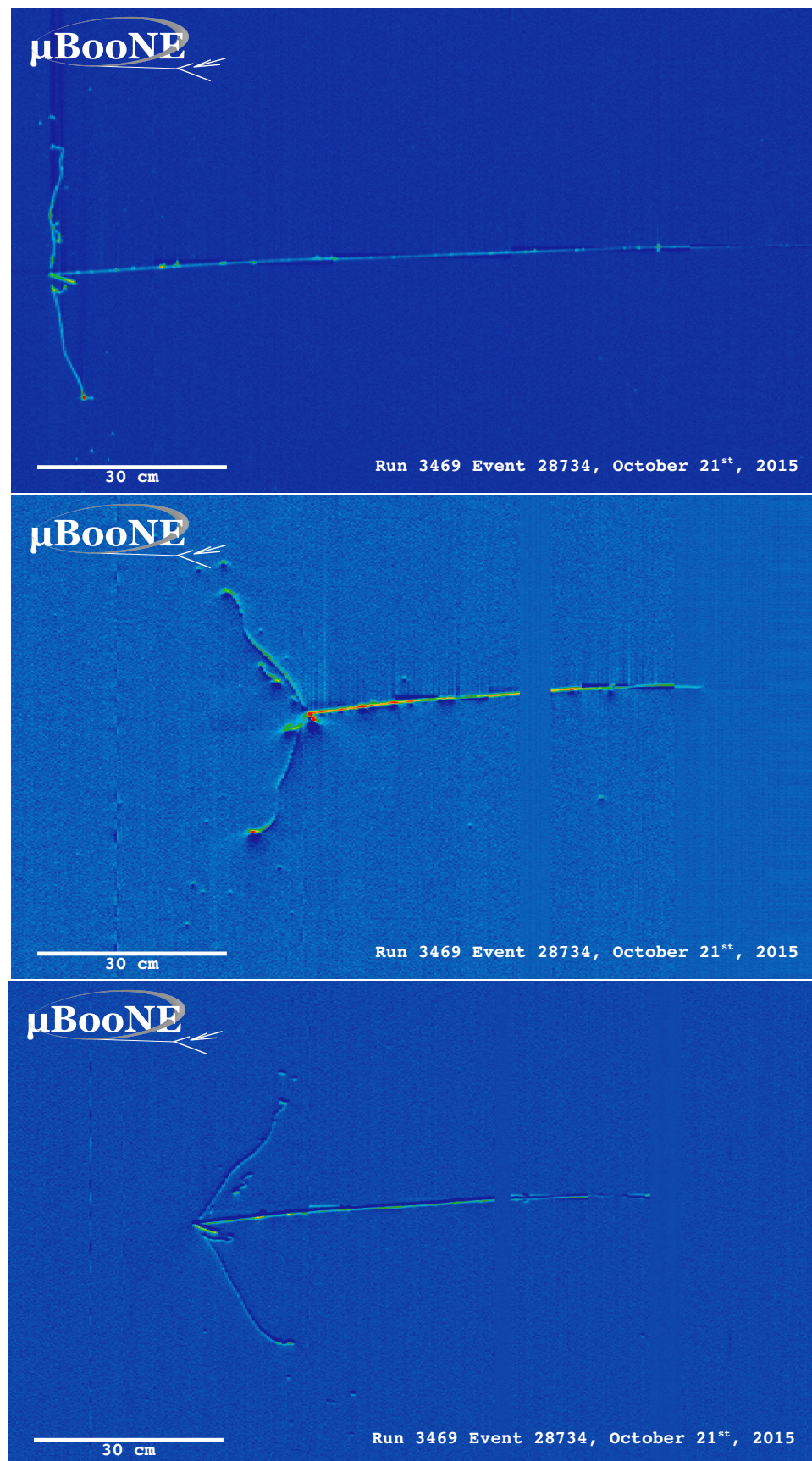


Figure 4.5: First Neutrino Interaction Candidate Events from MicroBooNE

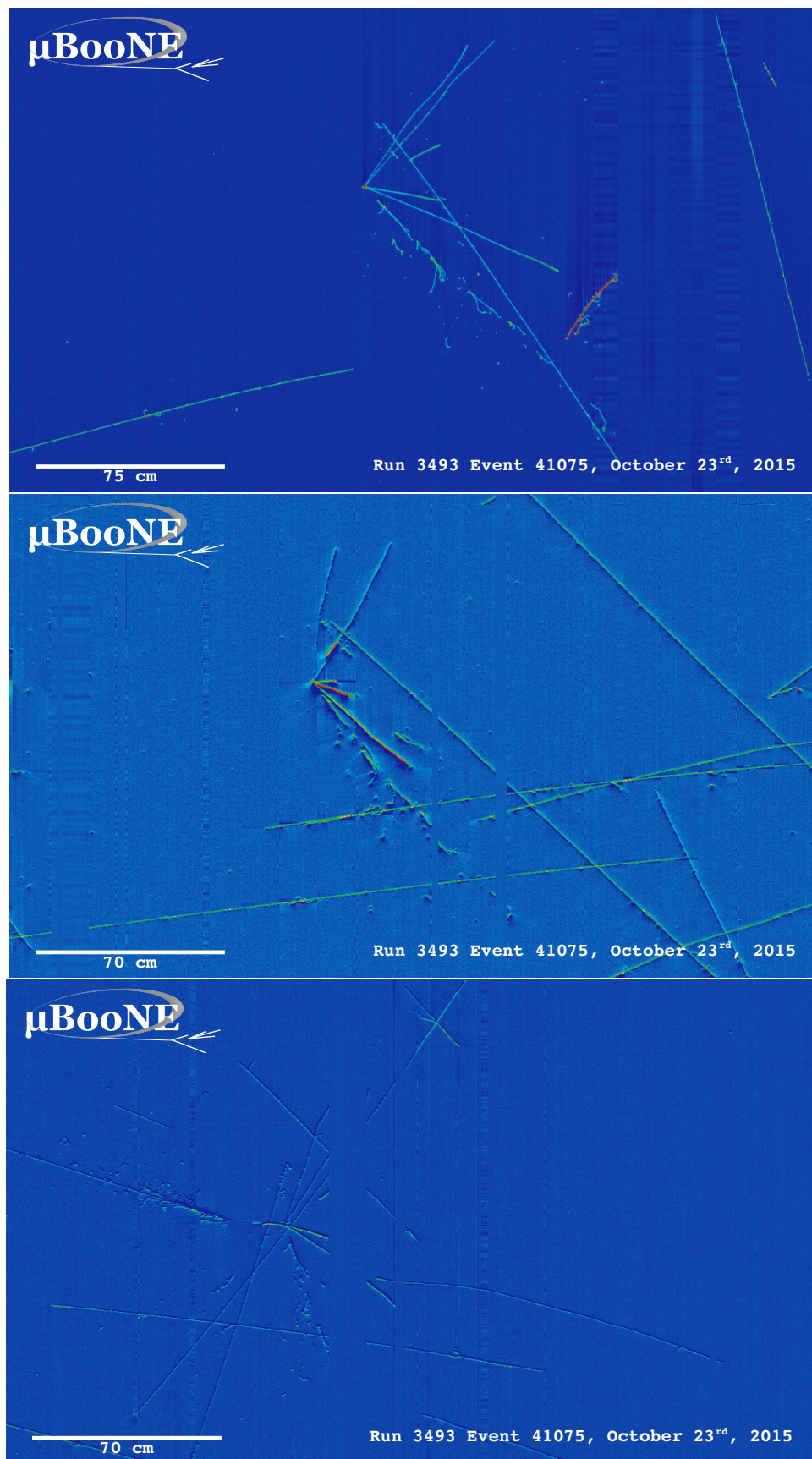


Figure 4.6: First Neutrino Interaction Candidate Events from MicroBooNE

1023 **Chapter 5**

1024 **CC-Inclusive Cross Section Selection**

1025 **Filter**

1026 The CC-Inclusive cross-section selection I and selection I modified filters used in this
1027 analysis will be described in the following sections below. These filters are an expansion
1028 of the Neutrino ID filter. The work done in this thesis was to further improve these
1029 selections by increasing both efficiency and purity as well as increasing acceptance
1030 without further affecting the kinematic distributions of the selected neutrino events.

1031 MicroBooNE requires fully automated event reconstruction and selection algorithms for use in the many physics measurements being worked on to date due to
1032 the large data rate MicroBooNE receives. Being able to automatically pluck out the
1033 neutrino interaction among a sea of cosmics proved to be challenging but was accomplished.
1034 MicroBooNE has developed two complementary and preliminary selection
1035 algorithms to select charged-current $\nu_\mu - Ar$ interactions. Both are fully automated
1036 and cut based. The results of this thesis will focus on selection I and selection I modified
1037 and will focus on further improving these algorithms using Convolutional Neural
1038 Network (CNN) implementations. These selections identify the muon from a neutrino
1039 interaction without biasing towards track multiplicity. To combat cosmic and neutral
1040 current background, the analysis is strongly biased towards forward-going long tracks
1041 which are contained. This limits phase space and reduces acceptance.
1042

1043 5.1 Data and MC Processing Chain

1044 The data used for this analysis were based on hardware and software triggers. Events
1045 used came from the *BNB_INCLUSIVE* and *EXT_BNB_INCLUSIVE* streams and were
1046 used for signal and background. The *BNB_INCLUSIVE* stream is chosen by requiring
1047 that the hardware trigger bit is fired and that the event passed an optical software
1048 trigger within a BNB spill timing window. The *EXT_BNB_INCLUSIVE* stream requires
1049 the EXT hardware trigger to fire as well as pass the same optical software trigger
1050 within a BNB spill size timing window similar to the *BNB_INCLUSIVE*.

1051 The two MC samples used in this analysis and for determining selection efficiencies
1052 and purities were GENIE BNB neutrino interactions with CORSIKA cosmic ray overlay
1053 within the readout window and inTime CORSIKA cosmic rays. The MC samples
1054 generated used *uboonecode v04_36_00* and are based on the following packages:

- 1055 • larsoft v04_36_00
- 1056 • GEANT v04_09_06_p04d
- 1057 • GENIE v02_08_06d
- 1058 • GENIE xsec v02_08_06a
- 1059 • pandora v02_03_0a
- 1060 • CORSIKA v07_4003

1061 Both data and MC samples were processed using the same reconstruction release,
1062 *uboonecode v05_08_00* and the fcl files used for reconstruction are listed below:

- 1063 • MC fcl files
 - 1064 – reco_uboone_mcc7_driver_stage1.fcl
 - 1065 – reco_uboone_mcc7_driver_stage2.fcl
- 1066 • Data fcl files
 - 1067 • reco_uboone_data_Feb2016_driver_stage1.fcl
 - 1068 • reco_uboone_data_Feb2016_driver_stage2.fcl

1069 On top of the hardware and software triggers, the data also had to pass more
1070 criteria to be identified as part of the good run list. The criteria is detailed below.

- 1071 • **Detector conditions:** the detector has to be in a good operating condition. The
1072 detector conditions are read from the slow monitoring database and are required
1073 to be within the alarm thresholds. The variables of interest for events passing
1074 the good run list criteria include DAQ, PMT, HV, Drift HV, wire bias, electron
1075 lifetime and detector power. These conditions need to be met on a run-by-run
1076 basis in order to pass the selection.
- 1077 • **Data quality:** normal and stable behavior for basic reconstruction quantities.
1078 These reconstruction variables include average number of tracks, hits, and flashes
1079 in each event, the average length of tracks, the average amplitude and area of
1080 hits, the average PE and the average spread of each one of these quantities.
- 1081 • **Beam Conditions:** the BNB must be on and stable and the POT per spill needs
1082 to above the intensity threshold. Beam quality conditions include checking the
1083 fraction of proton beam interacting within the target, the horn current, and the
1084 intensity of protons per spill. The final sample is $5 * 10^{19}$ and a per-spill intensity
1085 of $4 * 10^{12}$
- 1086 • **Run processed:** the full run must be processed completely without missing
1087 subruns or crashes in the data processing.

1088 5.2 Normalization of data and MC

1089 The off-beam sample is used to measure beam unrelated backgrounds. For normalization
1090 one needs the total number of BNB spills (N_{BNB}) and the total number of external
1091 triggers. The BNB spills used need to pass the beam quality cuts. The normalization
1092 factor is then N_{BNB}/N_{EXT} which is 1.23.

1093 To normalize generated BNB MC events to POT, we used the following:

- 1094 • $5 * 10^{19} POT = 41524.3$ generated events

1095 where this scaling factor only applies to mcc7 generated events. The inTime cosmic
1096 sample is normalized with respect to the open cosmic sample so an understanding
1097 of both is necessary. The POT per beam spill for mcc7 BNB samples is $5 * 10^{12}$. To
1098 calculate how many spills are necessary to produce a specific POT one would multiply
1099 the total POT by the average 1/POT per spill. For a total POT of $5 * 10^{19}$ the amount
1100 of spills necessary is $\frac{5 * 10^{19}}{5 * 10^{12}} = 1 * 10^7$. This is only one in ~ 241 events therefore each

cosmic event needs to be scaled up by a factor of 240.8 when comparing to BNB MC. For inTime cosmics however, two filters are applied to reduce computing and processing time and only leave cosmics that will interact within the detector. The passing rate after these two filters is 0.02125, therefore the total inTime cosmic scaling factor to compare inTime cosmics to BNB is $0.02125 * 240.8 = 5.12$.

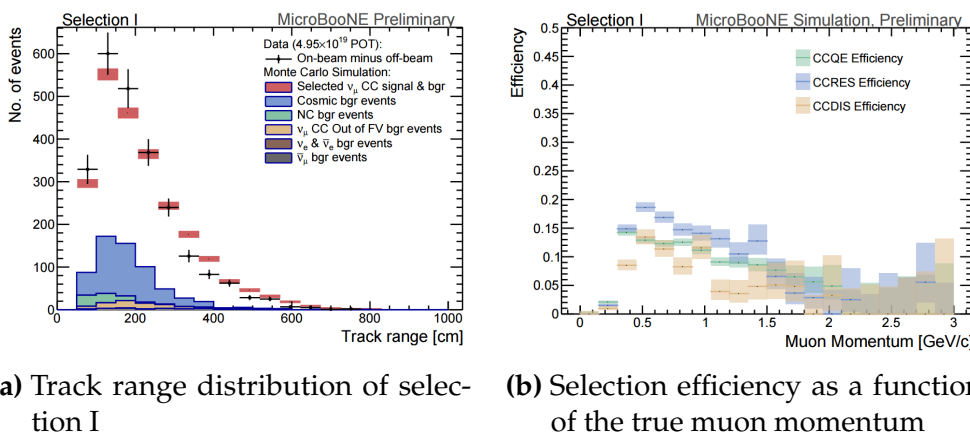


Figure 5.1: 5.1a Track range distribution for selection I. The track range is defined as the 3D distance between the start and end of the muon candidate track. No data is shown below 75 cm due to the track length cut described previously. 5.1b Efficiency of the selected events by process quasi-elastic (QE), resonant (RES), and deep-inelastic (DIS). Statistical uncertainty is shown in the bands and the distributions are a function of true muon momentum. The rise of the efficiency between 0 GeV and 0.5 GeV is due to the minimum track length cut and the decreasing efficiency for higher momentum tracks is caused by the containment requirement.

5.3 Optical Software Trigger and Reconstruction

5.3.1 Software Trigger

Most of the BNB spills from the accelerator do not have a neutrino interaction in MicroBooNE. To save computation resources and reduce data-rates, we require a burst of light in the light collection system in coincidence with the 1.6 μ s beam spill. Requiring light activity in coincidence with the beam spill eliminates the vast majority of triggers with no neutrino interaction in the detector, however, it doesn't guarantee the activity in the detector is a neutrino interaction since a cosmic ray can interact in coincidence with the beam spill as well.

1115 To implement this, a software trigger was used on the PMT waveforms to decide
1116 whether or not to keep that event. The software trigger is implemented after the event
1117 builder combines data from the PMTs and triggers into a single event. The software
1118 trigger uses the digitized output of the 32 PMT channels in the light collection system.
1119 Only the waveform region in coincidence with the beam spill is used to search for
1120 possible triggers. For each PMT, a waveform is found by taking the difference of ADC
1121 values is calculated between t and $t + s$. This waveform is then scanned for ADC
1122 values above a threshold X_0 . Once an ADC is above this threshold, a discriminator
1123 window is opened for a fixed number of time ticks (W_0). If the ADC count within this
1124 window W_0 is greater than a second larger threshold X_3 , a final window of width W_3
1125 is opened. The max ADC value within this final window is set as the peak amplitude
1126 for the PMT and then summed across all 32 PMTs and set to the variable PHMAX. The
1127 software trigger places a final cut on the PHMAX variable to decide whether or not
1128 to keep the event. The thresholds were found by the Trigger task force using Monte
1129 Carlo Studies and are as follows:

- 1130 • $X_0 = 5$ ADC
- 1131 • $X_3 = 10$ ADC
- 1132 • $W_0 = 6$ Ticks
- 1133 • $W_3 = 6$ Ticks
- 1134 • PHMAX cut = 130 ADC

1135 5.3.2 Flash Reconstruction

1136 MicroBooNE collects light from each of the 32 PMTs either in a continuous readout
1137 window of $23.4 \mu\text{s}$ activated by a beam gate signal on the trigger board, or in discrimi-
1138 nated pulses of $\sim 1 \mu\text{s}$ duration activated if the ADC count for any PMT goes above 80
1139 ADC count. These two formats are saved as output waveforms and put onto an event.
1140 Additionally, each PMT can provide two output streams, high-gain (~ 20 ADC/PE)
1141 and low-gain (~ 2 ADC/PE) channels. The first step in the reconstruction is to merge
1142 both these channels into a “saturation corrected waveform” which uses information
1143 from the low-gain waveform to correct for saturating high-gain pulses.

1144 The saturation corrected waveform in the continuous readout window is used to
1145 reconstruct optical hits. Each PMT’s waveform is scanned for hits then a threshold

1146 based hit reconstruction algorithm is applied which requires pulses of a minimum
1147 area in order to be reconstructed. Each reconstructed hit is associated to a PMT, a time
1148 in μs , and a PE count.

1149 Once hits are reconstructed for all 32 PMTs, all PMT information is then combined
1150 into optical flashes which represent optical information seen by the PMTs from interac-
1151 tions in the detector. Each flash has information on total light seen per interaction, the
1152 distribution of the light across all 32 PMTs, the flash time with respect to the trigger
1153 time of the flash, and lastly, the spacial information of the flash in Y-Z plane of the
1154 detector. These flashes are reconstructed by requiring that there is a $\sim 1 \mu\text{s}$ coincidence
1155 between the reconstructed hits in all 32 PMTs. The total PE is summed up among
1156 all coincident hits across the PMTs and if the total PE is greater than 2 PE, a flash is
1157 reconstructed. There are also safe guards in place to take care of late scintillation light.

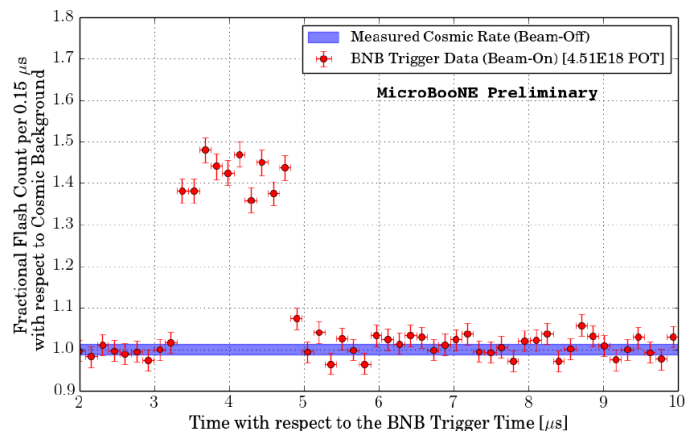


Figure 5.2: Time distribution of reconstructed optical flashes with a PE value of 50 or more for a sample of BNB unbiased triggered events.

1158 Figure 5.2 shows the time distribution of reconstructed optical flashes using the
1159 BNB continuous stream. You can see a clear excess in coincidence with the expected
1160 arrival time of neutrinos. The same flash reconstruction that was used in the cc-
1161 inclusive filter detailed here was used to create this plot in data.

1162 5.3.3 Beam Window

1163 Figure 5.3 shows the distribution of flashes for on-beam, off-beam and various MC
1164 samples. The software trigger has been applied to these samples. The pile-up seen just
1165 after 0 μs is a feature of the flash finding algorithm and consists of low PE flashes and

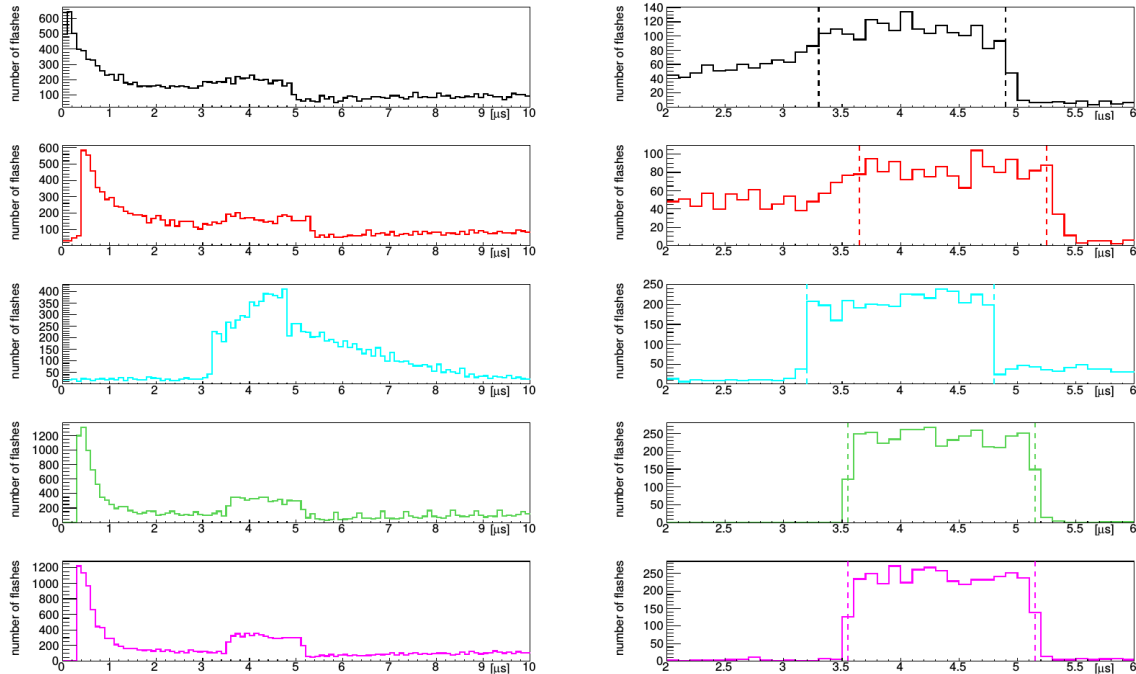


Figure 5.3: Flash time distribution for all flashes (left plot) and flashes $> 20\text{PE}$ (right plot). The different curves are as follows: on-beam data (black), off-beam data (red), CORSIKA inTime MC (light blue), BNB only MC (green), and BNB+Cosmic MC (purple). The dashed vertical lines mark the time window that was chosen for each sample

1166 is removed in the second column of distributions with a low 20 PE threshold cut. The
1167 plots show that the time window for the distributions are shifted a small amount from
1168 each-other. This is caused by different hardware configurations per sample. Using
1169 these distributions, the windows chosen per sample are as follows:

- 1170 • On-Beam: 3.3 to 4.9 μ s
- 1171 • Off-Beam: 3.65 to 5.25 μ s
- 1172 • CORSIKA inTime: 3.2 to 4.8 μ s
- 1173 • BNB only: 3.55 to 5.15 μ s
- 1174 • BNB+Cosmic: 3.55 to 5.15 μ s

1175 Each window has a width of 1.6 μ s.

1176 5.4 TPC Reconstruction

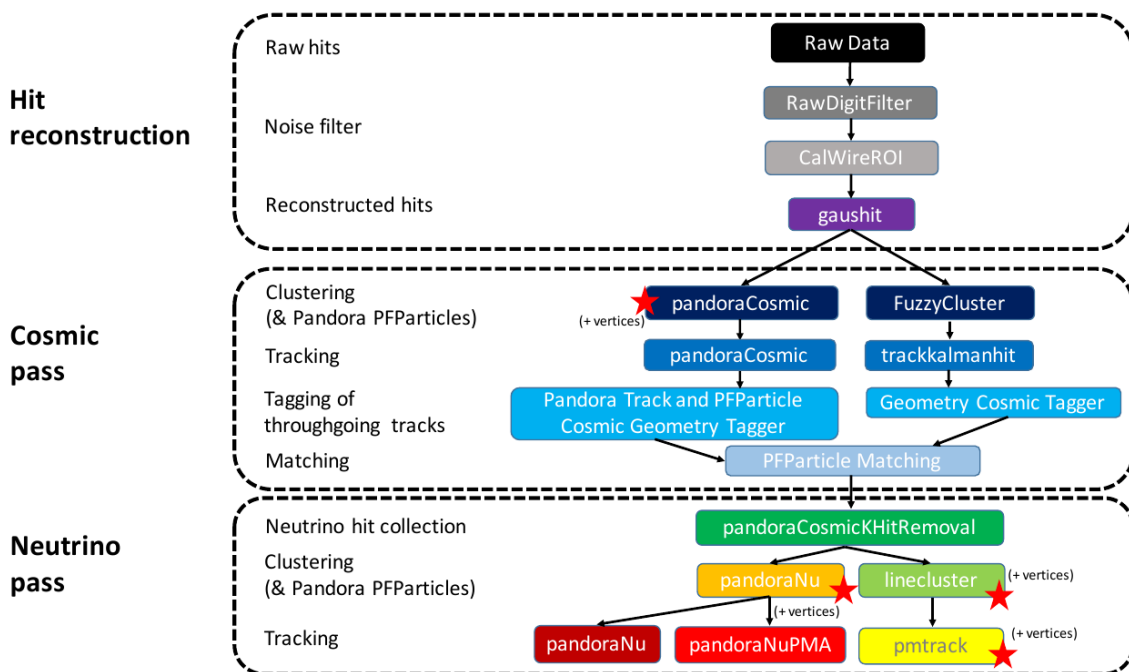


Figure 5.4: Reconstruction chain run on both data and MC. The red stars mean that the algorithm returns reconstructed 3D vertices.

1177 Figure 5.4 summarizes the reconstruction chain applied to both MC and data for
1178 this analysis. After the hit reconstruction, a cosmic pass is applied which removes all
1179 hits associated to through-going tracks. A description of these TPC reconstruction
1180 algorithms will be detailed below.

1181 **5.4.1 Hit Reconstruction**

1182 The waveforms used for hit reconstruction consist of charge deposited on the sense
1183 wire in drift time. The first step in hit reconstruction is to pass the waveforms through
1184 a filtering algorithm to filter out the noise introduced from the electronics. The input
1185 waveforms are also truncated from 9600 time ticks to 6400 time ticks in this first step
1186 to reduce the data footprint of these waveforms.

1187 Once noise filtering is complete, a deconvolution algorithm is applied to the wave-
1188 forms to remove the drift field and electronics response, therefore leaving only the
1189 ionized electrons kicked off the argon atoms by an incident track. During this process,
1190 Region of Interests (ROI) are identified and cut out of the waveforms to further reduce
1191 the data volume.

1192 The hit finding algorithm then finds candidate peaks in these ROI's and fits the
1193 peaks to Gaussian curves. These Gaussian shaped peaks are now called hits and
1194 represent the charge deposition on a wire by the incoming track. These hit objects
1195 have a peak time and width and are the basic object input to further algorithms down
1196 the reconstruction chain.

1197 **5.4.2 Clustering**

1198 There are multiple clustering algorithms used in this analysis. The main purpose of all
1199 the clustering algorithms is to associate hits together in 2D space to create objects like
1200 tracks, vertices and showers. For the fuzzy cluster algorithm, three steps are used to
1201 achieve this. The first step is to associate hits to each-other using a fuzzy clustering
1202 algorithm which gives each hit a degree of belonging to the cluster. Second, a Hough
1203 transform is used to find hits associated to candidate tracks and showers within each
1204 of the clusters found in the first step. The last step merges smaller candidate tracks
1205 and showers into large clusters. The last step also associates unclustered hits into

1206 nearby objects which helps shower reconstruction. The result is a set of clusters made
1207 up of associate hits that represent tracks or showers per plane.

1208 The pandora algorithm utilizes it's own clustering algorithm and will be detailed
1209 in the next section. The last clustering algorithm is called linecluster. The linecluster
1210 algorithm reconstructs 2D linear clusters per plane by fitting a line onto nearby hits
1211 which is then extrapolated to neighboring wires. 2D vertices are found per plane by
1212 using the intersection points of the ends of nearby clusters. These 2D vertices are then
1213 matched in time across all three planes to get a 3D vertex in space.

1214 5.4.3 Pandora

1215 5.4.4 Trackkalmanhit

1216 The trackkalmanhit algorithm takes 2D clusters returned from the fuzzy cluster algo-
1217 rithm and outputs track objects. There are no hierarchy structure as it is in pandora,
1218 each track is independent. There also is no vertex reconstruction with this algorithm
1219 as well.

1220 5.4.5 Cosmic Hit Removal

1221 The Pandora algorithm is applied to the events twice, the first to remove downward
1222 going tracks primarily from cosmic ray muon like particles. The second pass only runs
1223 on a subset of hits that aren't associated with cosmic ray muon tracks.

1224 After the first pass, the output of PFParticle hierarchy is then passed to a cosmic
1225 ray tagger to look through all hits to determine start and end points. If the start or
1226 end point trajectories are consistent with entering or exiting the TPC, then these hits
1227 are removed from the second pass. Hits are considered entering or exiting the TPC
1228 if the drift time are outside of the neutrino drift window or outside of the fiducial
1229 volume of the TPC. The fiducial volume was based on a montecarlo study and is 20
1230 cm from the top or bottom of the TPC and 10 cm from the TPC ends. Hits associated
1231 with candidate cosmic ray tracks are removed from the input hit collection and the
1232 remaining hits are passed to the neutrino optimized pass of Pandora.

1233 5.4.6 Projection Matching Algorithm

1234 The projection matching algorithm (PMA) was inherited from ICARUS and has been
1235 implemented in LArSoft. PMA differs from traditional LArSoft 3D reconstruction
1236 algorithms. Most 3D reconstruction attempts to match 2D objects from all three planes
1237 by drift time, while the PMA algorithm projects a track hypothesis on each plane
1238 then the distance between this projection and the hits on each plane is minimized
1239 simultaneously. More information can be found in [?].

1240 5.5 Event Selection

1241 The first requirement for selecting ν_μ CC events is that the event has at least one
1242 scintillation light flash in the beam trigger window with more than 50 PE on all PMTs
1243 combined. From the flashes that pass, the most intense is chosen and considered to be
1244 originating from a neutrino interaction and will be the only flash used in further cuts.

1245 Vertices are then required to have at least one reconstructed track start or endpoint
1246 within a 5 cm radius. Showers associated with a vertex do not pass this cut. All
1247 tracks associated with a vertex are then used to calculate a track length weighted
1248 average of the θ -angle. Of all the vertices that do pass, only the vertex with the most
1249 forward going θ -angle average of all associated tracks is considered the neutrino vertex
1250 candidate. The most forward going θ -angle average is chosen by picking the largest
1251 track range weighted average of $|\cos(\theta)|$, seeing as $\cos(\theta) = 1$ is the beam direction.
1252 Next, it is required that the reconstructed neutrino vertex candidate be within the
1253 fiducial volume as well as within the drift time starting at t_0 . The fiducial volume
1254 boundaries chosen are 10 cm from the edges of the TPC in x and z which is the drift
1255 direction and beam direction respectively, and 20 cm from the edges of the TPC in y
1256 which is the vertical direction. For all further cuts, only the longest track associated
1257 with the neutrino vertex candidate and this track is assumed to be the muon candidate
1258 of the neutrino event.

1259 The next cut requires the position of the flash in the z-direction and the track z-
1260 projection to be compared. This basic flash matching algorithm is rudimentary and a
1261 placeholder for a more sophisticated algorithm. The z-position of the flash needs to be
1262 within 80 cm to the z-positions of track start or endpoints. If the flash is between the
1263 track start and endpoint, the distance of the flash to the track is considered to be 0 cm.

1264 Lastly, the track needs to be fully contained within the fiducial volume and have a
1265 track range greater than 75 cm. The range is the 3D distance between the track's start
1266 and endpoint. The length cut was optimized to remove NC background that contain
1267 a pion due to the pion interaction rate to be ~ 70 cm. A track that makes all the cuts
1268 is considered to be the muon of a ν_μ CC event. The list of cuts for this selection is
1269 described below:

- 1270 1. At least one flash > 50 PE within the beam gate.
- 1271 2. At least one track within 5 cm around a vertex.
- 1272 3. Vertex with flattest tracks is chosen to be vertex candidate.
- 1273 4. Vertex candidate in fiducial volume.
- 1274 5. Longest track associated with vertex candidate is chosen to be track candidate.
- 1275 6. Longest track is within 80 cm (z-axis only) of the flash.
- 1276 7. Longest track is fully contained.
- 1277 8. Longest track is greater than 75 cm.

1278 The event selection scheme can also be seen in figure 5.5. Table 5.1 lists the passing
1279 rates for MC events for the selection scheme described above. Table 5.2 lists the passing
1280 rates for on-beam and off-beam data for the selection scheme. The normalization
1281 factors applied between on-beam and off-beam data are described in section 5.2.

1282 5.5.1 Expected Backgrounds

1283 Most of the selected background events will be of cosmic origin. There are two types
1284 of cosmic background, one triggered by a cosmic-ray event occurring in the beam
1285 gate time window, the other triggered by a beam induced interaction in the cryostat
1286 followed by a misidentification of a cosmic event as a neutrino event. The first
1287 cosmic background can be subtracted from the selected events using the off-beam
1288 BNBEXT sample normalized to the on-beam. The second cosmic background events
1289 are modeled by MC by using BNB+Cosmic MC sample.

1290 Other backgrounds originate from neutrino beam contaminants. A major contribution
1291 in this sector is by neutral current neutrino events for example a charged pion track
1292 misidentified as a muon. Another contribution are ν_e -like and anti-muon-neutrino

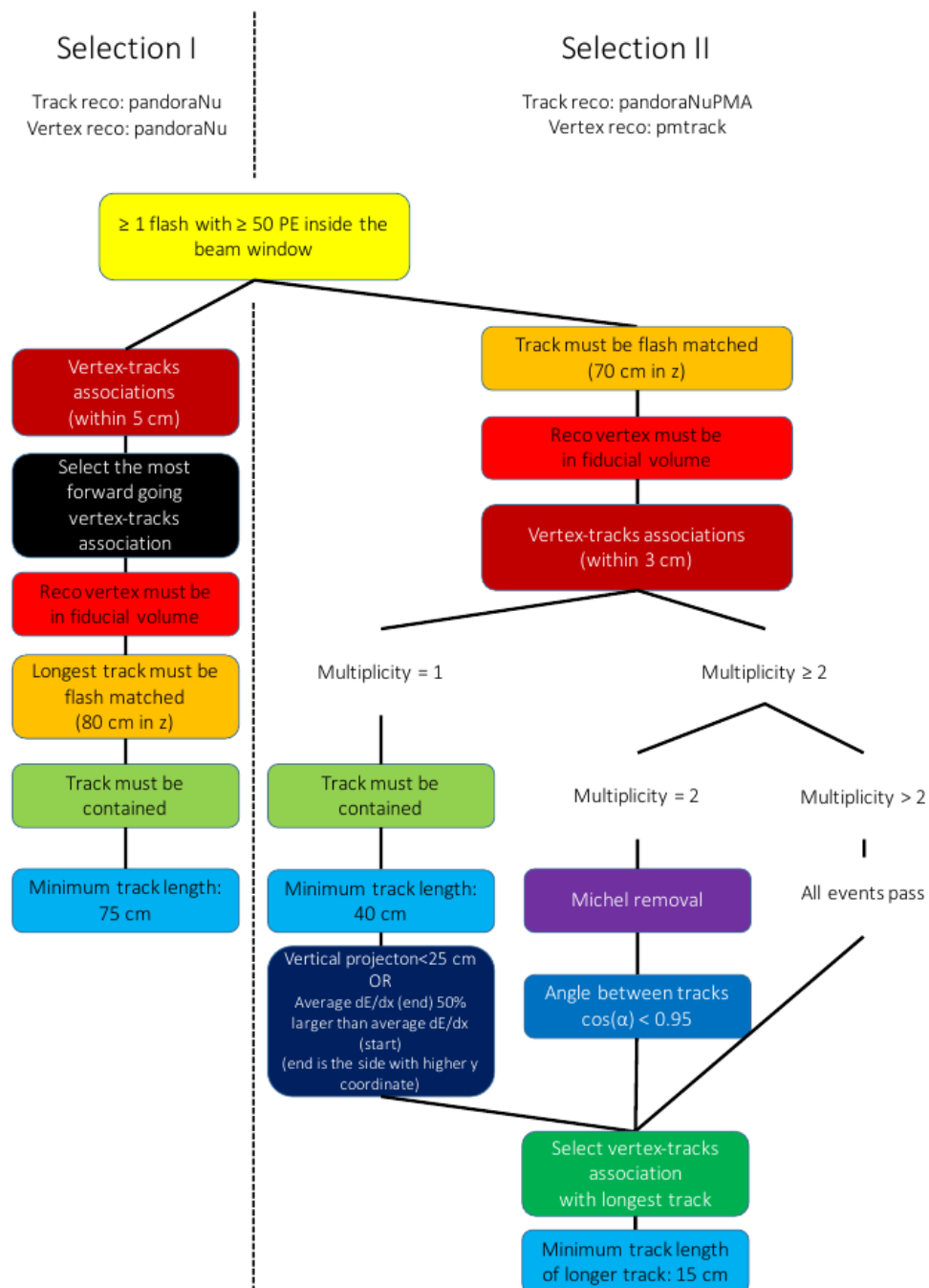


Figure 5.5: Event selection diagram for selection I and selection II. This analysis focused on optimizing selection I. Boxes with the same color across the two selections symbolize similar cuts.

	BNB+Cosmic Selection	BNB+ Cosmic MC-Truth	Cosmic Only	Signal:Cosmic Only
Generated Events	191362	45273	4804	1:22
≥ 1 flash with ≥ 50 PE	136219 (71%/71%)	44002 (97%/97%)	2970 (62%/62%)	1:14
≥ 1 track within 5 cm of vertex	135830 (99%/71%)	43974 (99%/97%)	2975 (99%/62%)	1:14
vertex candidate in FV	79112 (58%/41%)	34891 (79%/77%)	1482 (50%/31%)	1:8.9
flash matching of longest track	40267 (51%/21%)	25891 (74%/57%)	340 (23%/7.1%)	1:2.8
track containment	19391 (48%/10%)	11693 (45%/26%)	129 (38%/2.7%)	1:2.3
track ≥ 75 cm	6920 (36%/3.6%)	5780 (49%/13%)	17 (13%/0.4%)	1:0.6

Table 5.1: Passing rates of Selection I. Numbers are absolute event counts and cosmic background is not scaled. The BNB+Cosmic sample contains all events, not just ν_μ CC inclusive. The numbers in brackets give the passing rate wrt the step before (first percentage) and wrt total generated events (second percentage). The BNB+Cosmic MC-Truth column shows how many true ν_μ CC inclusive events are left in the sample. This number includes mis-identifications where a cosmic track is picked by the selection instead of the neutrino interaction in the same event. The cosmic only sample is used just to illustrate the cut efficiency. The last column Signal:Cosmic only gives an estimate of the ν_μ CC events wrt the cosmic only background at each step. For this number, the cosmic background has been scaled as described in section 5.2.

	on-beam	off-beam
Generated Events	546910	477819
≥ 1 flash with ≥ 50 PE	135923 (25%/25%)	96748 (20%/20%)
≥ 1 track within 5 cm of vertex	134744 (99%/25%)	95778 (99%/20%)
vertex candidate in FV	74827 (55%/14%)	51468 (54%/11%)
flash matching of longest track	22059 (29%/4.0%)	12234 (24%/2.6%)
track containment	10722 (49%/1.9%)	5283 (43%/1.1%)
track ≥ 75 cm	3213 (30%/0.6%)	1328 (25%/0.3%)

Table 5.2: Passing rates for Selection I selection applied to on-beam and off-beam data. The numbers in brackets give the passing rate wrt the step before (first percentage) and wrt the generated events (second percentage). Off-beam data has been scaled with a factor 1.23 to normalize to the on-beam data stream.

1293 events. These beam related backgrounds are an order of magnitude smaller than the
1294 cosmic misidentification backgrounds. These backgrounds can not be subtracted and
1295 are estimated using MC truth.

1296 The efficiency and purity of Selection I are calculated below:

- 1297 • Efficiency: Number of selected true ν_μ CC events divided by the number of
1298 expected true ν_μ CC events with interaction in the FV.

1299 – $(12.3 \pm 3.4) \%$

- 1300 • Purity: Number of selected true ν_μ CC events divided by the sum of itself and
1301 the number of all backgrounds.

1302 – $(53.8 \pm 4.4) \%$

1303 **5.5.2 Truth Distributions**

1304 The truth distributions of MC truth variables before and after the selection are detailed
1305 in this section. The overall efficiencies are calculated for all ν_μ CC signal events
1306 with a true interaction within the fiducial volume and a fully contained muon track
1307 originating from said vertex. Figures 5.6 through 5.8 detail the truth distributions for
1308 muon momentum, $\cos(\theta)$ and ϕ and figures 5.9 through 5.11 detail the total efficiency
1309 of the selection for charged current quasi elastic (CCQE) events, charged current
1310 resonant (CCRES) events, and charged current deep inelastic (CCDIS) events.

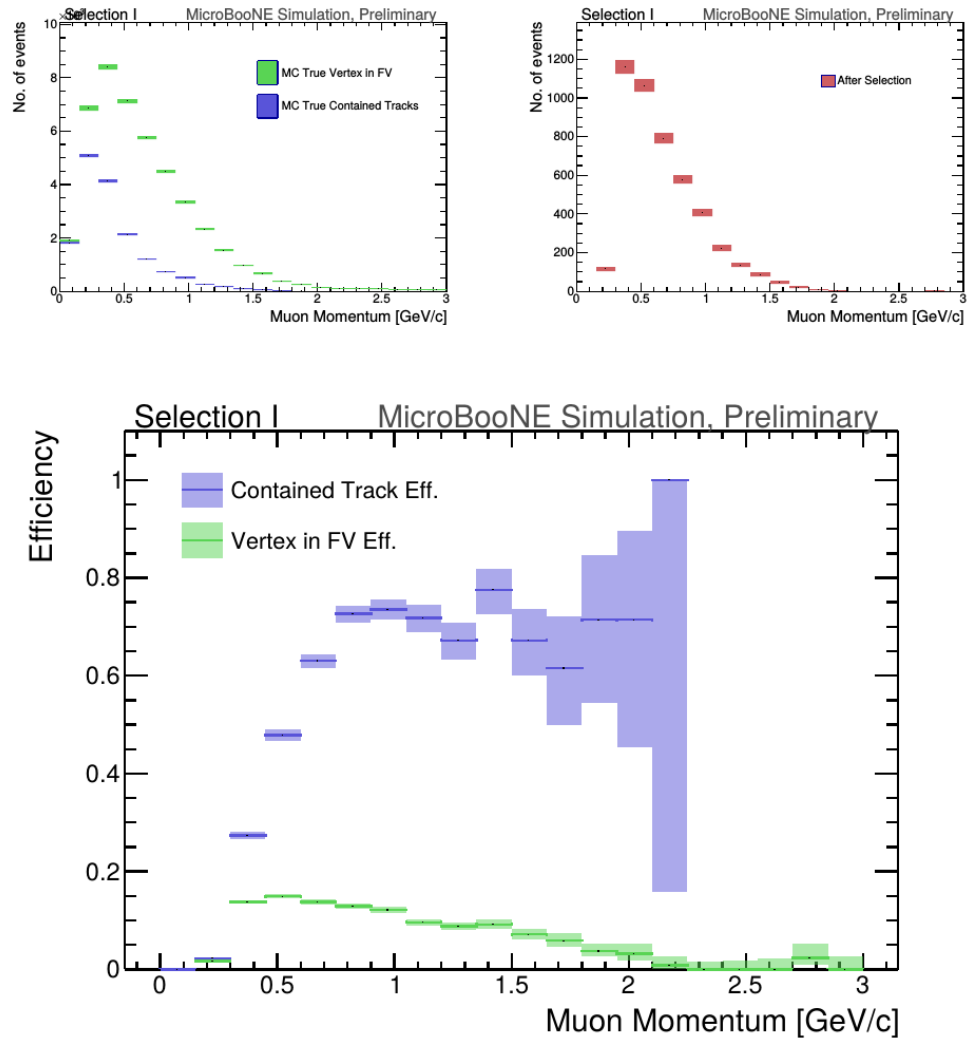


Figure 5.6: MC momentum distributions of the muon originating from a ν_μ CC interaction. Upper left is the momentum distributions of events with a vertex within the FV (green) and the events with a fully contained track (blue) before the selection. The upper right side is the momentum distribution after the selection (red). The lower plot is the selection efficiencies.

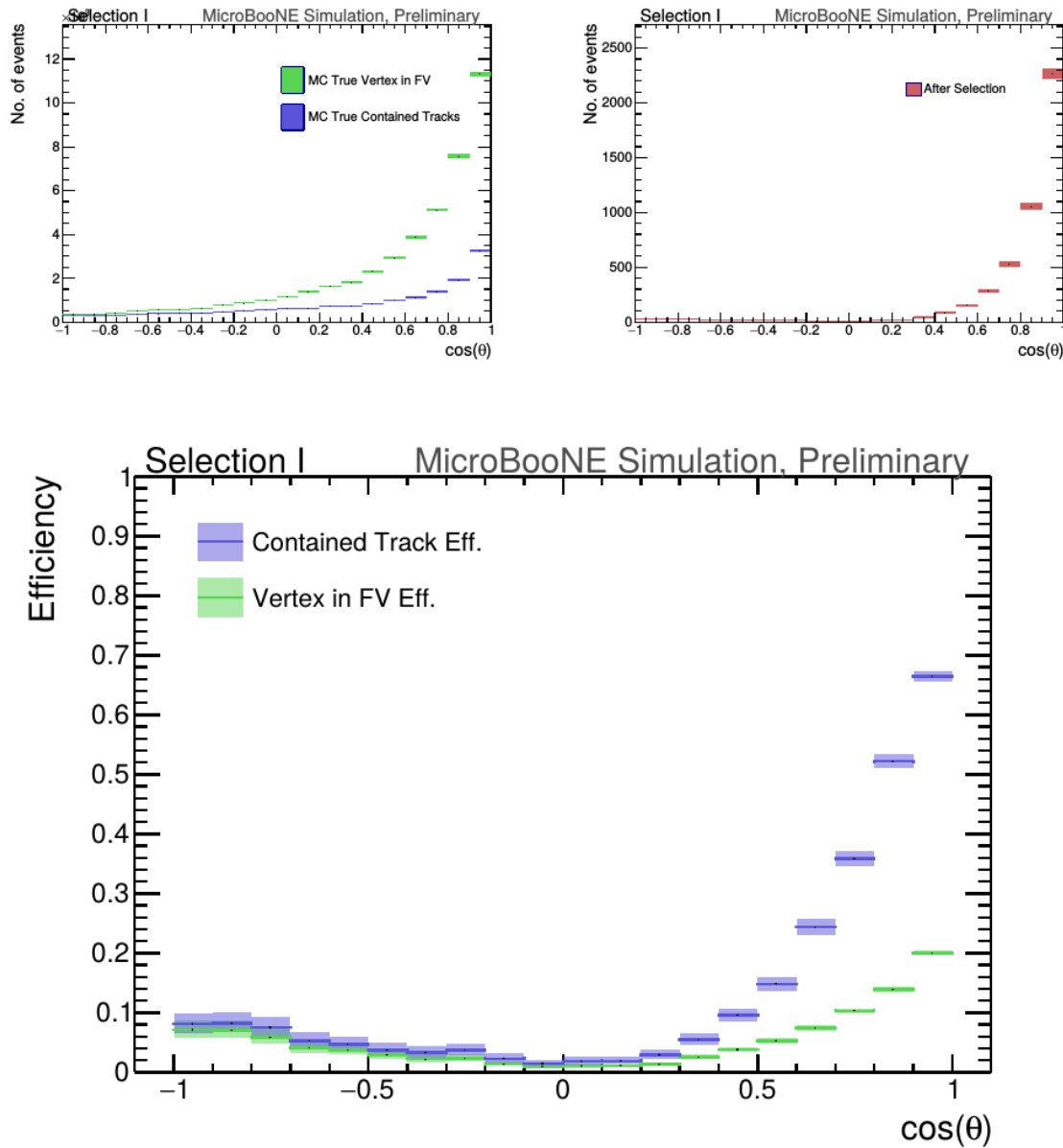


Figure 5.7: MC $\cos(\theta)$ distributions of the muon originating from a ν_μ CC interaction. Upper left is the $\cos(\theta)$ distributions of events with a vertex within the FV (green) and the events with a fully contained track (blue) before the selection. The upper right side is the $\cos(\theta)$ distribution after the selection (red). The lower plot is the selection efficiencies.

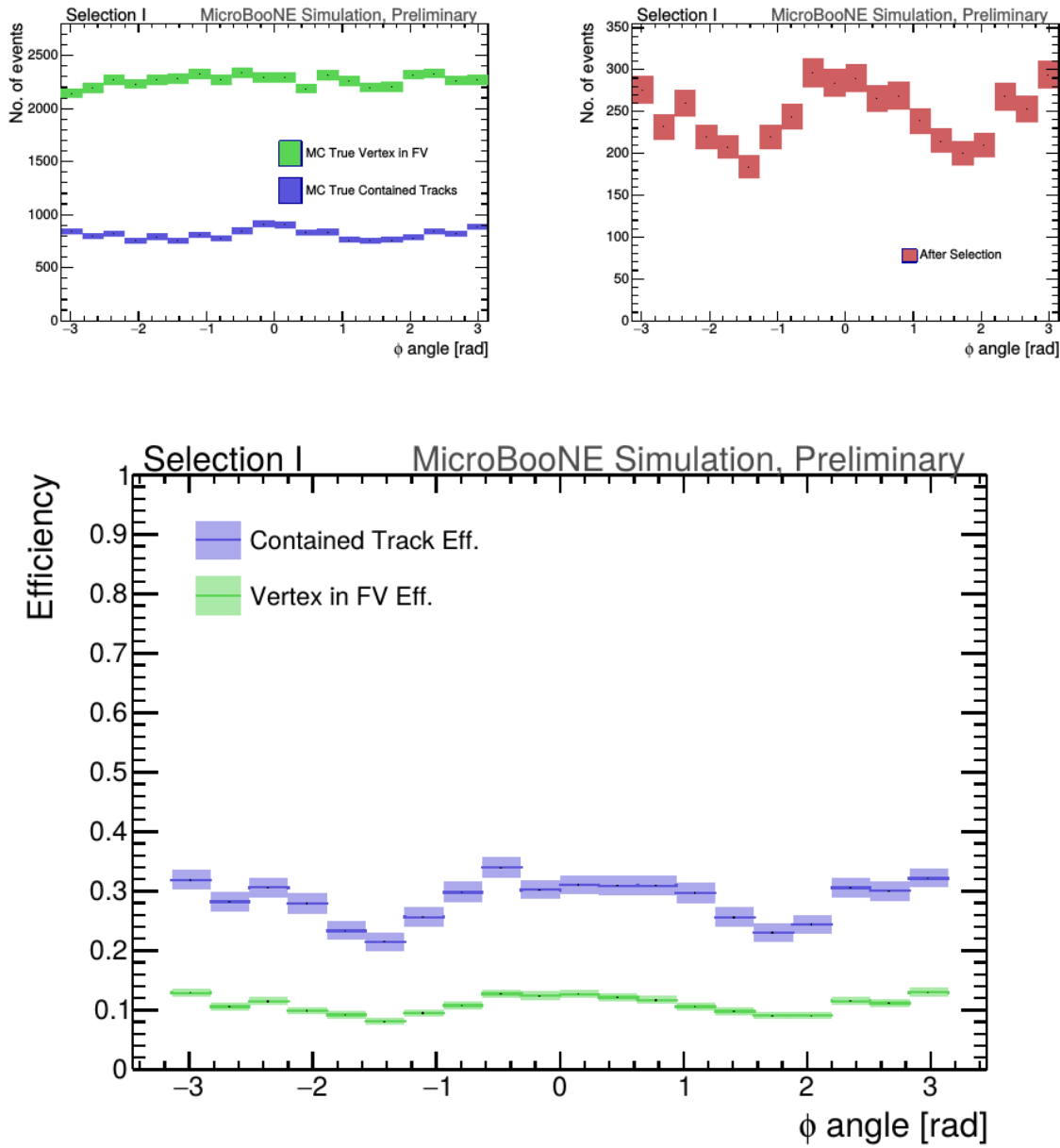


Figure 5.8: MC ϕ distributions of the muon originating from a ν_μ CC interaction. Upper left is the ϕ distributions of events with a vertex within the FV (green) and the events with a fully contained track (blue) before the selection. The upper right side is the ϕ distribution after the selection (red). The lower plot is the selection efficiencies.

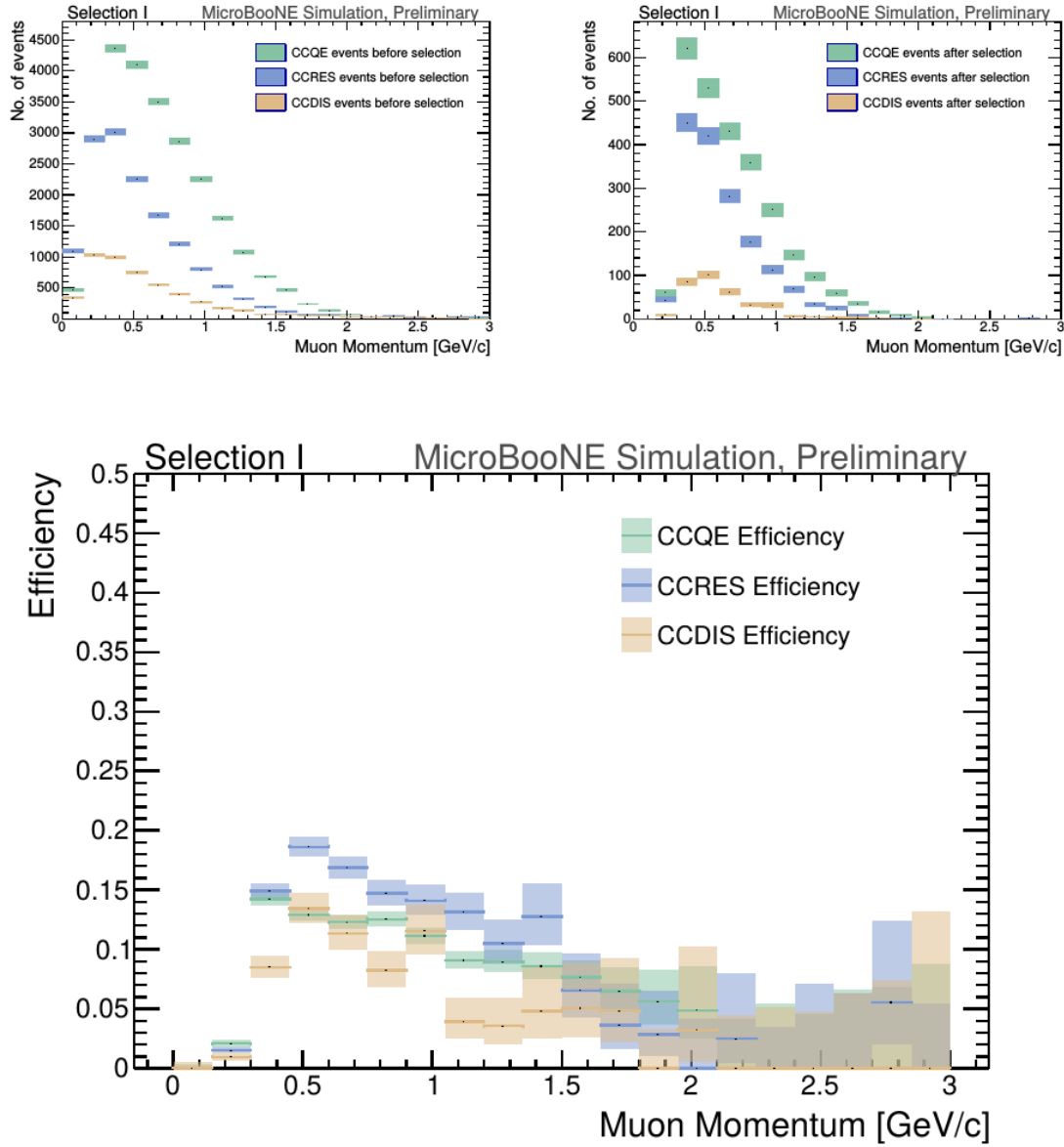


Figure 5.9: MC momentum distributions of the muon originating from a ν_μ CC interaction. Upper left is the momentum distributions of events with a vertex within the FV split up into CCQE (red), CCRES (yellow), and CCDIS (green) before selection. The upper right side is the momentum distribution after the selection with the same color schemes. The lower plot is the selection efficiencies for all three interaction types. The definition of QE, RES, and DIS is based on GENIE.

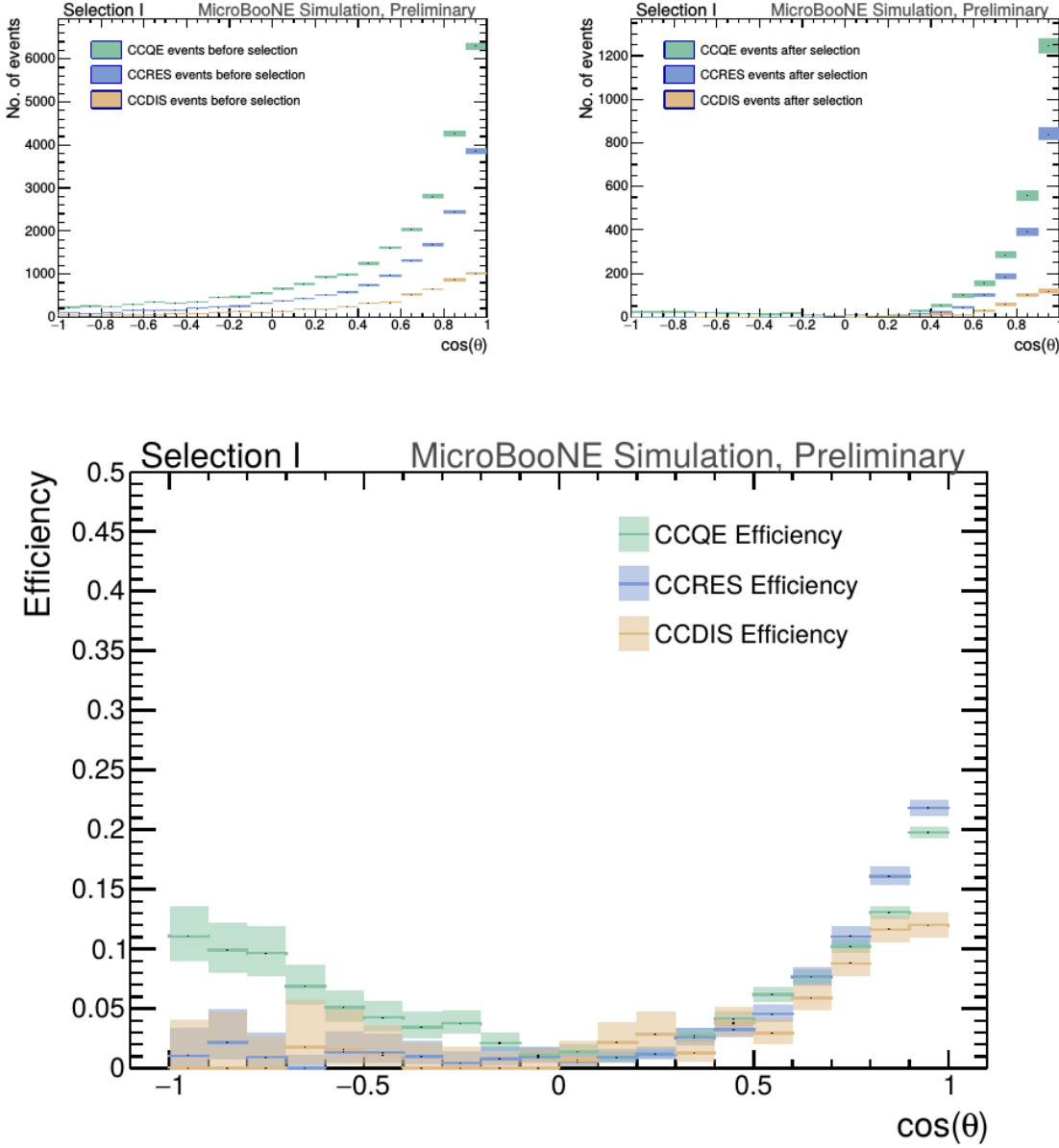


Figure 5.10: MC $\cos(\theta)$ distributions of the muon originating from a ν_μ CC interaction. Upper left is the $\cos(\theta)$ distributions of events with a vertex within the FV split up into CCQE (red), CCRES (yellow), and CCDIS (green) before selection. The upper right side is the $\cos(\theta)$ distribution after the selection with the same color schemes. The lower plot is the selection efficiencies for all three interaction types. The definition of QE, RES, and DIS is based on GENIE.

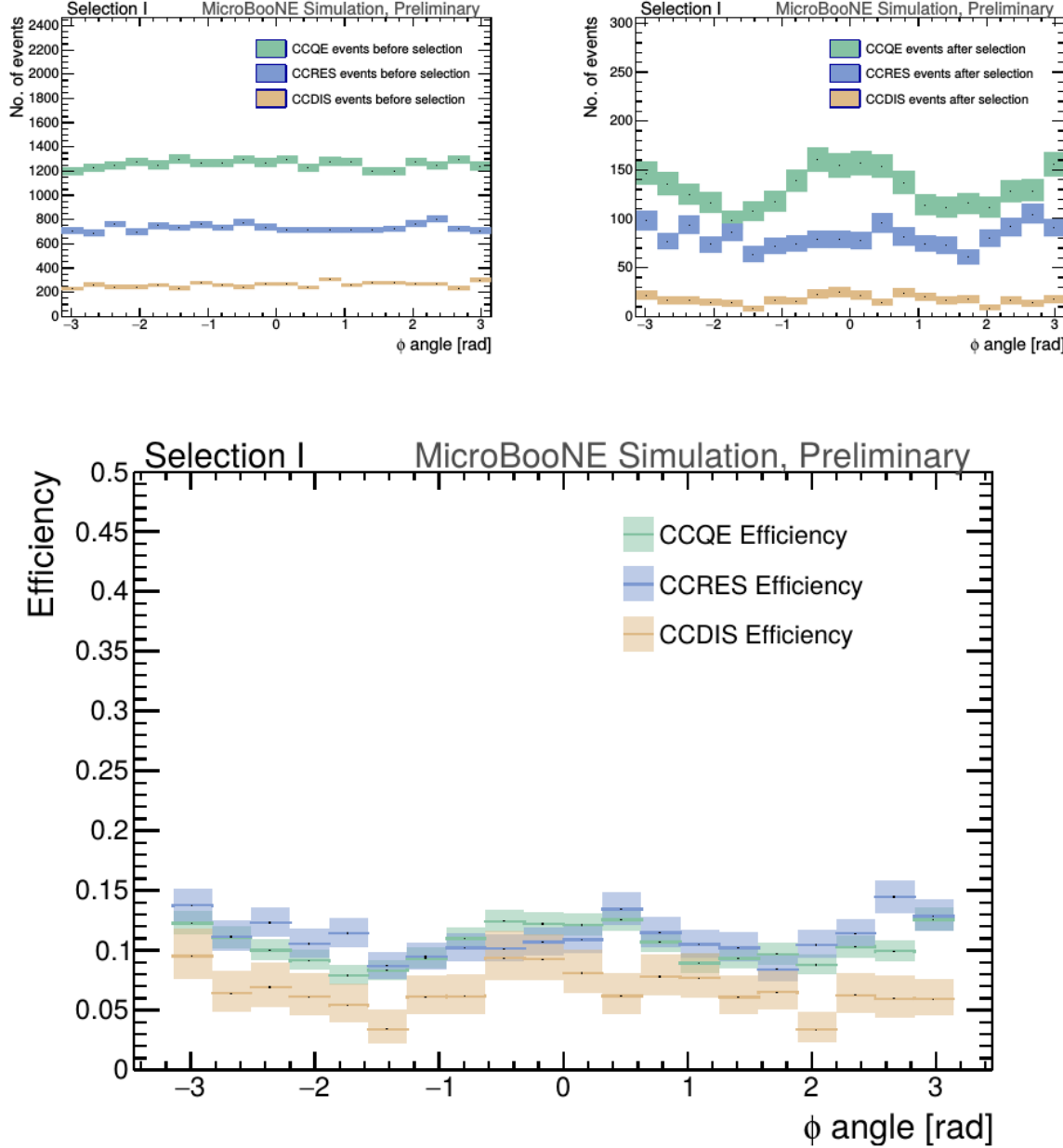


Figure 5.11: MC ϕ distributions of the muon originating from a ν_μ CC interaction. Upper left is the ϕ distributions of events with a vertex within the FV split up into CCQE (red), CCRES (yellow), and CCDIS (green) before selection. The upper right side is the ϕ distribution after the selection with the same color schemes. The lower plot is the selection efficiencies for all three interaction types. The definition of QE, RES, and DIS is based on GENIE.

1311 Chapter 6

1312 Background on Convolutional Neural Networks

1314 Convolutional neural networks (CNNs) have been one of the most influential innovations in the field of computer vision. Neural networks became popular in 2012 1315 when Alex Krizhevsky used them to win that year's ImageNet competition [?] by 1316 dropping the error from 26% to 15%. Since then, many companies are using deep 1317 learning including Facebook's tagging algorithms, Google for their photo search and 1318 Amazon for product recommendations. For the purpose of this thesis CNNs were 1319 used for image classification, specifically, images of varying particles created using 1320 LArTPC data.

1322 6.1 Image Classification

1323 Image classification is the process of inputting an image into the CNN and receiving a 1324 probability of classes that best describes what is happening in the image. As humans, 1325 image classification is something that is learned at a very young age and is easy to 1326 do without much effort. This is also apparent when hand-scanning LArTPC images. 1327 After learning what a neutrino event looks like in MicroBooNE, it is relatively easy 1328 to recognize simple neutrino events from cosmic ray background as well as highly 1329 ionizing particles like protons from minimum ionizing particles like muons. The very 1330 detailed images LArTPC detectors output are prime candidates for input images into 1331 a CNN. CNNs mimic a human's ability to classify objects by creating an architecture 1332 that can learn differences between all the images it's given as well as figure out the

unique features that make up each object. CNNs are modeled after the visual cortex. Hubel and Wiesel [?] found that there are small regions of neuronal cells in the brain that respond to specific regions of the visual field. They saw that some neurons fired when exposed to vertical edges while others fired when shown horizontal or diagonal edges. They also saw that these neurons were organized in columns. The idea of specific neurons inside of the brain firing to specific characteristics is the basis behind CNNs.

6.2 CNN Structure

When used for image recognition, convolutional neural networks consist of multiple layers that extract different information on small portions of the input image. How many layers is tunable to increase the accuracy. The output of these collections are then tiled so that they overlap to gain a better representation of the original image and allow for translation. The first of these layers is always a convolution layer. To the CNN, an image is an array of pixel values. For a RGB color image with width and height equal to 32x32 the corresponding array is 32x32x3. Filters, also known as neurons, of any size set by the user is then convolved with the receptive field of the image. If the filter is 5x5, the receptive field will be a patch of 5x5 on the input image. The filter is also an array of numbers called weights. The convolution of the filter and image are matrix multiplications of the weights and the pixel values. By stepping the receptive field by 1 unit, for an input image of 32x32x3 and a filter of 5x5x3 you'd get an output array of 28x28x1. This output array is called an activation map or feature map. The use of more filters preserves the spatial dimensions better. The filters can be described as feature identifiers. Examples of features in an image consist of edges, curves, and changes in colors. The first filters in a CNN will primarily be straight line and curve feature identifiers. An example of a curve filter is shown in figure 6.2. When a curve in the same concavity is found in the input image, the corresponding pixel in the output feature map will be activated. Going back to our example of a 32x32 input image and a 5x5 filter, if there were to be a curve in the top left corner of the input image, our output feature map would have a high pixel value in the top left. Therefore, feature maps tell us where a specific feature is located in the original image. Figure ?? shows a visualization of filters found in the first layers of many CNN architectures. These filters in the first layer convolve around the image and activate when the specific feature it is looking for is in the receptive field.

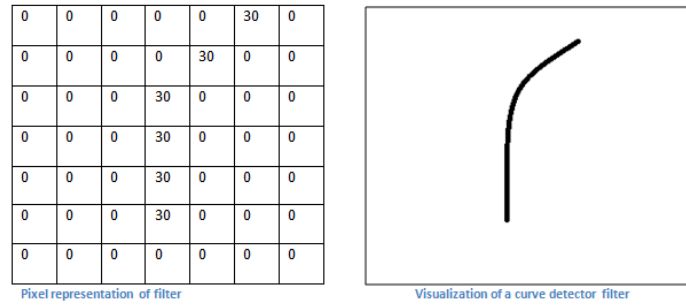


Figure 6.1: Pixel representation and visualization of a curve detector filter. As you can see, in the pixel representation, the weights of this filter are greater along a curve we are trying to find in the input image

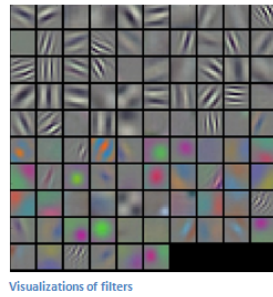


Figure 6.2: Visualization of filters found in first layer of a CNN.

In figure 6.3 you can see how an edge detection filter is used to save only necessary information for recognizing different types of clothes. You can also see by having multiple filters you can get more detail or less detail from an image which can then simplify or complicate the object recognition task. Being able to distinguish between a shirt or a leg garment is as much information you want, having a filter that extracts outline edge or shape information would be all that you need. But if instead you wanted to distinguish between a formal cocktail dress or a summer dress, more information would need to be saved equating to many more filters for one image. Rather than trying to come up with how many filters and what features are important for detection, CNNs do this automatically. CNNs take input parameters, called hyperparameters, for example number of layers, number of filters per layers, number of weights per filter, and uses these to create the output feature maps. The layers build upon each-other, for example if we were creating a CNN for facial recognition the convolutional layers will start learning feature combinations off of the previous layers. The low level features like edges, gradients, and corners of the first layers become high level features like eyes, noses, and hairs. This process is visualized in figure 6.4



Figure 6.3: Applying a feature mask over a set of fashion items to extract necessary information for auto-encoding. Unnecessary information for example color or brand emblems are not saved. This feature map is an edge detection mask that leaves only shape information which helps to distinguish between different types of clothes.

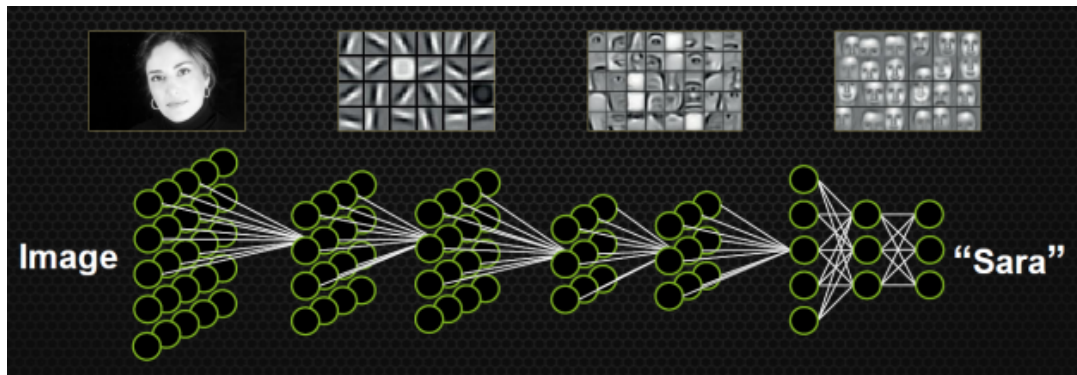


Figure 6.4: Pictorial Representation of Convolutional Neural Networks as well as a visual representation on CNN's complexity of layer feature extraction

1382 There are other layers in a CNN architecture that will not be covered in the scope
 1383 of this thesis but in a general sense, these layers are interspersed between convolution
 1384 layers to preserve dimensionality and control overfitting of the network. The last layer
 1385 is called a fully connected layer and it's job is to output an N dimensional vector where
 1386 N is the number of classes the network has been trained on. Each number in this vector
 1387 represents the probability that the input image is a certain class. Fully connected layers
 1388 use the feature maps of the high level features to compute the products between the
 1389 weights of the previous layer to get the probabilities of each class. These weights are
 1390 then adjusted through the training process using backpropagation.

1391 6.2.1 Backpropagation

1392 A CNN at it's onset has weights that are randomized. The filters themselves don't
1393 know how to pull out identifying information per class. For a neural network to learn,
1394 it must be trained on a training set that is labeled. Backpropagation has four seperate
1395 steps: foward pass, loss function, backward pass and updating weights. In the forward
1396 pass, a training image is passed through the whole network. All of our weights at this
1397 time are randomly initialized so the output for the first image will have no preference
1398 to a specific class. A common loss function is mean squared error (MSE):

$$E_{total} = \sum \frac{1}{2} (actualclass - predictedclass)^2 \quad (6.1)$$

1399 If we assume that the MSE is the loss of our CNN, the goal would be that our
1400 predicted label (output of CNN) is the same as our training label. To do this, we need
1401 to minimize the loss function. To do this, it is necessary to find out which weights most
1402 directly affect the loss of the network i.e $\frac{dL}{dW}$ where L is our loss function and W are
1403 the weights of a specific layer. The next step is the backward pass which determines
1404 which weights contribute the most to the loss and finds ways to adjust these weights
1405 so that the loss decreases. After the derivative is computed, the last step updates the
1406 weights in the opposite direction of the gradient.

$$w = w_i - \eta \frac{dL}{dW} \quad (6.2)$$

$$w = \text{Weight} \quad (6.3)$$

$$w_i = \text{Initial Weight} \quad (6.4)$$

$$\eta = \text{Learning Rate} \quad (6.5)$$

1407 The learning rate is a parameter given to the CNN and it describes the steps the
1408 network takes to update the weights. Higher learning rate equals large steps and a
1409 lower training time, but a learning rate that is too large can mean the CNN never
1410 converges.

1411 Going through backpropagation consists of one training iteration. Once the net-
1412 work completes a specific number of iterations, another parameter given, and runs
1413 over all training images that are split up into batches, the process is considered com-
1414 plete. User input parameters, called hyperparameters, help the network converge to

1415 optimal weights for each layer. Batch size, learning rate, and training iteration are just
1416 some of the user input hyperparameters that help. Lastly, to check if the network has
1417 learned, a different set of labeled images are fed to the CNN iteratively through the
1418 training process to see how well it's learning. This process is especially important to
1419 make sure the network architecture isn't being affected by overfitting (memorizing
1420 training input rather than learning).

1421 6.3 Choosing Hyperparameters

1422 Convolutional neural networks are a relatively new tools in computer vision. Choosing
1423 hyperparameters for your specific dataset is a non-trivial task. Hyperparameters can
1424 range from the amount of layers and filters per layer in an CNN architecture to the
1425 stride the receptive field of a filter takes, not to mention training hyperparameters
1426 such as learning rate and batch size described above. They're ways to optimize these
1427 hyperparameters via hyperparameter optimization using Bayesian Optimization [?]
1428 but as you can imagine, optimizing an CNN architecture from scratch can be very
1429 computationally intensive. For the purpose of this thesis, two well known CNN
1430 architectures were used, AlexNet [?], which won the ImageNet Large-Scale Visual
1431 Recognition Challenge (ILSVRC) in 2012 and therefore bringing awareness of CNNs,
1432 and GoogleNet [?], which won the ILSVRC in 2014, giving rise to deep networks. Both
1433 AlexNet and GoogleNet architectures were used to train on LArTPC images and their
1434 low level filter weights. Higher level filter weights were randomly initialized before
1435 training so the network can learn high level features of LArTPC image classes. The
1436 AlexNet architecture is shown in figure 6.5 and the GoogleNet architecture is shown
1437 in figure 6.6

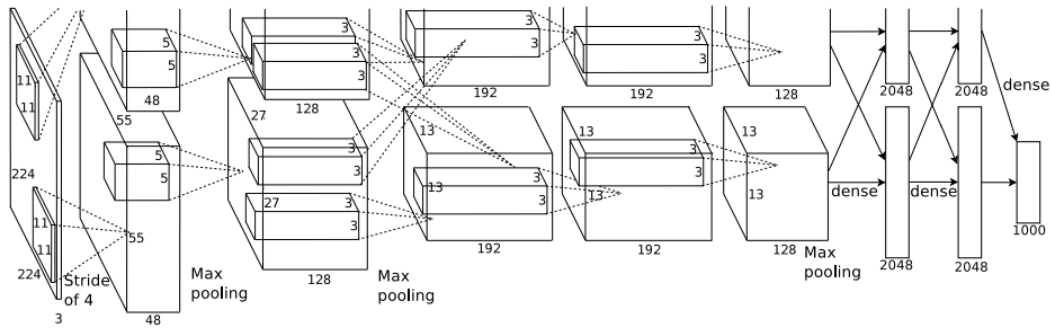


Figure 6.5: Pictoral representation of the AlexNet model. The AlexNet model consists of 5 convolution layers and 3 fully connected layers.

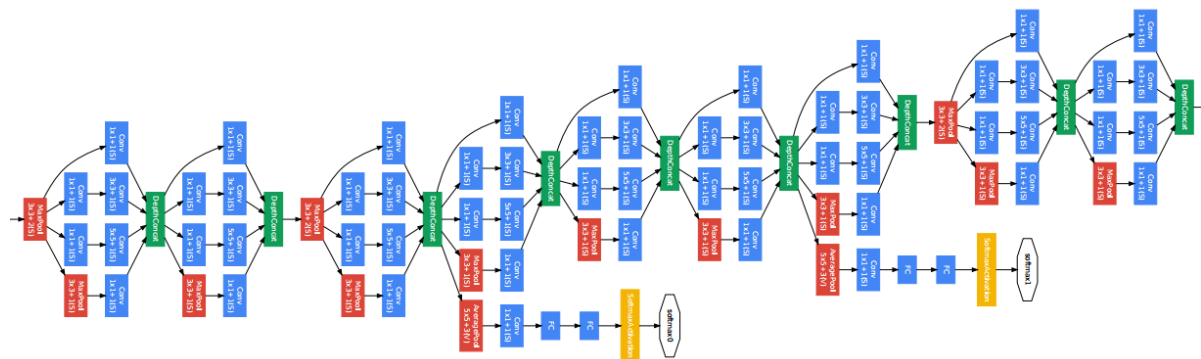


Figure 6.6: Pictoral representation of the GoogleNet model. The GoogleNet model consists of 22 layers. The model implements 9 Inception modules which performs covolution and pooling in parallel and strays away from the basis that CNN layers need to be stacked up sequentially. The GoogleNet model also doesn't use fully connected layers, instead it uses average pooling which greatly reduces the amount of parameters. GoogleNet has 12x fewer parameters than AlexNet.

¹⁴³⁸ Chapter 7

¹⁴³⁹ **Training process of Convolutional 1440 Neural Networks**

¹⁴⁴¹ Three Convolutional Neural Networks (CNNs) were trained throughout this analysis.
¹⁴⁴² There are differences to each CNN and will be described fully in the next sections but
¹⁴⁴³ the main difference are the amount of particle images used for training and validation.
¹⁴⁴⁴ CNN1075 used 1,075 muons and 1,075 pions for training and the same amount of
¹⁴⁴⁵ each particle for validation. CNN10000 used 10,000 muons and 10,000 pions split in
¹⁴⁴⁶ half for testing and training. Lastly CNN100000 had muons, pions, protons, electrons,
¹⁴⁴⁷ and gammas in it's training and validation set. Each particle had 20,000 images and
¹⁴⁴⁸ training and validation was split 90% training, 10% validation. This chapter will also
¹⁴⁴⁹ describe the different hardware frameworks used for training beginning on a CPU
¹⁴⁵⁰ and ending on a GPU cluster.

¹⁴⁵¹ **7.1 Hardware Configurations for Convolutional Neural 1452 Network Training**

¹⁴⁵³ The first training iteration, CNN1075, was a proof of concept. This CNN was trained
¹⁴⁵⁴ on my local machine for \sim 4-5 weeks. The batch size had to be very small as well as the
¹⁴⁵⁵ image size due to the lack of computation resources. The second iteration of training,
¹⁴⁵⁶ CNN10000, was trained on a Fermilab stationed Syracuse University machine. This
¹⁴⁵⁷ machine had 6 TB of disk space, 6 cores at 2.1 GHz and 32 GB of RAM. The use of
¹⁴⁵⁸ this machine allowed me to increase the training sample as well as the batch size and
¹⁴⁵⁹ hence further increase the accuracy of the neural network. Lastly, the CNN100000 was

¹⁴⁶⁰ trained using two GTX 1080 Ti GPUs with 11GB of memory on a node on the Syracuse
¹⁴⁶¹ University GPU cluster, SUrge, that has 8 cores and 16GB of memory. This increase in
¹⁴⁶² memory as well as the capability to use 2 GPUs drastically cut down on training time
¹⁴⁶³ from \sim 4-5 weeks to \sim 8 hours. SUrge also allowed for hyperparameter optimization
¹⁴⁶⁴ by being able to run multiple training iterations over the two GPUs. Lastly, SUrge
¹⁴⁶⁵ allowed for training over higher resolution images and a larger particle class of 5
¹⁴⁶⁶ particles vs 2 particles.

¹⁴⁶⁷ **7.2 Creating images using LArTPC data for
¹⁴⁶⁸ training/validation of CNNs**

¹⁴⁶⁹ The μ/π image dataset used to train and validate CNN1075 was created using single
¹⁴⁷⁰ generated isotropic muons and pions from 0-2 GeV energy range. 2,150 muons and
¹⁴⁷¹ 2,150 pions were used for training and testing split 50%. The images were created
¹⁴⁷² using LArSoft, a liquid argon software, and were based on wire number and time
¹⁴⁷³ tick in the collection plane. Uboonecode reconstruction version v05_08_00 was used.
¹⁴⁷⁴ The raw ADC value after noise filtering was the wire signal. Each collection plane
¹⁴⁷⁵ greyscale image was 3456x1600x1 where 6 time ticks were pooled into 1 bin.

¹⁴⁷⁶ After the image was created, the region of interest (ROI) in the image was found by
¹⁴⁷⁷ using Open CV, a image processing open source software package, to scan the image
¹⁴⁷⁸ starting from the edges and stopping once a bright pixel is encountered. At this step,
¹⁴⁷⁹ the ROI can be larger or smaller than the necessary size of a training image and the XY
¹⁴⁸⁰ ratio of the image is not kept. This ROI is then resized to an image of 224x224x1.

¹⁴⁸¹ The greyscale color standard is 8bit therefore the ADC value of wire and time tick
¹⁴⁸² was also downsampled due to the 12bit ADC value MicroBooNE has. To do this,
¹⁴⁸³ the highest ADC pixel in the image was found and then this was divided by the rest
¹⁴⁸⁴ placing all pixel values between 0-1. From there, all pixel values are then multiplied
¹⁴⁸⁵ by 255.

¹⁴⁸⁶ The μ/π image dataset used to train and validate the CNN10000 was also created
¹⁴⁸⁷ using single generated isotropic muons and pions from 0-2 GeV energy range. 10,000
¹⁴⁸⁸ muons and 10,000 pions were used for training and testing split 50%. Uboonecode
¹⁴⁸⁹ v06_23_00 was used instead of v05_08_00. Each collection plane greyscale image was
¹⁴⁹⁰ 3456x1280x1 where 5 time ticks were pooled into 1 bin which is different than the

1491 previous dataset and was implemented due to the fact that the time ticks of an event
1492 went from 9400 to 6400 with the change of uboonecode version. Issues that arose in
1493 CNN1075 that were fixed in CNN10000 include zero-padding images in X and Y that
1494 are smaller than 224X224 to eliminate over-zooming effect and fixing a bug that shifted
1495 pixels separated by a dead-wire region.

1496 The $\mu/\pi/p/e/\gamma$ image dataset used to train and validate the CNN100000 were
1497 created using single generated isotropic particles with energy range from 0-2 GeV.
1498 20,000 of each particle were used for training and were split 90/10 between training
1499 and testing sets. Uboonecode v06_23_00 was used for these images. The collection
1500 plane greyscale iamge had the same dimensions as CNN10000, 3456x1280x1 and the
1501 ROI algorithm was the same except for resizing these images to 576x576.

1502 A major change other than the higher resolution images was the treatment of the
1503 ADC values. In the first two image making schemes, the highest pixel value was found
1504 per image and the image was then normalized by that. The issue arising from this
1505 ADC normalization wasn't inherent in μ/π training due to the fact that both particles
1506 are minimum ionizing particles in liquid argon, however, when dealing with a larger
1507 particle class, it was necessary to try and make sure energy deposition by each particle
1508 was preserved. The energy deposition in a particle image corresponds to the ADC
1509 value or pixel brightness. To preserve energy deposition, the ADC float value was
1510 passed straight to the image rather than doing any image normalization. This then
1511 makes sure that minimum ionizing particles like muons and pions appear dimmer
1512 than highly ionizing particles like protons.

1513 Images were also made from BNB+Cosmic events that passed the cc-inclusive
1514 selection 1 filter right before the 75 cm track length cut and were classified using
1515 the CNN10000. The dataset used to create these images is the same one used in
1516 [?], *prodgenie_bnb_nu_cosmic_uboone_mcc7_reco2*. These images were created using
1517 information from the track candidate that passed the filter. Only wire number and
1518 time ticks associated to the track candidate were drawn on the image to mimic a single
1519 particle generated image.

1520 These images were then classified using CNN10000. Two approaches were taken
1521 in making these images. The first was using the image normalization above where
1522 the maximum pixel in each image is used as a normalization constant to get all pixels
1523 between 0-1 then multiply all pixels by 255. As described above, this is the incorrect

1524 way to normalize. The second way the images were created was by passing the ADC
1525 float to the image. The results of CNN10000 performance are shown in section [7.1](#).

1526 Lastly, multiple BNB+Cosmic images per event were made for CNN100000 by
1527 reducing many of selection I cuts to try and let the CNN do particle as well as event
1528 identification. This image making scheme used for CNN100000 will be described in
1529 more detail in later sections.

1530 7.3 Convolutional Neural Network Training

1531 7.3.1 Training CNN1075

1532 The results of CNN1075 are described in this section. The accuracy is how well
1533 CNN1075 is doing by epoch and was 74.5%. The loss is gradient descent or mini-
1534 mization of the error of the weights and biases used in each neuron of each layer of
1535 CNN1075 and was 58% with a trend sloping downwards on the loss curve as well as a
1536 trend sloping upward in the accuracy curve. The accuracy and loss of CNN1075 are
1537 shown in figure [7.1](#). Due to the depth of the neural network framework, it was neces-
1538 sary to train with a larger dataset and for more epochs, however, the downward slope
1539 of the loss curve is an indication that once trained for longer with a higher training
1540 sample, neural networks can be used for μ/π separation. The hyperparameters used
1541 to train CNN1075 are detailed below:

- 1542 • *train_batch_size*: 50 1547 • *lr_policy*: "step" 1552 • *momentum*: 0.9
- 1543 • *test_batch_size*: 50 1548 • *gamma*: 0.1 1553 • *weight_decay*: 0.0005
- 1544 • *test_iter*: 50 1549 • *stepsize*: 200 1554 • *snapshot*: 100
- 1545 • *test_interval*: 50 1550 • *display*: 50
- 1546 • *base_lr*: 0.01 1551 • *max_iter*: 5000

1555 The confusion matrices shown in figure [7.2](#) show the accuracy for both the training
1556 and testing datasets. The fact that these two have similar accuracies is important
1557 because if the training dataset had a much higher accuracy, that indicates an over-
1558 training of the training sample which means the neural network didn't learn features
1559 to separate muons from pions, it just memorized what was in the training dataset.

Loss/Accuracy of CNN trained on 2150 images

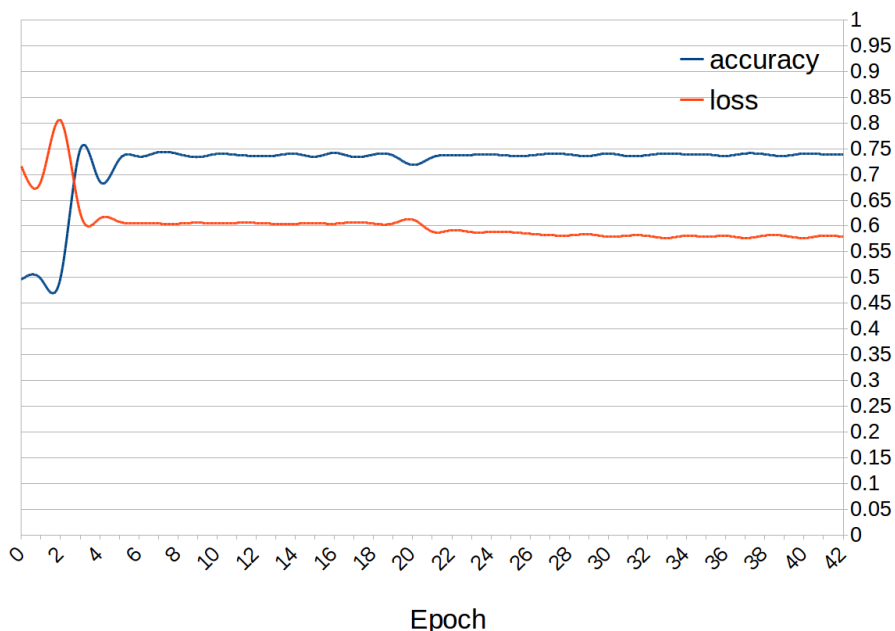
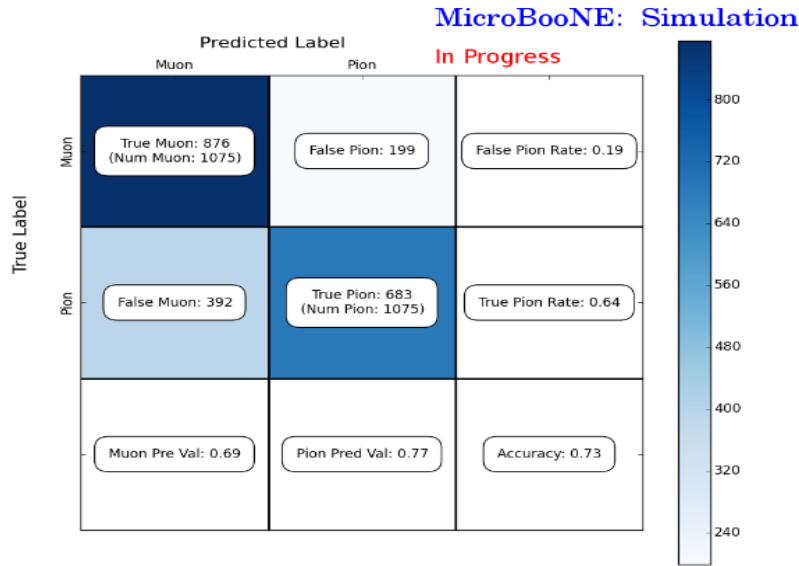
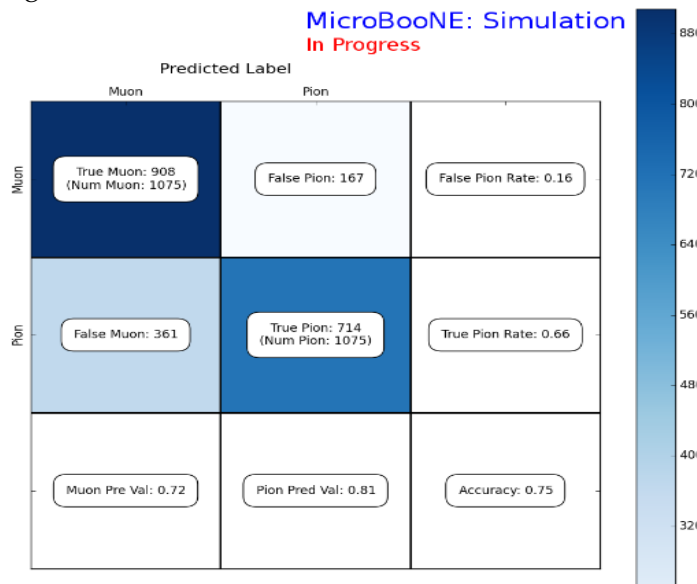


Figure 7.1: Accuracy vs. Loss of AlexNet 2-output μ/π sample consisting of 2,150 images each.



(a) Confusion Matrix showing Accuracy of CNN1075 using training MC data



(b) Confusion Matrix showing Accuracy of CNN1075 using testing MC data

Figure 7.2: Description of confusion matrix variables: False pion rate = $false\pi / total\pi$ True pion rate = $true\pi / total\pi$ Accuracy = $(true\pi rate + true\mu rate) / 2$ Pion prediction value = $true\pi / (true\pi + false\pi)$ Muon prediction value = $true\mu / (true\mu + false\mu)$

1560 Also note that the neural network does a better job of identifying muons than pions.
1561 This can be attributed to the more complex event scenes pions tend to leave in the
1562 detector due to pion interacting more in LAr than muons do. The CNN may do better
1563 at identifying pions with a larger training sample.

1564 **7.3.2 Training CNN10000**

1565 The hyperparameters used for CNN10000 are shown below. The batch size for the
1566 training and testing as well as the test_iter were chosen to encompass the whole
1567 training/testing image set when doing accuracy/loss calculations. To do this, multi-
1568 plying the test_iter by the test batch size gives you the amount of images used when
1569 calculating accuracy/loss curves.

- 1570 • *train_batch_size*: 100₁₅₇₅ • *lr_policy*: "step"₁₅₈₀ • *momentum*: 0.99
- 1571 • *test_batch_size*: 100₁₅₇₆ • *gamma*: 0.1₁₅₈₁ • *weight_decay*: 0.0005
- 1572 • *test_iter*: 100₁₅₇₇ • *stepsize*: 1000₁₅₈₂ • *snapshot*: 100
- 1573 • *test_interval*: 100₁₅₇₈ • *display*: 100
- 1574 • *base_lr*: 0.001₁₅₇₉ • *max_iter*: 10000

1583 The same architecture that was used to train CNN1075 was employed on CNN10000,
1584 AlexNet. Caffe [?] was the software package used for both CNNs. The differences
1585 include batch size and test_iter and momentum to account for the larger dataset. Fig-
1586 ure 7.3 shows the loss and accuracy of CNN10000. There is around a 10% increase in
1587 accuracy from CNN1075 to CNN10000, 85%, and around a 20% decrease in loss, 36%.

1588 Figure 7.4 show a breakdown of μ/π separation for CNN10000. It also shows
1589 the network is not being over-trained due to the Accuracy of both the training and
1590 testing datasets being within .01% of each-other. Figure 7.5 shows how well the neural
1591 network is doing at μ/π separation with respect to muon probability. The red bins
1592 corresponds to true pions and the blue bins correspond to true muons. There is
1593 still pion contamination in the high muon probability bins but by choosing a muon
1594 probability of $\geq 80\%$ we can reduce this. The CNNs increase in total accuracy can be
1595 attributed to an increase in accurately classifying pions as pions as seen in both the
1596 confusion matrix in figure 7.4 and the large number of events in the zero bin of the
1597 muon probability plot seen in figure 7.5 that corresponds to high probability pions.

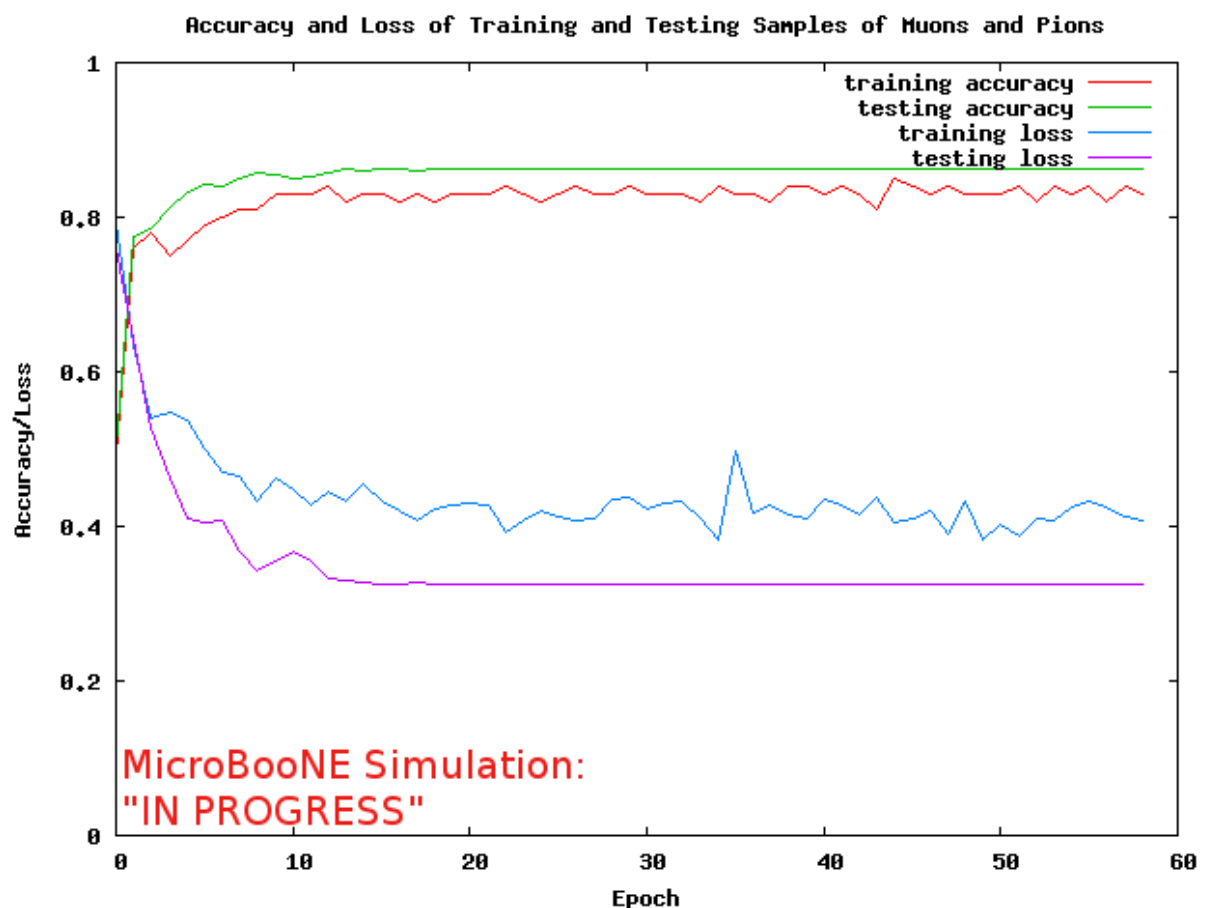
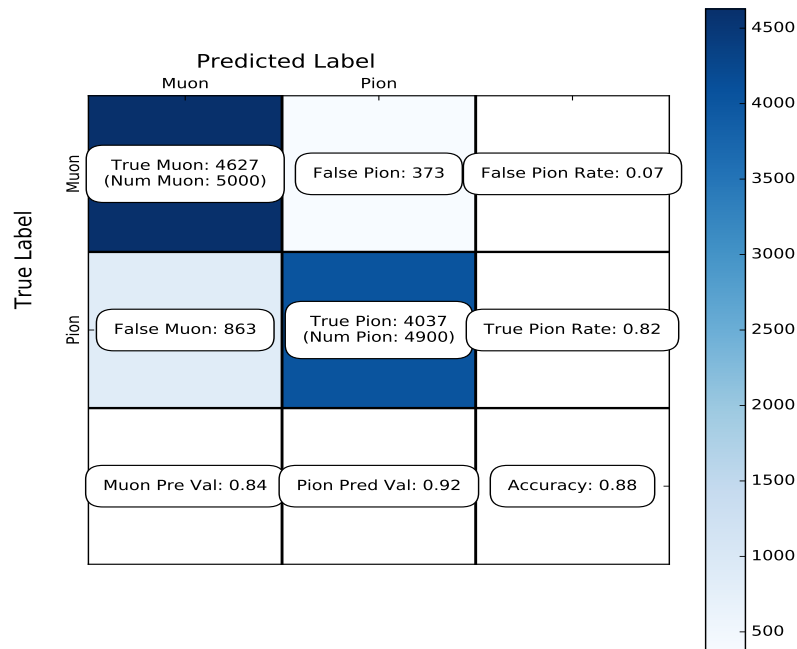
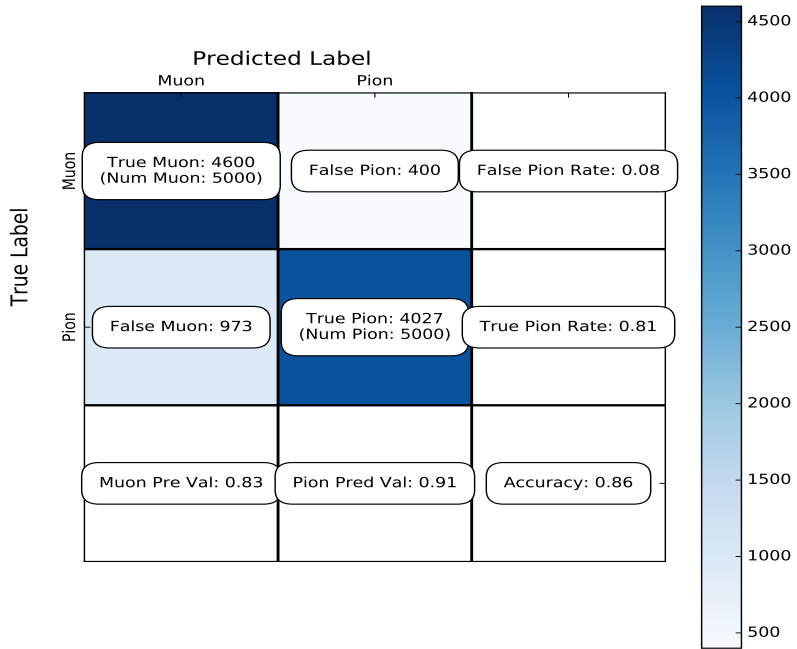


Figure 7.3: Accuracy vs. Loss of AlexNet 2-output μ/π sample consisting of 10,000 images each.



(a) Confusion Matrix showing Accuracy of CNN10000 using training MC data



(b) Confusion Matrix showing Accuracy of CNN10000 using testing MC data

Figure 7.4: Description of confusion matrix variables: False pion rate = $false\pi / total\pi$; True pion rate = $true\pi / total\pi$; Accuracy = $(true\pi rate + true\mu rate) / 2$; Pion prediction value = $true\pi / (true\pi + false\pi)$; Muon prediction value = $true\mu / (true\mu + false\mu)$

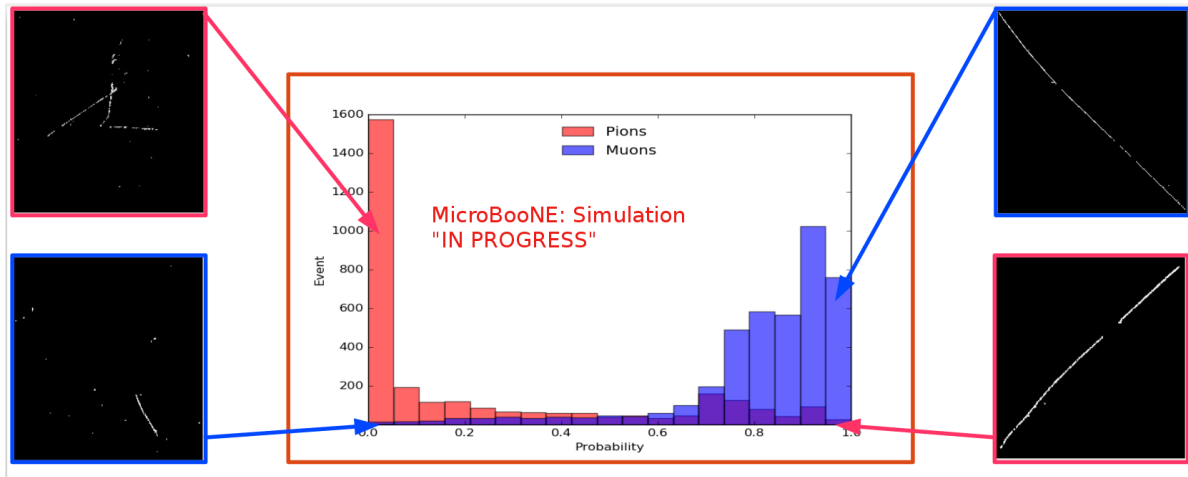


Figure 7.5: Probability plot of muons and pions from testing set. Images surrounding histogram are a random event from lowest bin and highest bin for each particle.

1598 7.3.3 Training CNN100000

1599 CNN100000 used the GoogleNet architecture rather than the AlexNet architecture
 1600 used in the two previous trained CNNs. This is the first time the neural network was
 1601 trained on a larger particle class, $\mu/\pi/p/\gamma/e$, and on higher resolution images. This
 1602 CNN also employed GPUs during the training process. The hyperparameters are
 1603 shown below:

- 1604 • *train_batch_size*: 18 1609 • *lr_policy*: "step" 1614 • *max_iter*: 10000
- 1605 • *test_batch_size*: 2 1610 • *gamma*: 0.96 1615 • *momentum*: 0.99
- 1606 • *test_iter*: 2000 1611 • *stepsize*: 10000 1616 • *weight_decay*: 0.0002
- 1607 • *test_interval*: 2000 1612 • *average_loss*: 40 1617 • *snapshot*: 50000
- 1608 • *base_lr*: 0.001 1613 • *display*: 40

1618 The accuracy and loss for CNN100000 are shown in figures 7.6 and 7.7. The jumps
 1619 shown in both figures are when the training was stopped to fine-tune the weight decay
 1620 and the learning rate. The accuracy leveled off at $\sim 80\%$ and the loss was at ~ 0.48 .

1621 Figure 7.8 shows the confusion matrix of CNN100000. The proton identification of
 1622 the neural network is at 85% and the highest out of all five particles. One thing to note
 1623 is clear separation between particles that leave track like objects in the MicroBooNE
 1624 detector, $\mu/\pi/p$, versus particles that leave shower like objects in MicroBooNE, e/γ .

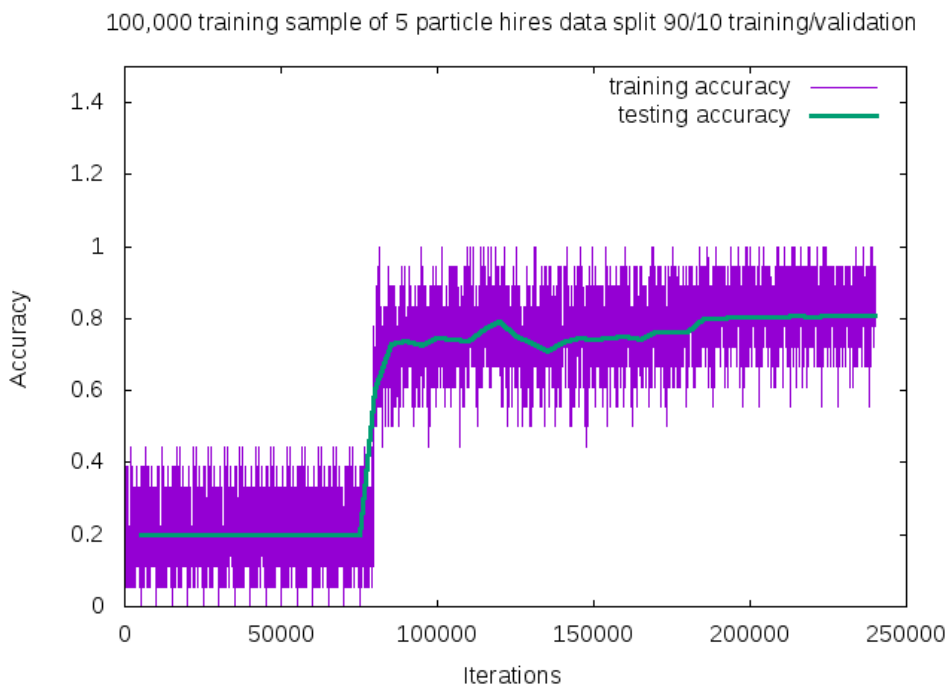


Figure 7.6: Training and testing accuracy of CNN trained on 100,000 images of $\mu/\pi/p/\gamma/e$ with 20,000 images of each particle. Each image was a size of 576x576 and the images per particle were split 90% use for training and 10% used for testing the network

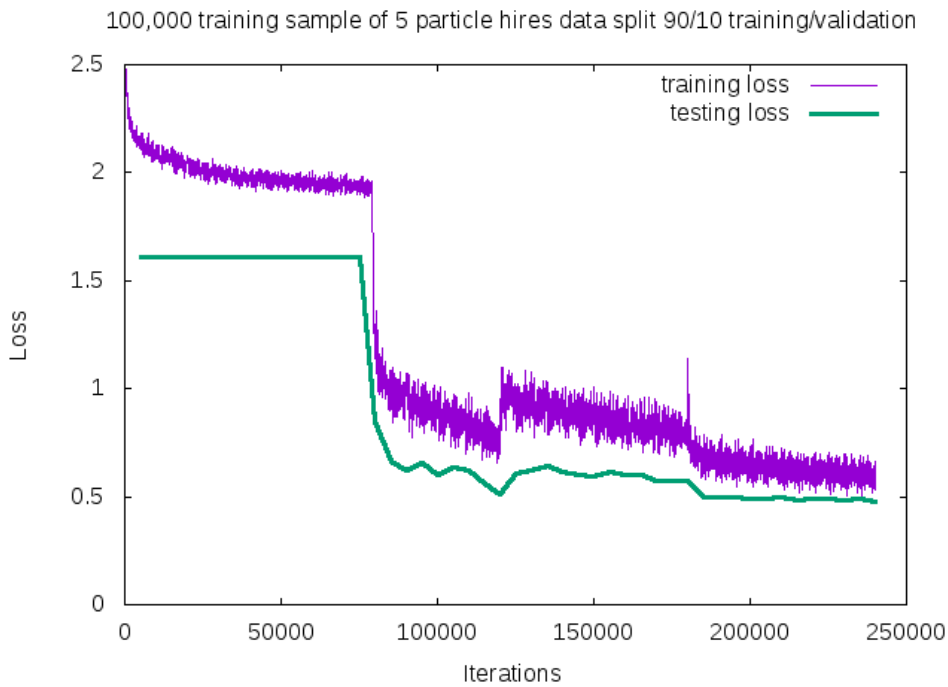


Figure 7.7: Training and testing loss of CNN trained on 100,000 images of $\mu/\pi/p/\gamma/e$

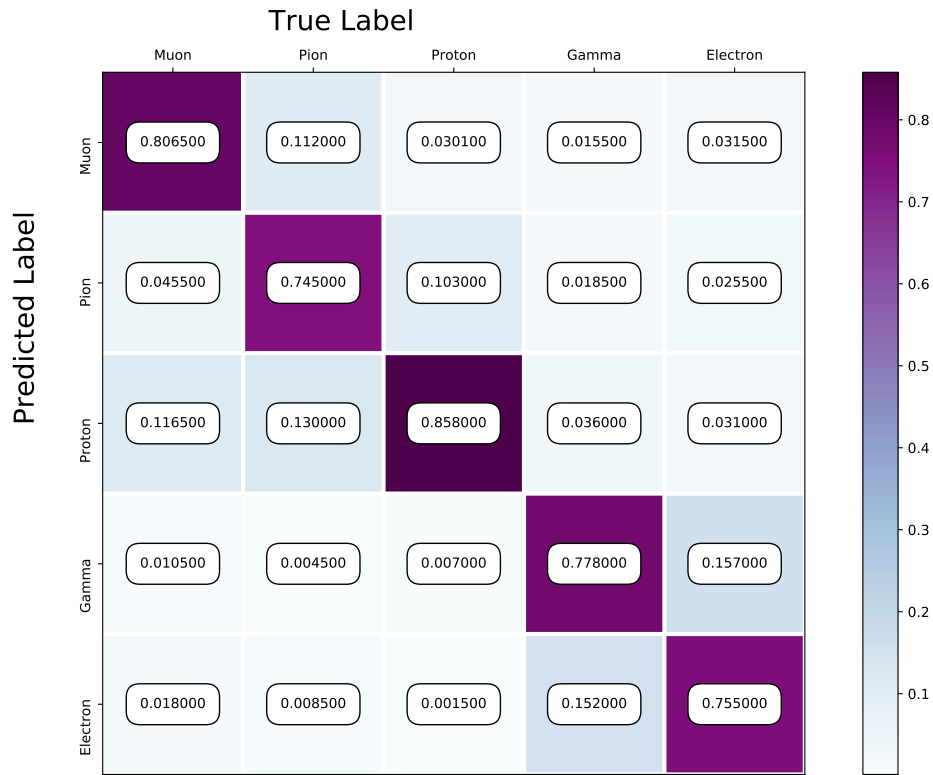


Figure 7.8: Confusion Matrix of all five particles

Another visualization of how the neural network is learning is shown in 7.9. t-SNEs [?] is a technique used for dimensionality reduction developed for use in visualizing high-dimensional datasets. Each datapoint is given a location in a two or three-dimensional map by using stochastic neighbor embedding to convert high-dimensional euclidean distances between datapoints into conditional probabilities that represent the similarities between these datapoints. For datapoints close together on the map, their conditional probabilities are high, for datapoints with a wide separation between them, their conditional probabilities are very small. Figure 7.9 is a t-SNE of the final training iteration of a subset of the training sample used in CNN100000. You can see a clear separation between track like objects and shower like objects. You can also see that electrons and gammas are not as separated as muons, pions, and protons. For the purpose of this thesis, this isn't an issue but later iterations of training could include more images for the gamma and electron classes to help the CNN further separate these classes.

Figure 7.10 shows the probability of each particle class and the highest probability misidentification for each class. For muons, the largest misidentification is from

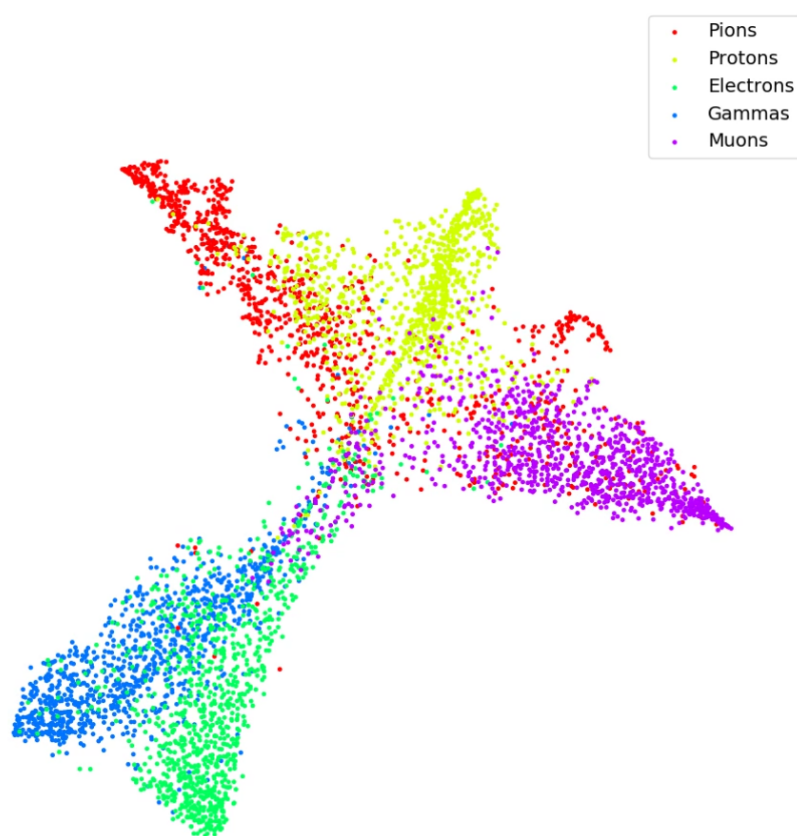


Figure 7.9: t-SNE of CNN

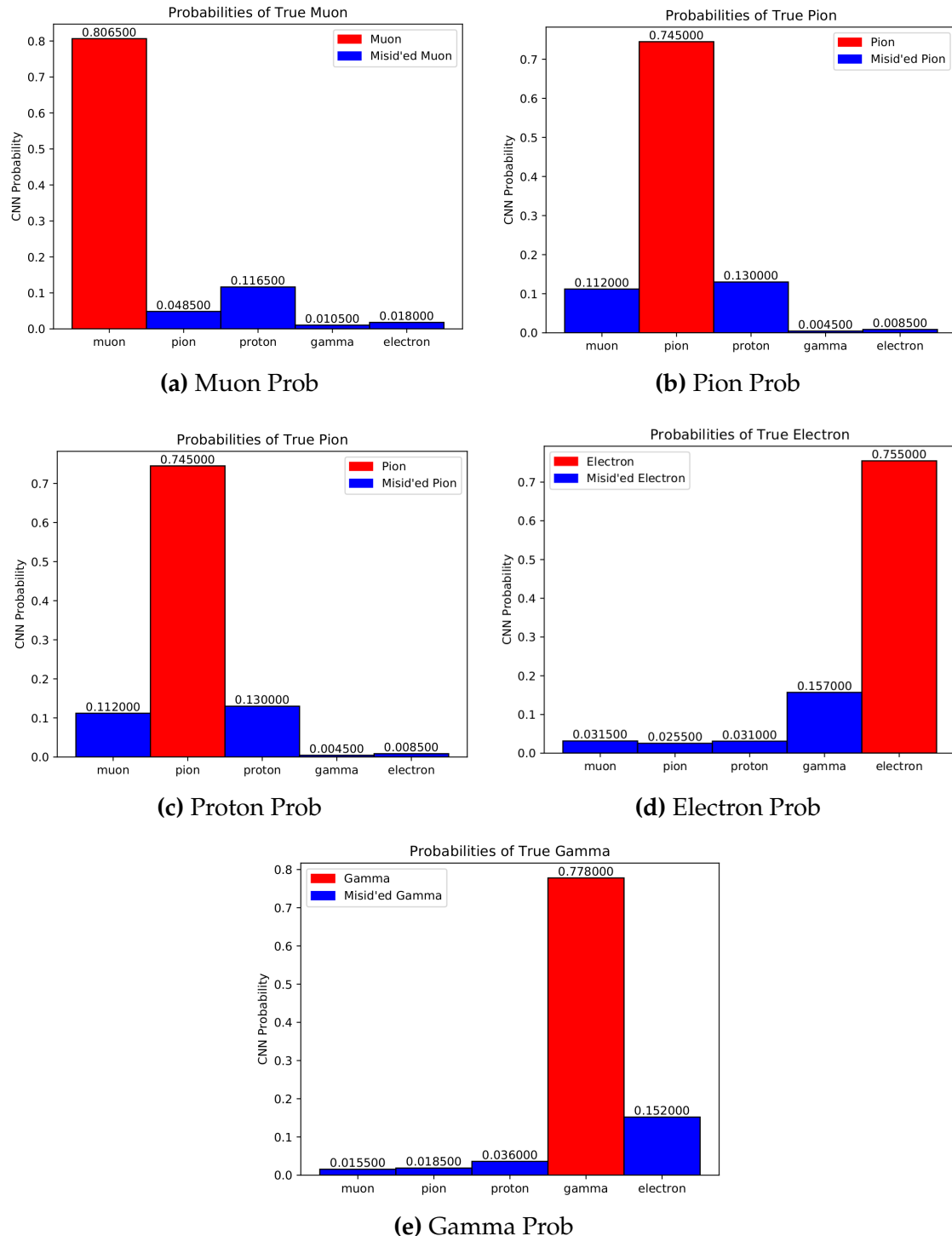


Figure 7.10: Probabilities of different particle classes as well as their contamination from other classes

¹⁶⁴¹ protons. For pions, both protons and muons get misidentified as pions at around the
¹⁶⁴² same probability. Similar behavior is also seen for proton identification. Electrons and
¹⁶⁴³ gammas are misidentified as each-other with similar probabilities.

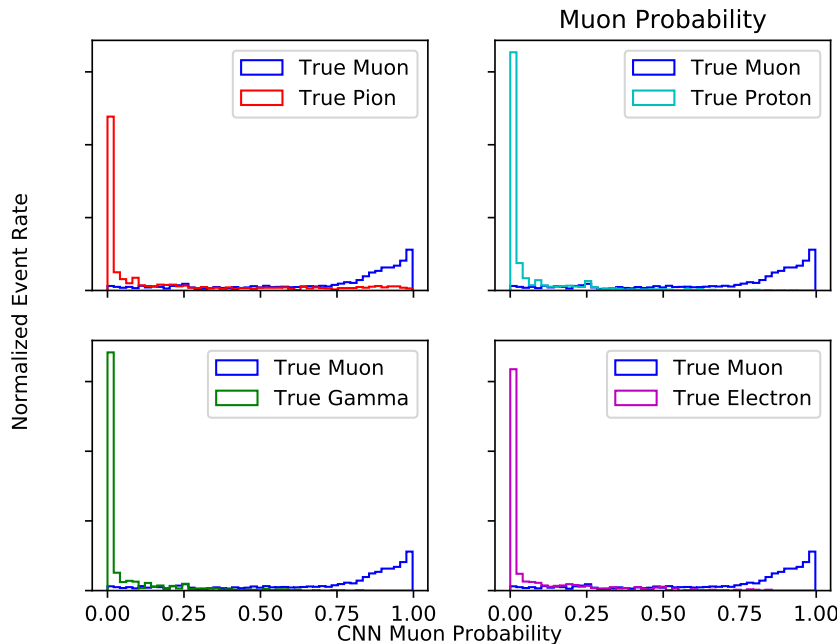
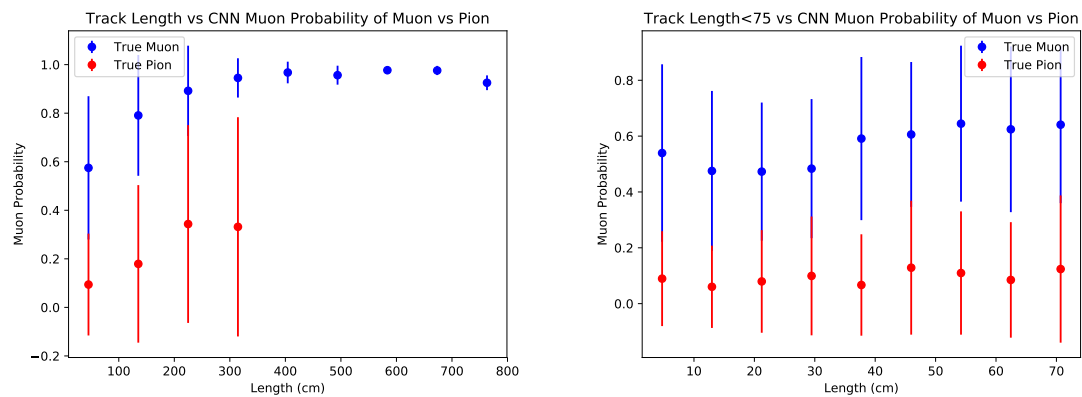


Figure 7.11: Muon probability of true muons (blue) versus pions (red), protons (cyan), gammas (green) and electrons (magenta).

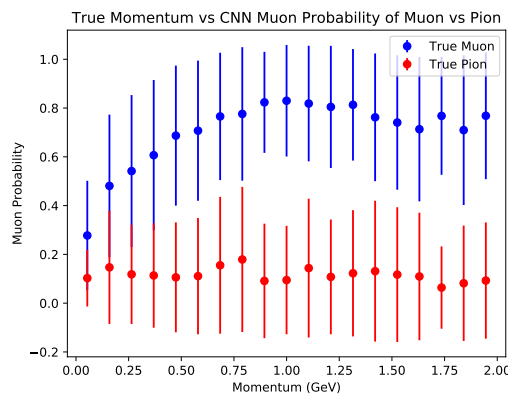
¹⁶⁴⁴ To see what type of background contamination one would be dealing with when
¹⁶⁴⁵ doing muon identification, muon probabilities for each particle class was plotted
¹⁶⁴⁶ against the probability of true muons to see how well muon signal vs other particle
¹⁶⁴⁷ background separation can be done with CNN100000. Figure 7.11 is showing the
¹⁶⁴⁸ true muon probability for true muons, versus the rest of the particle classes. This plot
¹⁶⁴⁹ describes which muon probability value should be chosen for the least amount of
¹⁶⁵⁰ other particle contamination. For electrons and gammas, a muon probability of $\sim 75\%$
¹⁶⁵¹ would eliminate e/γ contamination. For pions and protons, there is contamination at
¹⁶⁵² all values of muon probability, but the contamination is drastically reduced at a muon
¹⁶⁵³ probability $\geq 75\%$.

¹⁶⁵⁴ One of the main concerns with training a neural network was that the features the
¹⁶⁵⁵ network would learn to separate muons from pions would be track range, which is
¹⁶⁵⁶ what was used to begin with in selection I. To make sure that wasn't the case, the next
¹⁶⁵⁷ thing that was looked at was the muon probability versus track range and momentum

of the track. Figures 7.12 through 7.15 show the muon probability in blue for all plots against all other particles. A zoomed in version of track range for all particles was also plotted to make sure there is separation between the particles at low track range. The μ/π separation in track range and momentum is less than for $p/e/\gamma$ but that was to be expected. Although the separation isn't as good as the other particles, there still is separation at low momentum and low track range which cannot be done by using a track range cut like selection I does.

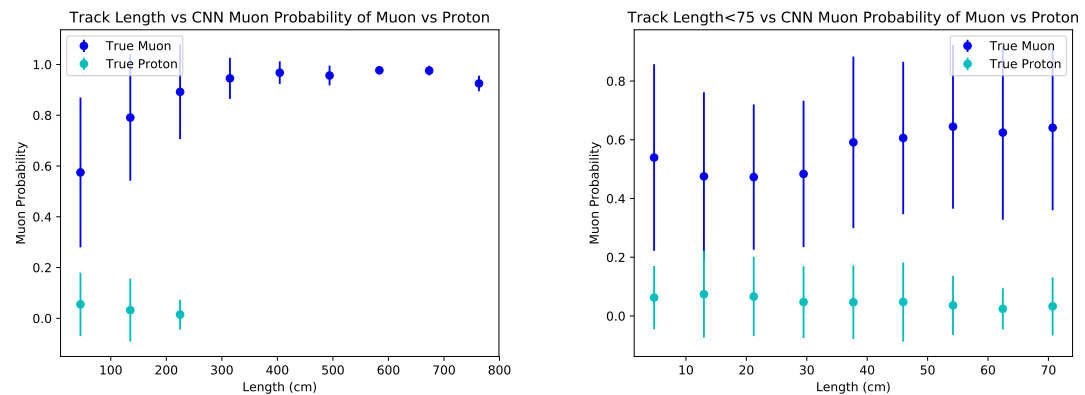


(a) Track range versus muon probability for true muons (blue) and true pions (red). (b) Track range ≤ 75 cm versus muon probability for true muons (blue) and true pions (red).

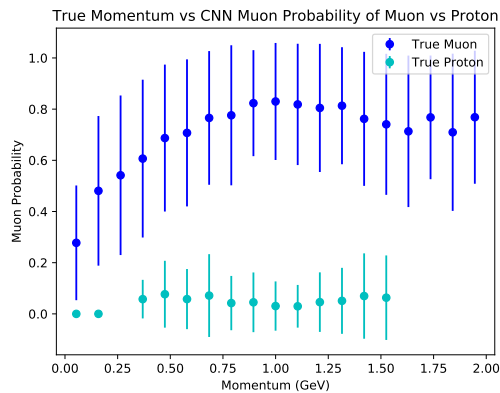


(c) Momentum versus muon probability for true muons (blue) and true pions (red).

Figure 7.12: Kinematic distributions versus muon probability for true muons and true pions.

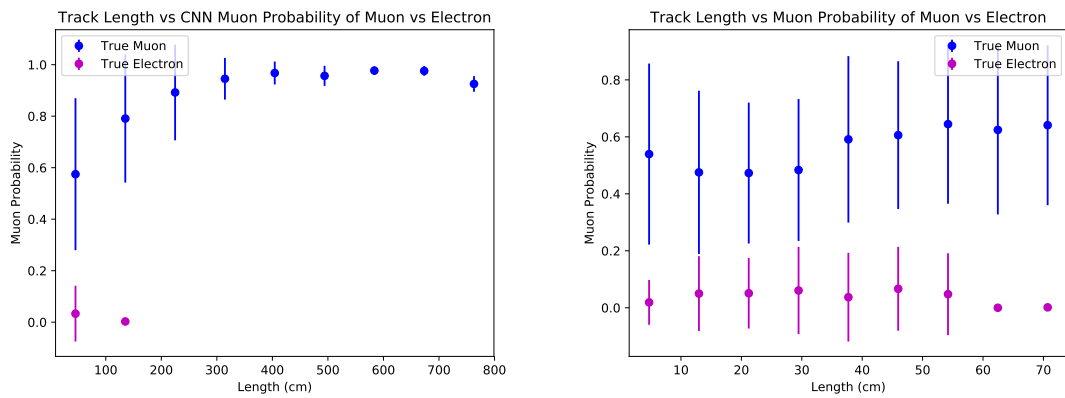


(a) Track range versus muon probability for true muons (blue) and true protons (cyan). (b) Track range ≤ 75 cm versus muon probability for true muons (blue) and true protons (cyan).

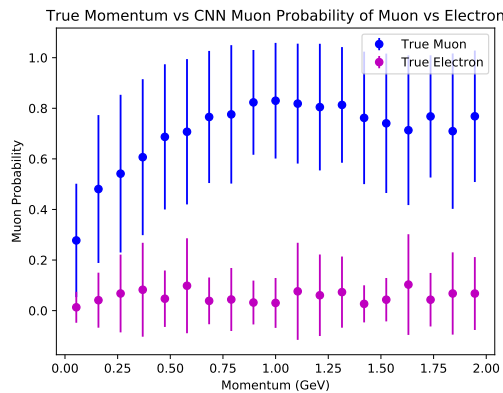


(c) Momentum versus muon probability for true muons (blue) and true protons (cyan).

Figure 7.13: Kinematic distributions versus muon probability for true muons and true protons.



- (a) Track range versus muon probability for true muons (blue) and true electrons (magenta).
- (b) Track range ≤ 75 cm versus muon probability for true muons (blue) and true electrons (magenta).



- (c) Momentum versus muon probability for true muons (blue) and true electrons (magenta).

Figure 7.14: Kinematic distributions versus muon probability for true muons and true electrons.

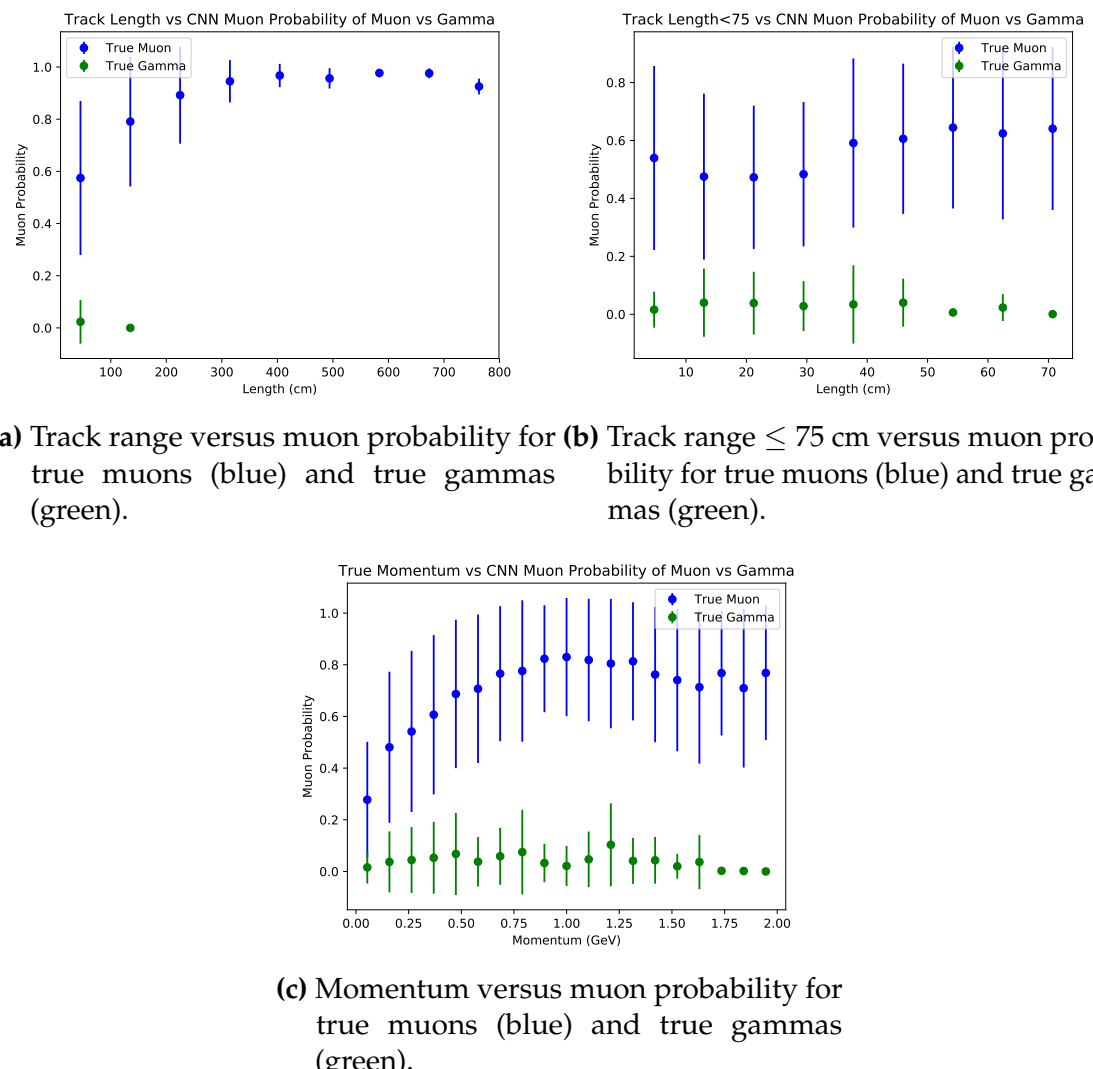


Figure 7.15: Kinematic distributions versus muon probability for true muons and true gammas.

1665 Chapter 8

1666 Using Convolutional Neural Networks 1667 for ν_μ CC event classification

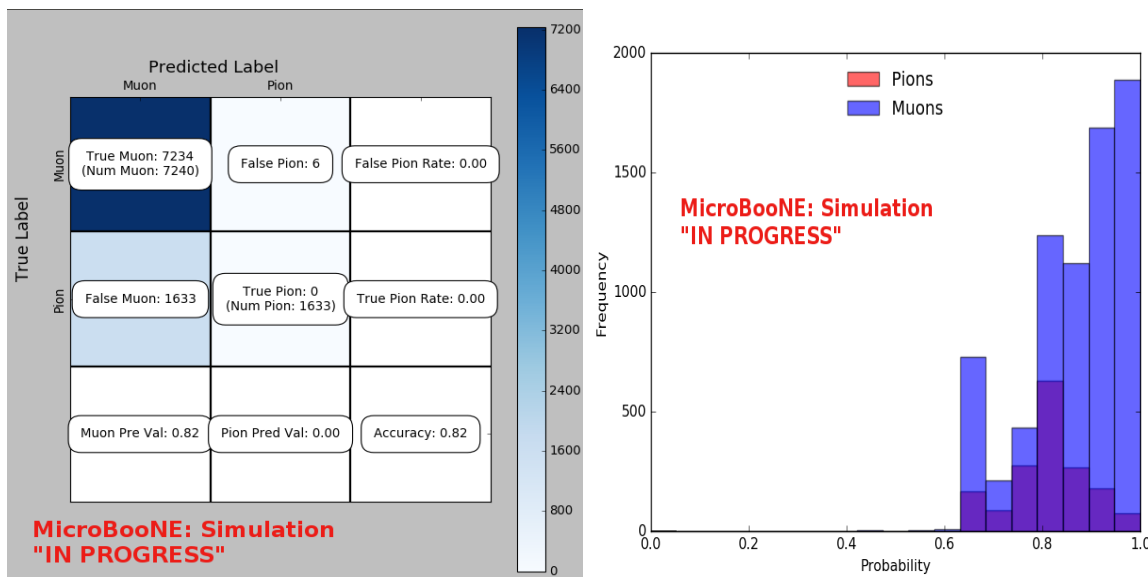
1668 8.1 Classification using CNN10000

1669 8.1.1 Classification of MC data using Selection I CC-Inclusive Filter

1670 CNN10000 was also used to classify track candidate images that were identified by
1671 the selection I cc-inclusive filter described in [?]. Passing rates for each cut in this filter
1672 are shown in figure ???. As seen in section ???, wrong image normalization had a higher
1673 muon classification probability so all work done using selection I cc-inclusive filter
1674 was done using this normalization. Out of 188,880 events, 19,112 passed the cut right
1675 before the 75 cm track length cut which is a 10.1% passing rate and comparable to
1676 the 10% passing rate shown in figure ???. In time cosmics were also run over, out of
1677 14,606 in time cosmics events, 302 passed the cut right before the 75 cm track length
1678 cut which is a 2.1% passing rate comparable to the 2.7% passing rate in the cc-inclusive
1679 tech-note. Figures 8.1a and 8.1b show the accuracy and μ/π separation. Both plots
1680 are only composed of muons and pions and like selection I original data, all other
1681 particles were id'ed as muons. Also like selection I original data, muons are being
1682 identified at a very high rate. Figure 8.2a shows the track range distributions of all
1683 events from selection I being classified by the CNN as a muon with a probability of
1684 70% regardless of true particle type. We get entries for the CNN curve in the lowest
1685 bin and none for the 75 cm curve. To see how many true CC events were identified
1686 by CNN10000 breaking down figure 8.2a by event type was necessary. Figures 8.2b
1687 and 8.2c show track range distributions separated by signal and various backgrounds.

1688 Particle type was not taken into consideration in these plots so true CC event images
 1689 can be any track candidate particle passing selection I cut right before track length cut
 1690 including pions and protons.

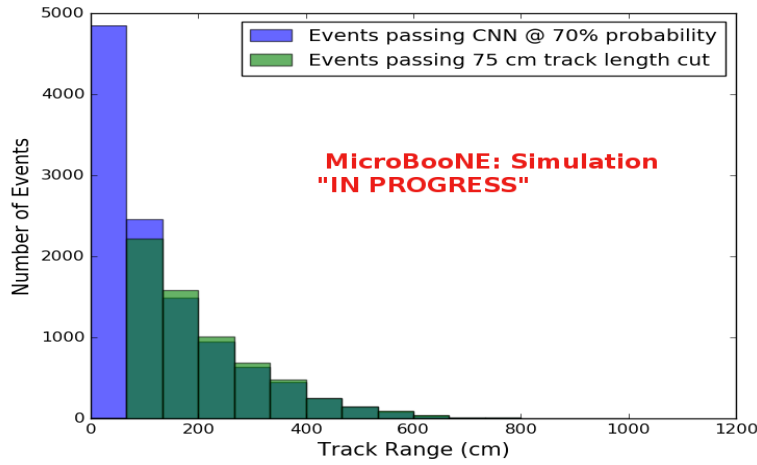
1691 To gain an even deeper understanding on how CNN10000 is performing, plotting
 1692 these distributions with only muons and pions was done due to the fact that CNN10000
 1693 was trained with only those particles for μ/π separation. Figures 8.2d-8.3d show the
 1694 stacked histograms of signal and background of the track range distributions with
 1695 varying CNN probabilities starting from 70% and ending at 90% probability. With
 1696 higher probabilities we get a purer sample in the lower bin but we end up losing
 1697 events as well. Momentum distributions for all signal/background events are shown
 1698 in figure 8.4.



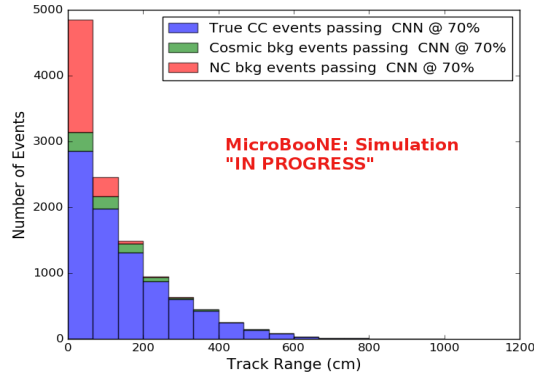
(a) Confusion Matrix for CNN10000 classified events from selection I (b) Probability plot for CNN10000 classified events from selection I

Figure 8.1: Confusion matrix and probability plot of events passing selection I cc-inclusive cuts right before 75cm track length cut

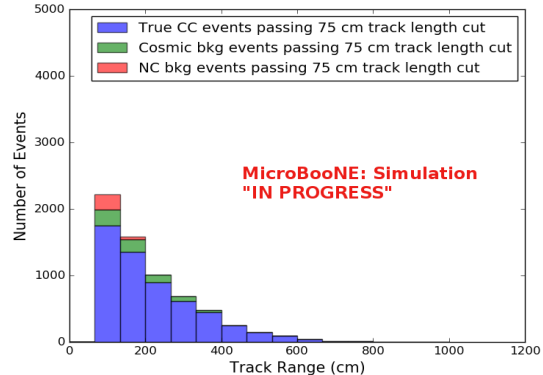
1699 Another check was to see if any true CC pions were passing through the cut right
 1700 before the 75 cm track length cut. Figure 8.5 shows the comparison of the stacked track
 1701 range distribution with only true CC muon signal versus the stacked distribution with
 1702 true CC muons and pions signal. As you can see, we gain more events when plotting
 1703 CC events with a particle type of either muons or pions due to the CNN classifying
 1704 all pions in this dataset as muons. This is an interesting scenario and a sample of
 1705 topologies of these images are represented in figure 8.6, at least 3 tracks are coming out



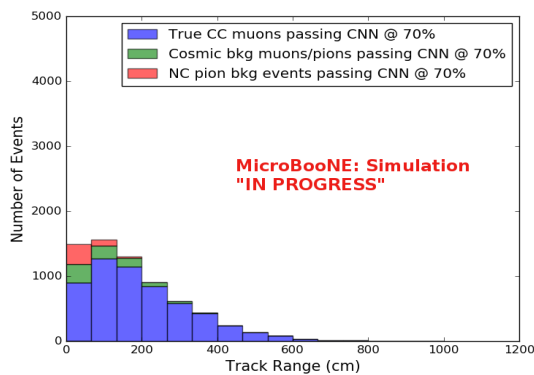
(a) Track range distribution of events from Selection I Modified passing CNN with 70% accuracy



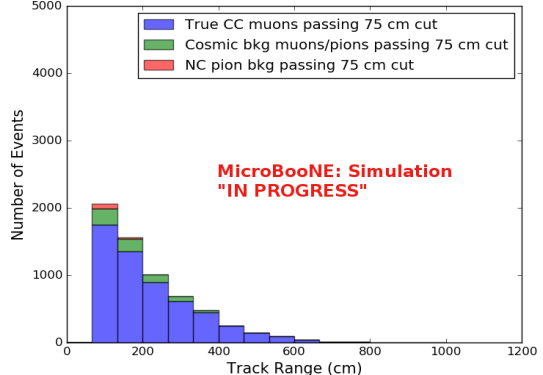
(b) Stacked signal and background track range distributions from Selection I Modified passing CNN with 70% accuracy



(c) Stacked signal and background track range distributions from Selection I Modified passing 75 cm track length cut



(d) Stacked signal muons and background muons/pions of track range distributions from Selection I Modified passing CNN with 70% accuracy



(e) Stacked signal muons and background muons/pions of track range distributions from Selection I Modified passing 75 cm track length cut

Figure 8.2: CNN10000 distributions of track candidate images output from Selection I Modified cc-inclusive filter

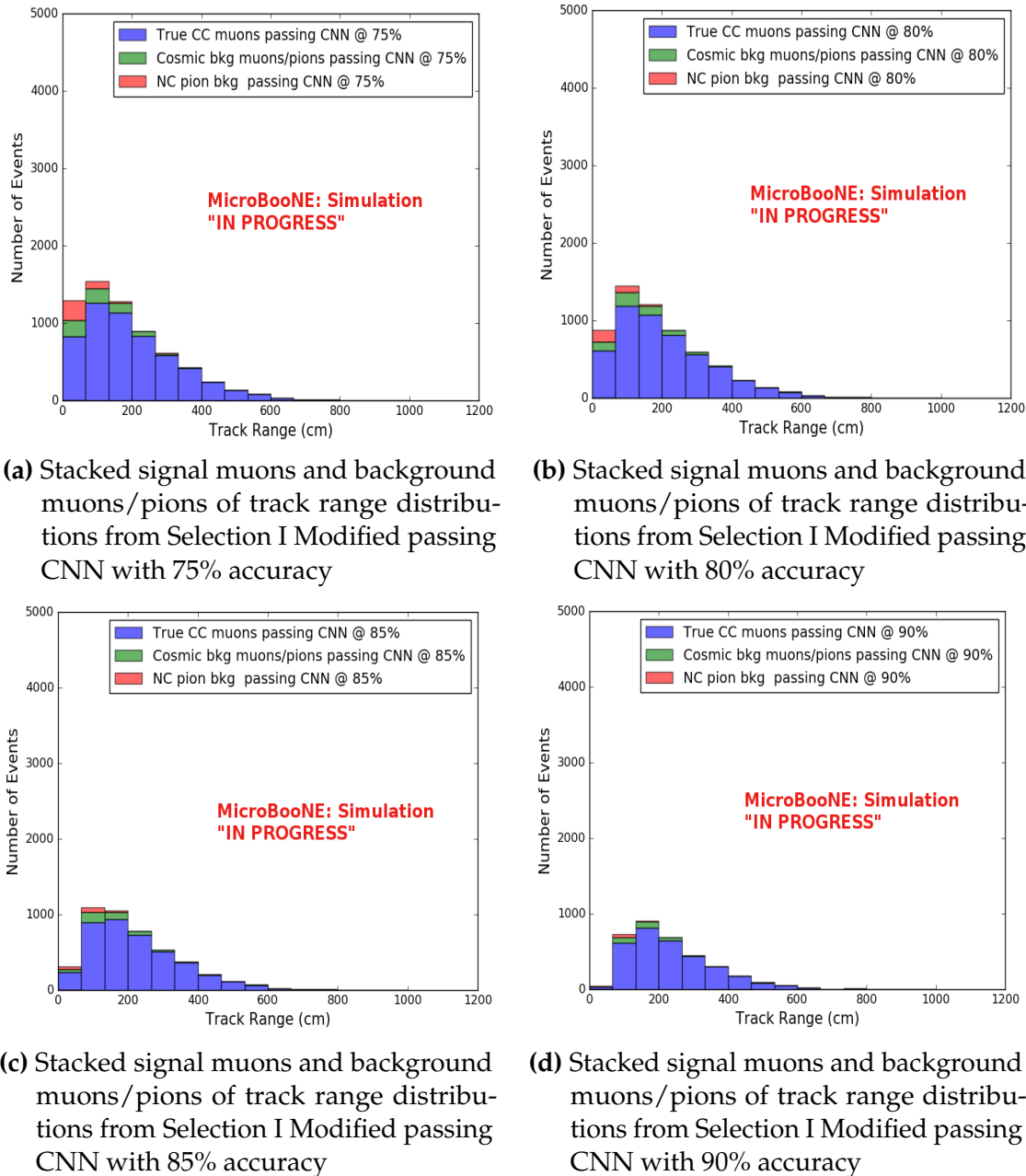
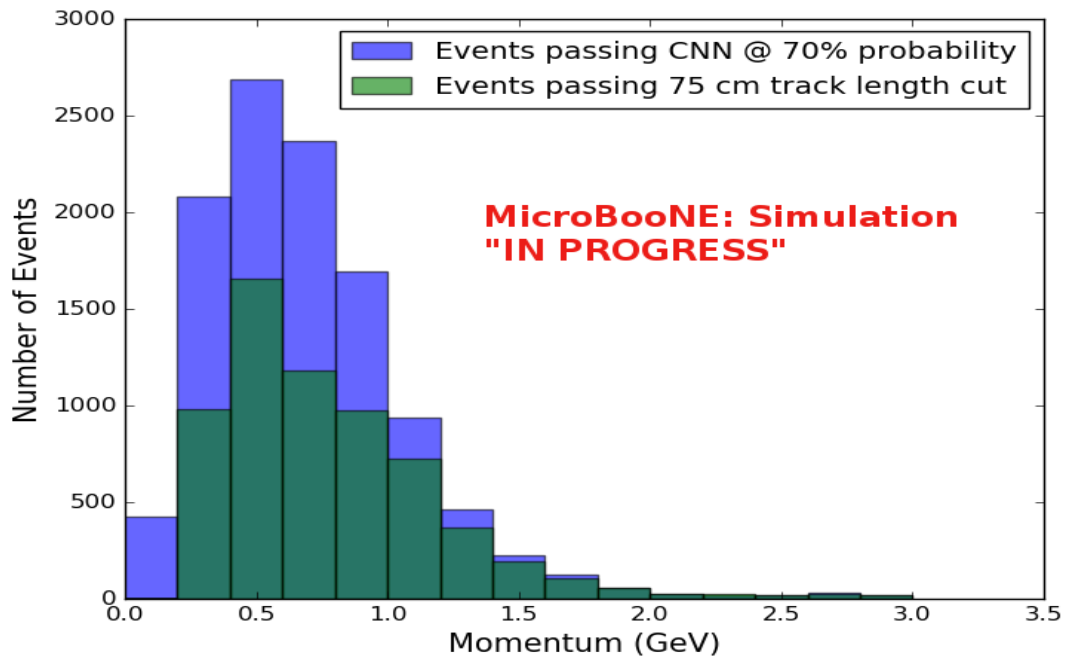
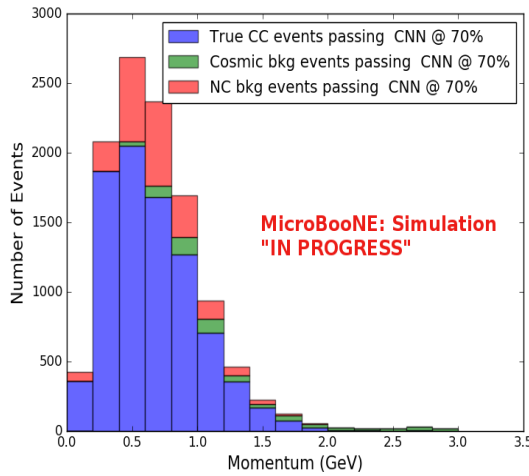


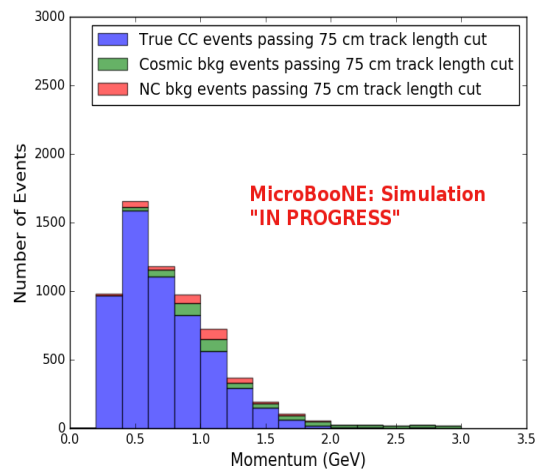
Figure 8.3: CNN10000 stacked signal/background track range distributions of track candidate images output from Selection I Modified cc-inclusive filter



(a) Momentum distribution of events from Selection I Modified passing CNN with 70% accuracy



(b) Stacked signal and background momentum distributions from Selection I Modified passing CNN with 70% accuracy



(c) Stacked signal and background momentum distributions from Selection I Modified passing 75 cm track length cut

Figure 8.4: CNN10000 momentum distributions of track candidate images output from Selection I Modified cc-inclusive filter

of the vertex for these types of events. With the 75 cm track length cut, the selection is cutting event topologies like this where the pion is the tagged track candidate. Figure 8.6a has a defined longer muon track, but because of dead wires through the track, the reconstructed range is 1. less than 75 cm and 2. shorter than the reconstructed pion whose length is also less than 75 cm. This is a very interesting event, but because of issues with the tracking algorithm, the 75 cm cut would get rid of this event. The CNN was able to recover this event only because it has classified all pions as muons. Figure 8.6b shows the second case to think about, the pion, while still less than 75 cm has a reconstructed track length longer than the muon. Again, the CNN recovered this event due to pions being classified as muons. Lastly, figure 8.6c shows a pion with a reconstructed track length greater than 75 cm and the muon. These three cases show that a broader question must be asked when training the network other than is it a muon or pion. There are different routes to recover interesting events like these. One route is to ask the network “Is it a CC event or is it an NC event?” and obtain an image dataset consisting of whole CC/NC events that will train the network to answer this question. The other route is to ask the network “Is this a $\mu/\pi/p/$ from a CC event or NC event and obtain an image dataset consisting of primary particles from a CC/NC event. Both these paths will be explored in future work.

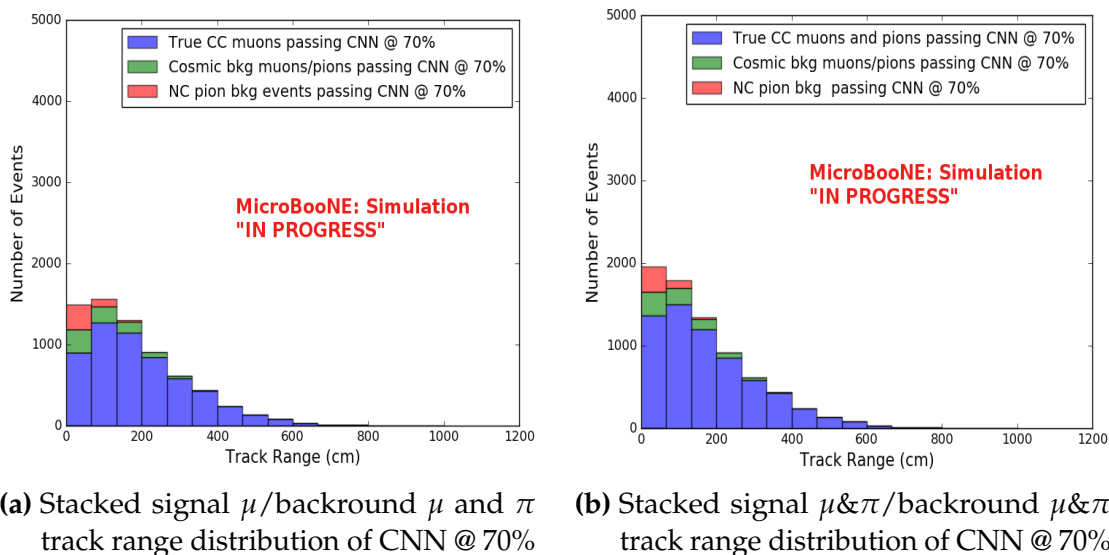


Figure 8.5: Track distribution comparisons of true CC muons plotted vs true CC muons and pions plotted

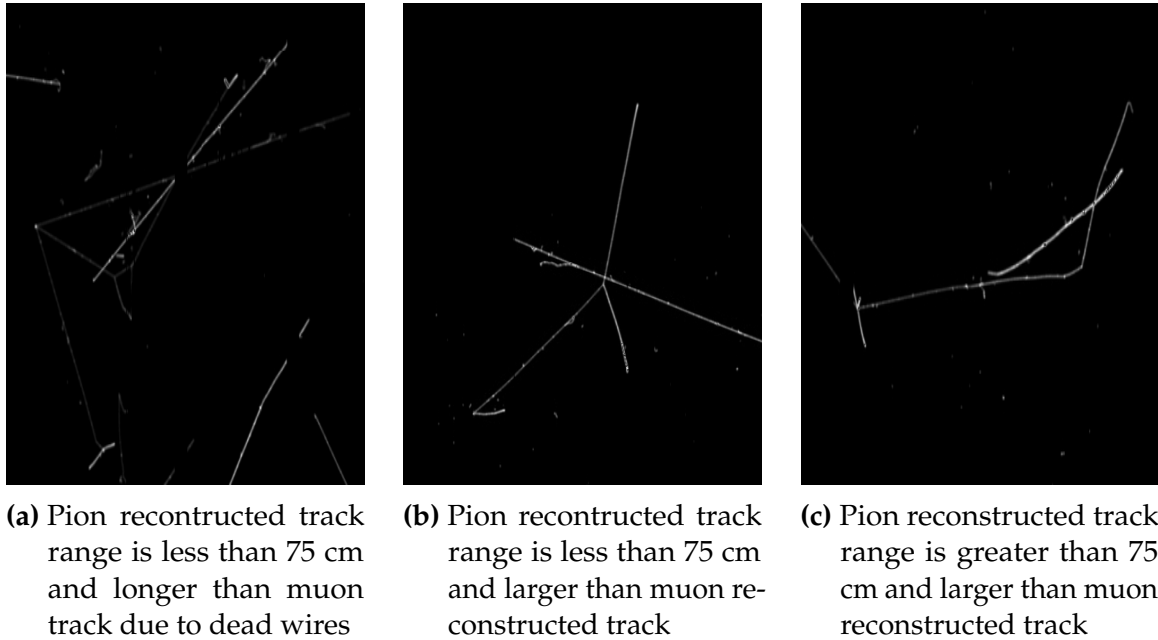


Figure 8.6: Images of true CC events where the pion was the tagged track candidate

		BNB + Cosmics		Cosmic Only	Signal: Cosmic Only
		Selection	MC Truth		
75 cm Cut passing rates	Generated Events	191362	45723	4804	1:22
	Track Containment	19391 (48%/10%)	11693 (45%/26%)	129 (38%/2.7%)	1:2.3
	track \geq 75 cm	6920 (36%/3.6%)	5780 (49%/13%)	17 (13%/0.4%)	1:0.6
CNN passing rates	Generated Events	188880	44689	14606	1:21
	Track Containment	19112 (/10%)	11554 (/26%)	302 (/2.1%)	1:1.73
	CNN cut @ 70% Probability	16502 (86%/8.7%)	10605 (92%/23%)	205 (68%/14%)	1:1.28
	CNN cut @ 83% Probability	7511 (46%/4.0%)	6142 (58%/14%)	32 (16%/0.2%)	1:0.4

Table 8.1: Comparing passing rates of CNN at different probabilities versus 75 cm track length cut: Numbers are absolute event counts and Cosmic background is not scaled appropriately. The BNB+Cosmic sample contains all events. The numbers in brackets give the passing rate wrt the step before (first percentage) and wrt the generated events (second percentage). In the BNB+Cosmic MC Truth column shows how many true ν_μ CC-inclusive events (in FV) are left in the sample. This number includes possible mis-identifications where a cosmic track is picked by the selection instead of the neutrino interaction in the same event. The CNN MC True generated events were scaled wrt the MC True generated events for the 75 cm cut passing rates due to only running over 188,880 generated events versus the 191362 generated events. The last column Signal:Cosmic only gives an estimate of the ν_μ CC events wrt the cosmic only background at each step. For this number, the cosmic background has been scaled as described in [?]. Note that these numbers are not a purity, since other backgrounds can't be determined at this step.

¹⁷²⁴ Table 8.1 shows the passing rates for the 75 cm track length cut and the CNN cut
¹⁷²⁵ at 70% and 83%. The passing rates at the track containment level for the 75 cm track

Signal	ν_μ CC events with true vertex in FV	#Events(Fraction)	#Events(Fraction)
		passing Sel I	passing CNN @ 83% Probability
Backgrounds	Cosmics Only Events	725(33.4%)	2582(26%)
	Cosmics in BNB Events	144(6.6%)	492(4.9%)
	NC Events	75(3.5%)	778(7.7%)
	ν_e and $\bar{\nu}_e$ Events	4(0.2%)	32(0.3%)
	$\bar{\nu}_\mu$ Events	40(1.8%)	67(0.7%)

Table 8.2: Signal and background event numbers of selection I and selection I with CNN cut estimated from a BNB+Cosmic sample and Cosmic only sample normalized to $5 * 10^{19}$ PoT. The last column gives the fraction of this signal or background type to the total selected events per CNN probability.

length cut compared to the CNN are comparable with only a 0.6% difference in the in time cosmic bin which may be due in part to the larger in time cosmic statistics used for the CNN dataset. These passing rates need to be comparable to then be able to compare the passing rates after the CNN cut to the 75 cm cut. Again, the same BNB+Cosmic sample was used for both selection I with 75 cm cut and selection I with CNN cut. As it stands, a CNN cut at 83% probability has a MC true CC event passing rate of 14% compared to the 13% passing rate of the 75 cm track length cut. The Signal:Cosmic Only background is also reduced from 1:0.6 to 1:0.4. The total passing rate is also higher than the 75 cm cut, 3.6% vs 4.0%. Table 8.2 shows the breakdown of signal and backgrounds for the CNN at the different probabilities. We have a 61% signal passing rate with the CNN cut @ 83% versus the 53.8% signal passing rate of the 75 cm cut.

Based on these numbers, the following performance values of the selection with 75 cm cut versus selection with CNN @ 83% probability cut were calculated:

- Efficiency: Number of selected true ν_μ CC events divided by the number of expected true ν_μ CC events with interaction in the FV.
 - Selection I: 12.3%
 - Selection I with CNN10000 cut @ 83% probability: 14%
- Purity: Number of selected true ν_μ CC events divided by sum of itself and the number of all backgrounds.
 - Selection I: 53.8%

- 1747 – Selection I with CNN10000 cut @ 83% probability: 61%

1748 Lastly, figure 8.7 shows a more representative performance of the CNN. Due to the
 1749 fact that the CNN was trained on muons and pions, showing the performance of CC
 1750 muon events versus NC pion events with respect to CNN probability gives a better
 1751 picture of how the network is performing. Figure 8.7 shows that at 83% we are below
 1752 the 75 cm cut NC pion threshold and still above the CC muon threshold. Using 83%
 1753 probability not only reduced the NC pion background, it also dramatically reduced
 1754 the in time cosmics and cosmics in the BNB.

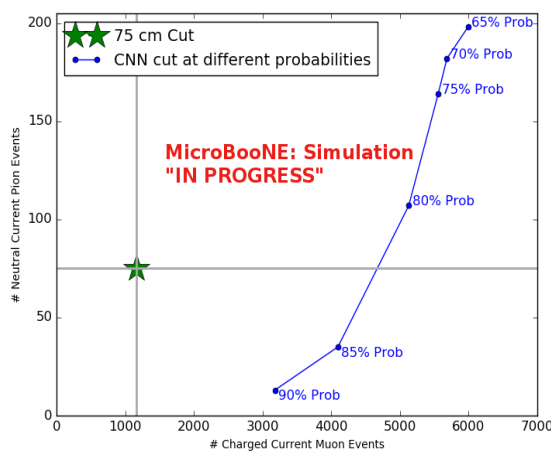


Figure 8.7: CNN performance of classified muons and pions compared to the already implemented 75 cm track length cut

1755 8.1.2 Conclusions of CNN10000 classification of MC data

1756 It was shown that even though CNN10000 was trained with single particle generated
 1757 muons and pions, it performs fairly well at classifying track candidate images from
 1758 BNB+Cosmic events. Events have been regained below the 75 cm track length cut and
 1759 the momentum and track range distributions have similar shapes to the distributions
 1760 of Selection I. Efficiencies and purities were calculated for selection I events before 75
 1761 cm track length cut with the CNN at 83% probability and are 14% and 62% respectively.
 1762 Although the CNN doesn't have separation between muons and pions and although
 1763 all particles passing CNN are classified as muon, increasing CNN probability allows
 1764 us to increase the purity as well as maintain an efficiency comparable to the 75 cm track
 1765 length cut all while recovering events below that 75 cm cut. Out of the 6142 events
 1766 that passed the CNN @ 83% 1470 events were below the 75 cm cut, a recovery of 3.3%

₁₇₆₇ of data with an purity of 15%. Although these numbers are low, it is an improvement
₁₇₆₈ from the selecion I in both total efficiency and purity and an increase in phase space
₁₇₆₉ by recovering these events.

₁₇₇₀ 8.2 Classification using CNN100000

₁₇₇₁ To reiterate, CNN100000 was trained using 20,000 images of each $\mu/\pi/p/\gamma/e$. The
₁₇₇₂ results of using CNN100000 to classify BNB+Cosmics will be outlined below.

₁₇₇₃ 8.2.1 Classification of MC data using Selection I CC-Inclusive Filter

₁₇₇₄ Kinematic truth distributions of BNB+Cosmic events passing Selection
₁₇₇₅ I+CNN10000

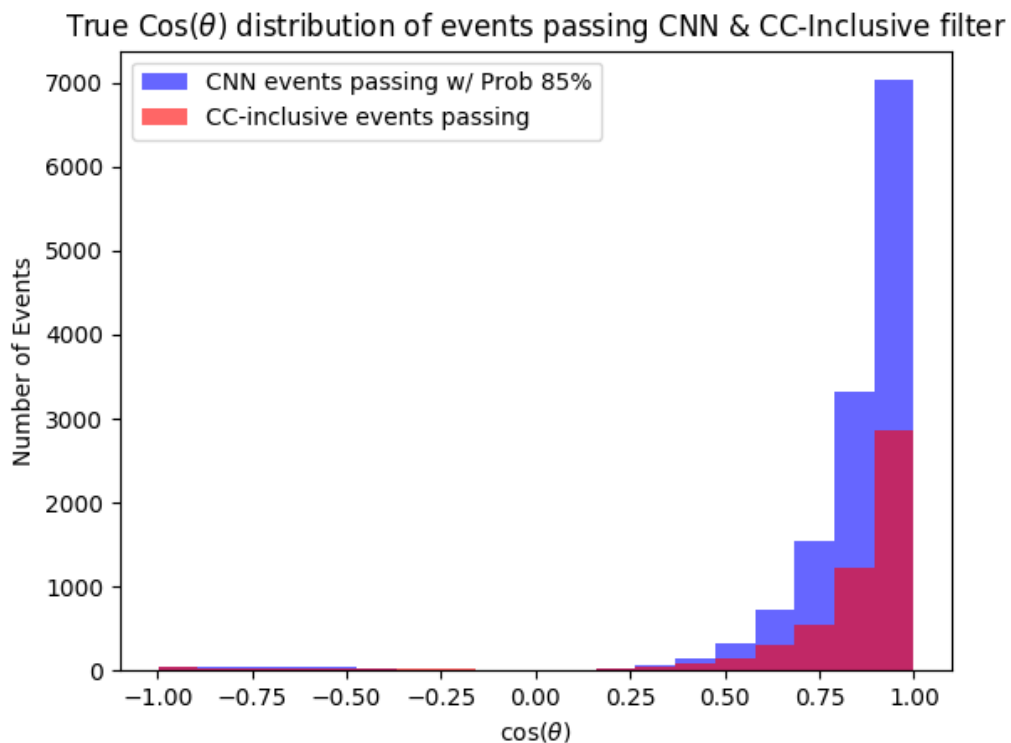


Figure 8.8: $\text{Cos}(\theta)$ distribution at $\text{CNN10000} \geq 85\%$

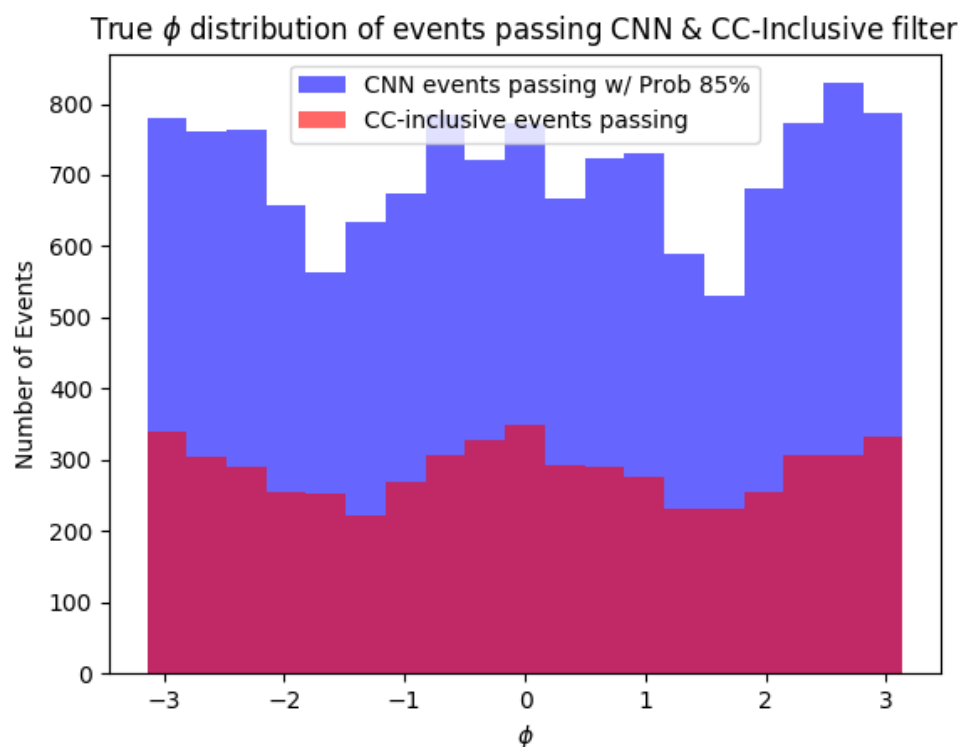


Figure 8.9: $\cos(\theta)$ distribution at $\text{CNN10000} \geq 85\%$

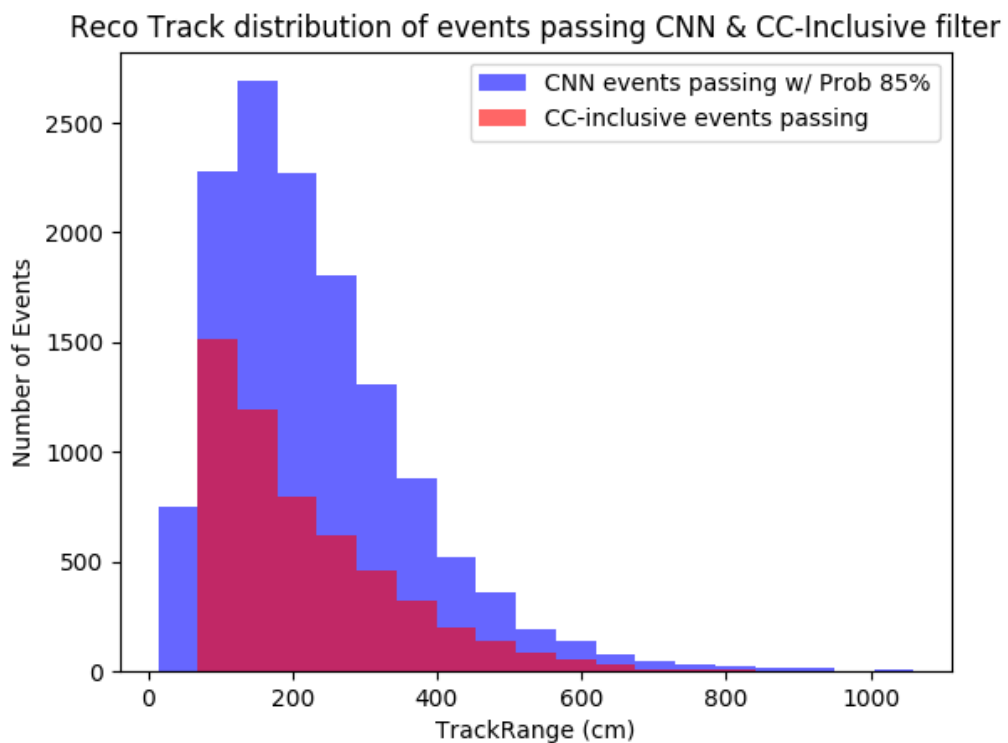


Figure 8.10: $\cos(\theta)$ distribution at $\text{CNN10000} \geq 85\%$

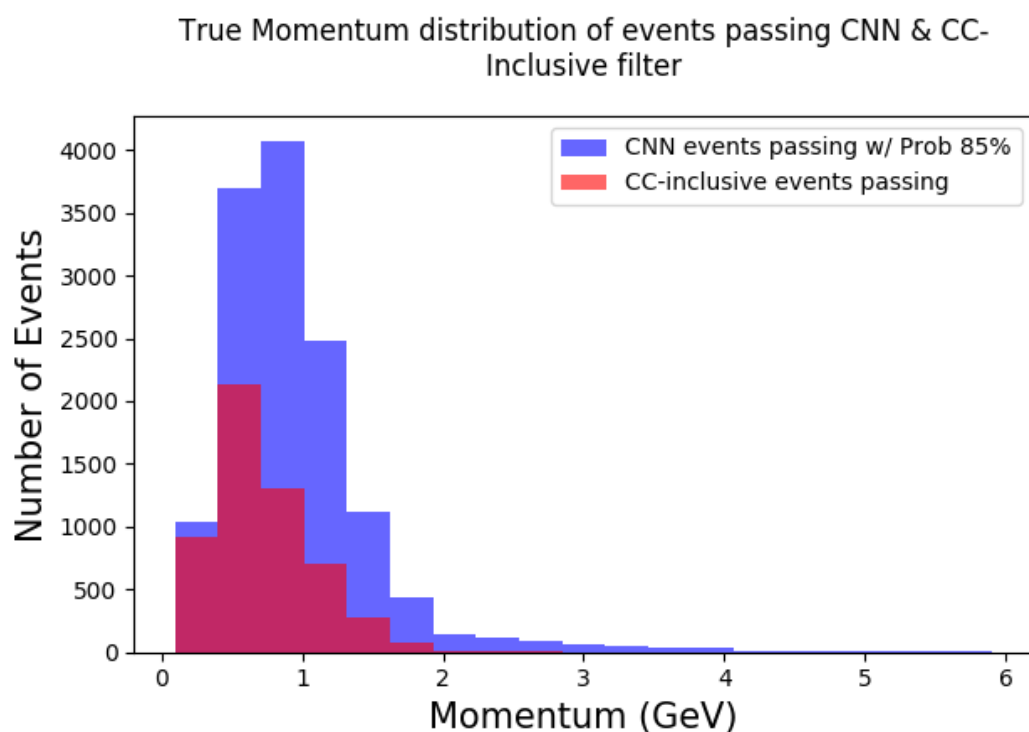


Figure 8.11: $\cos(\theta)$ distribution at $\text{CNN10000} \geq 85\%$

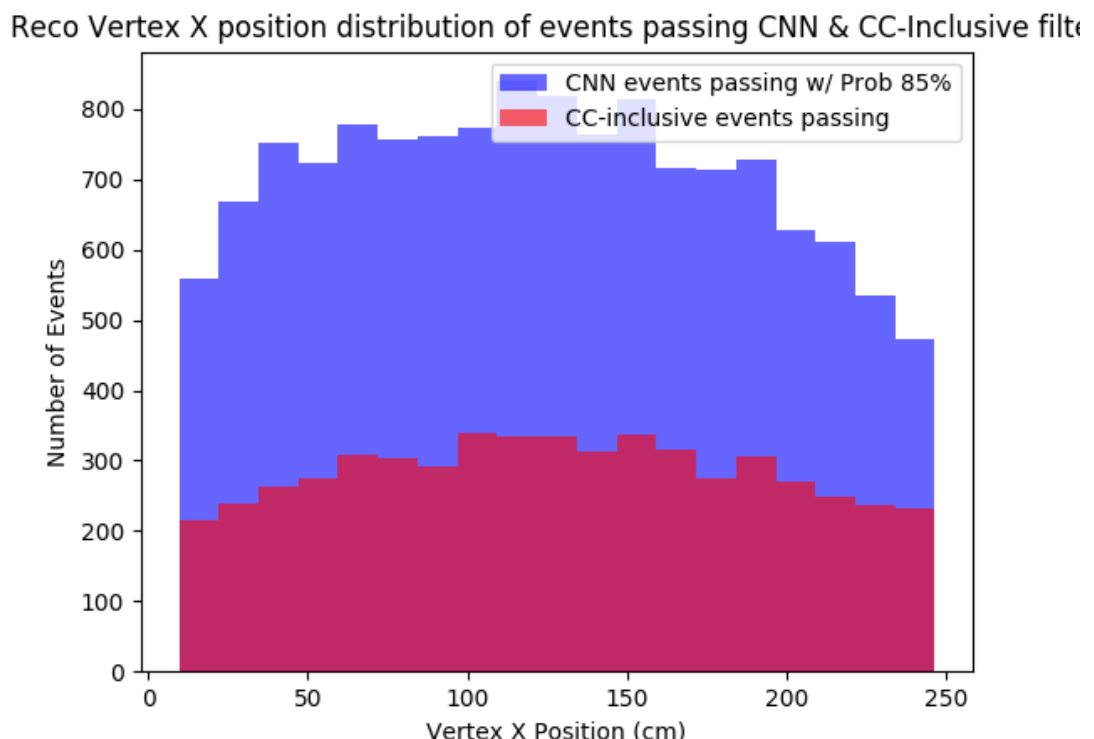


Figure 8.12: $\cos(\theta)$ distribution at $\text{CNN10000} \geq 85\%$

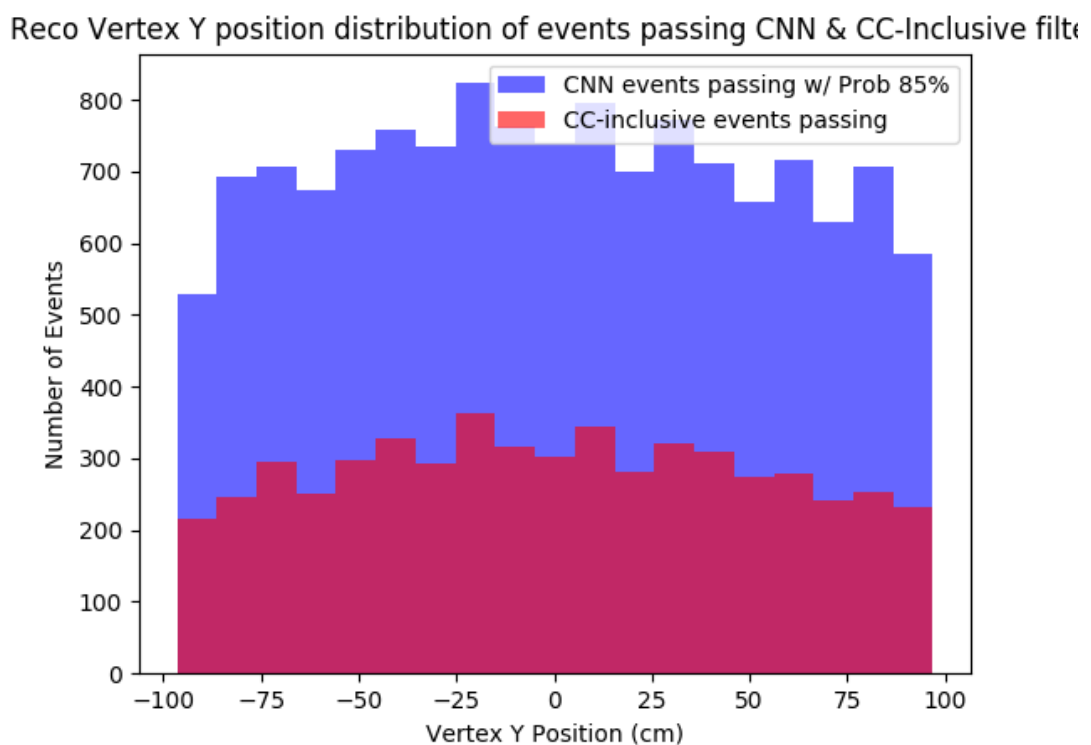


Figure 8.13: $\cos(\theta)$ distribution at $\text{CNN10000} \geq 85\%$

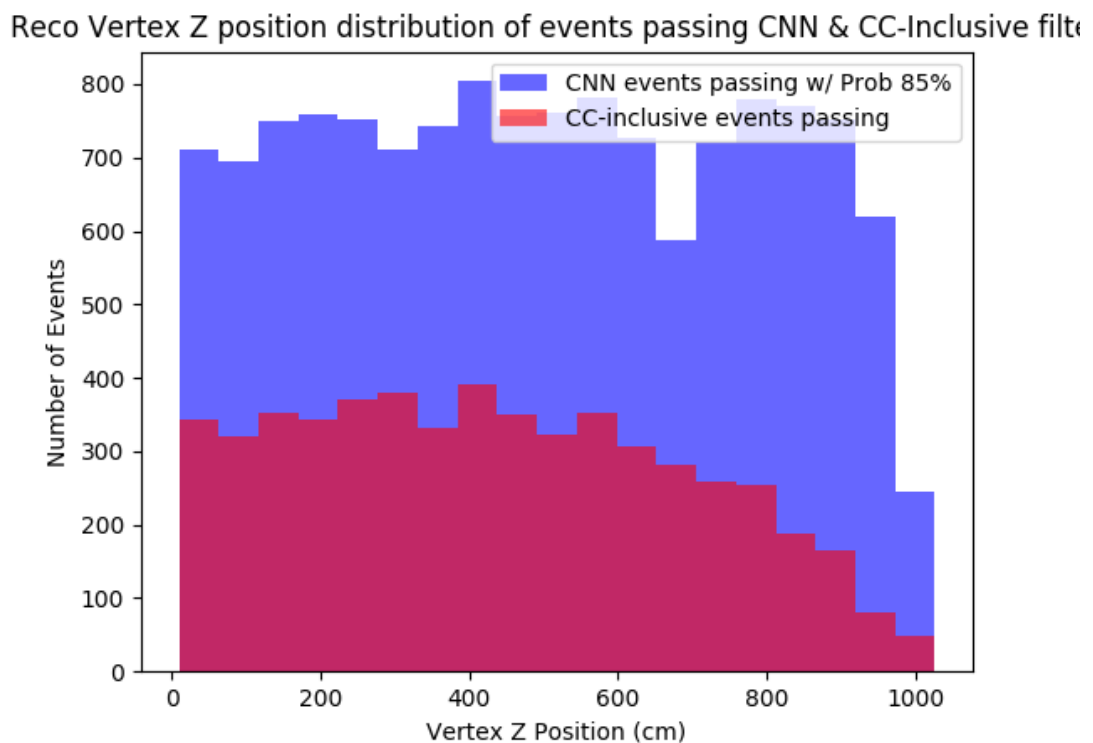


Figure 8.14: $\cos(\theta)$ distribution at $\text{CNN10000} \geq 85\%$

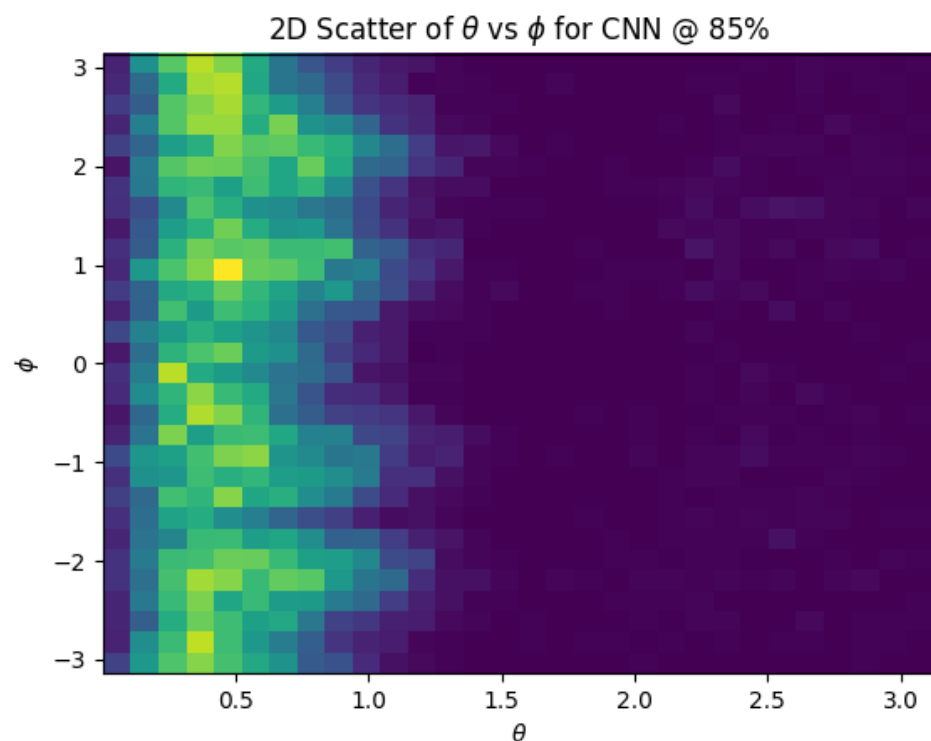


Figure 8.15: $\cos(\theta)$ distribution at $\text{CNN10000} \geq 85\%$

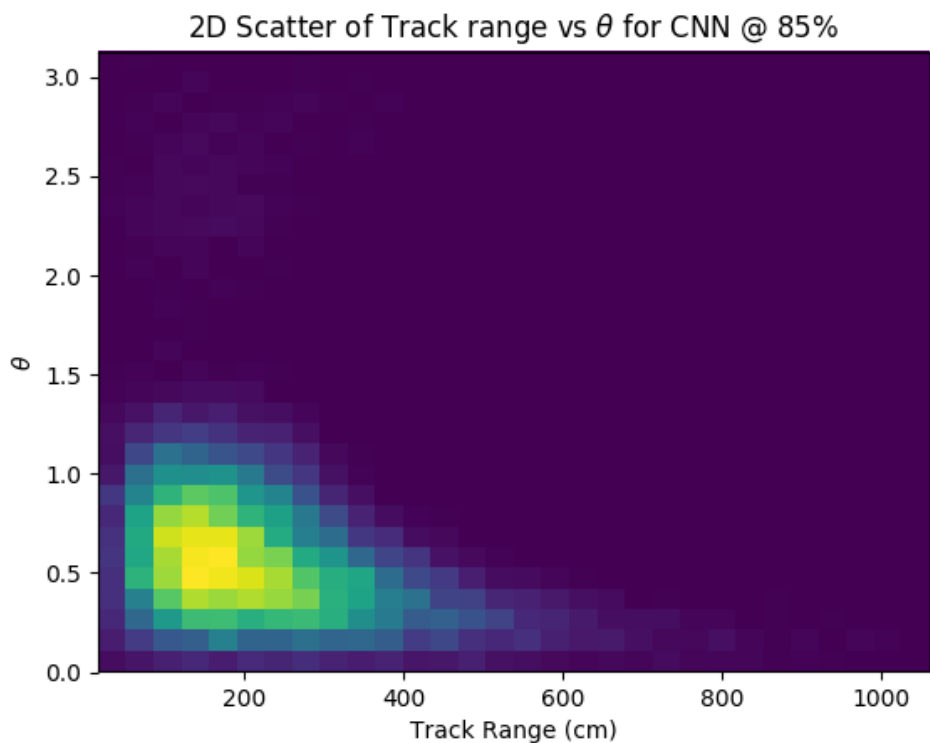


Figure 8.16: $\cos(\theta)$ distribution at CNN10000 $\geq 85\%$

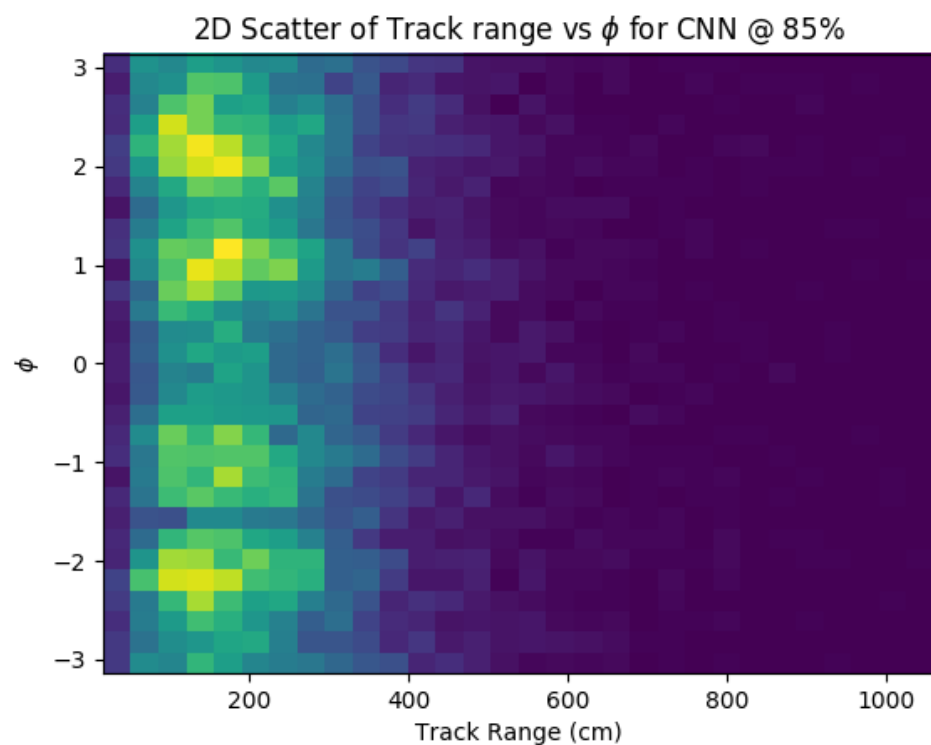


Figure 8.17: $\cos(\theta)$ distribution at $\text{CNN10000} \geq 85\%$

₁₇₇₆ **8.2.2 Classification of MicroBooNE data using Selection I**

₁₇₇₇ **CC-Inclusive Filter**

₁₇₇₈ **8.2.3 Comparing two CC-Inclusive Cross Section Selection Filters**

¹⁷⁷⁹ **Chapter 9**

¹⁷⁸⁰ **Conclusion**

¹⁷⁸¹ Your Conclusions here.

¹⁷⁸²

¹⁷⁸³ Bibliography

- ¹⁷⁸⁴ [1] Wikipedia, Neutrino, <http://wikipedia.org/wiki/Neutrino>, 2013.
- ¹⁷⁸⁵ [2] Wikipedia, Neutrino oscillation, http://en.wikipedia.org/wiki/Neutrino_oscillation, 2013.
- ¹⁷⁸⁶ [3] B. N. Laboratory, Neutrinos and nuclear chemistry, <http://www.chemistry.bnl.gov/sciandtech/sn/default.htm>, 2010.
- ¹⁷⁸⁷ [4] K. Heeger, Big world of small neutrinos, <http://conferences.fnal.gov/lp2003/forthepublic/neutrinos/>.
- ¹⁷⁸⁸ [5] A. Y. Smirnov, p. 23 (2003), hep-ph/0305106.
- ¹⁷⁸⁹ [6] The MicroBooNE Collaboration, R. e. a. Acciari, (2015), arXiv:1512.06148.
- ¹⁷⁹⁰ [7] The MicroBooNE Collaboration, R. e. a. Acciari, (2016), arXiv:1705.07341.
- ¹⁷⁹¹ [8] The MicroBooNE Collaboration, R. e. a. Acciari, (2017), arXiv:1704.02927.
- ¹⁷⁹² [9] The MicroBooNE Collaboration, R. e. a. Acciari, JINST **12** (2017).